ABSTRACT

Title of dissertation: PHOTOCURRENT SPECTROSCOPY OF PENTACENE THIN FILM TRANSISTORS

Mihaela Breban, Doctor of Philosophy, 2006

Dissertation directed by: Professor Ellen Williams
Department of Physics

We demonstrate the application of photocurrent modulation spectroscopy in characterizing the performance of organic thin-film transistors. A parallel analysis of the direct current and photocurrent voltage characteristics provides a model-free determination of the field-effect mobility and the density of free carriers in the transistor channel as a function of the applied gate voltage. Applying this technique to pentacene thin-film transistors demonstrates that the mobility increases as $V_g^{1/3}$. The free-carrier density is approximately 1/10 of the expected capacitive charge, and the mobility increases monotonically with the free carrier density, consistent with the trap and release model of transport.

Also, the modulated photocurrent spectroscopy can be used as a probe of defect states in pentacene thin film transistors, measuring simultaneously the magnitude and the phase of the photocurrent as a function of the modulation frequency. This is accomplished by modeling the photo-carrier generation process as exciton dissociation via interaction with localized traps. Experimental data reveal a Gaussian distribution of localized states centered around 0.3 eV above the highest occupied

molecular orbital. We also investigated the effect of the gate dielectric material with our probe and found that the position of the extracted gaussian slightly shifts, consistent with the expected image charge effect for Pn through the dielectric substrate. Also shifts in the gaussian position for samples fabricated with variable deposition conditions are correlated with changes in Pn morphology. The morphological differences between Pn films were also detected in current-voltage characteristics and photocurrent spectra. However, the origin of the ubiquitous 0.3 eV defect in Pn seems to be unrelated to structural differences in Pn films.

PHOTOCURRENT SPECTROSCOPY OF PENTACENE THIN FILM TRANSISTORS

by

Mihaela Breban

Dissertation submitted to the Faculty of the Graduate School of the
University of Maryland, College Park in partial fulfillment
of the requirements for the degree of
Doctor of Philosophy
2006

Advisory Commmittee:

Professor Ellen D. Williams, Chair/Advisor
Professor Theodore L. Einstein
Professor Michael S. Fuhrer
Professor Janice Reutt-Robey
Dr. Danilo B. Romero

ACKNOWLEDGMENTS

I want to express my gratitude to all the people who made this thesis possible. I am very grateful for the advice and support of my advisor, Prof. Ellen Williams. I thank her for her feedback, patience and advice whenever I knocked on her door. I wish to express my appreciation to Dr. Romero for guiding me in the lab and for our long stimulating discussions about physics. On a personal level, I very much thank him for being such a wonderful friend.

I thank my current and former colleagues in the Williams′ Organic Electronic Group. First, my thanks go to Sergey Mezhenny for designing the High Vacuum Evaporation System and for cooking special Eastern European dishes. I thank Karen Siegrist, Tracy Moore, Elba Gomar-Nadal, Dan Hines, Vinod Sangwan and Andrew Tunnell for providing valuable information, support and for their friendship over the years.

I am grateful to all the people in LPS for creating a professional but friendly environment. Special thanks to Dr. Bill Vanderlinde for support and help with SEM images for Pentacene transistors. All the experimental work was possible with J.B. Dotellis′ help in designing and fabricating different vacuum chambers.

And, I would like to especially mention my friends, Camelia and Iulian Mircea, Magda and Dragos Constantin and Sylvia Florez. Your friendships are very valuable to me. Iulian, our coffee talk helped boost my self-esteem and I learned a lot from our

discussions. I would like to extend my gratitude to my family: my parents Viorica and Pompi, my sister Gabriela and Matei. They always have provided unwavering love and encouragement. Finally, I would like to express my deepest gratitude to Vince for technical and emotional support. Thank you for being there for me.

TABLE OF CONTENTS

LIST OF TABLES

LIST OF FIGURES

Chapter 1

Pentacene: A Prototypical Organic Semiconductor Material for Thin-Film Transistors

1.1 Organic Semiconductor Thin-Film Transistors: An Overview

In contrast to covalent solids, organic molecular semiconductors are formed by weak van der Waals interactions between electrically neutral molecules. Consequently, the electronic properties of these materials retain much of the localized character of their molecular constituents. As such, organic molecular semiconductors can portray novel features not found in inorganic covalent solids or ionic semiconductor crystals. In addition, they possess desirable mechanical properties that are not displayed by conventional inorganic semiconductors, making them better suited for niche applications requiring large area coverage, structural flexibility, low temperature processing and low cost.

The light emitting properties of the organic materials are already being exploited for applications like television screens, computer displays, or advertising boards. In Fig. 1.1 we present an OLED display showing that this new technology is already part of our every day lives. Organic thin film transistors (OTFTs) are also good candidates for low-cost, large area electronics. For instance, they can act

Figure 1.1: OLED display fabricated by Samsung Electronics.

as switches behind each pixel of an active-matrix organic display, or be integrated in electronic bar codes or rf-identification tags. However, the organic thin film transistors are not yet mature enough to be marketable, even though significant progress has been made in the last 20 years. The major barriers towards realistic application are the low mobility and high operating voltage of the devices as well as their operational stability. The first OTFT was reported in 1986, the active material being the conducting polymer polythiophene [1]. The reported carrier mobility was order of 10^{-5} cm^2/Vs. Three years later, Horowitz and his collaborators [2] reported OTFTs fabricated with vacuum-evaporated sexithiophene, conjugated molecules acting as a semiconductor, increasing the carrier mobility two orders of magnitude.

The planar aromatic molecules, collectively known as polyacenes, are a promising class of molecular semiconductors for applications like thin film transistors. The prototypical molecule in this class is pentacene (Pn). As presented in Fig. 1.2, it consists of five benzene rings fused in series. This material is emerging as the most

widely-used p-type active layer in OTFTs. In general, Pn films are grown by vacuum vapor deposition, a technique which allows the control of important parameters like the chamber pressure, substrate temperature, and deposition rate.

Initially, the field-effect mobility for holes achieved in Pn-based OTFTs was approximately 10^{-3} cm^2/Vs [3]. This value was dramatically improved by purifying the starting material and controlling the organization of the molecules on the oxide substrate of the TFT [4, 5]. Organic thin film transistors fabricated with highly ordered pentacene thin films have demonstrated the best device performances. The highest reported mobility for pentacene TFTs on silicon oxide is 0.7 cm^2/Vs [6].

Better organization of the molecules was obtained by modifying the surface of the oxide with an organic monolayer prior to the pentacene deposition. Using octadecyltrichlorosilane (OTS) treated silicon oxide gate dielectric, the field effect mobility was improved to 1.5 cm^2/Vs [7]. A much better mobility, up to 6 cm^2/Vs, has been reported using a thin film of polystyrene prior to the pentacene deposition [8].

With such high values of the mobility that are currently being obtained in Pn TFTs, these devices are becoming good candidates for fabrication of large area, cost-effective organic electronics, that are compatible with flexible polymeric substrates. However, aspects like transport properties, device stability in ambient conditions, reproducibility, reliability, and gate-voltage induced decrease in the source-drain current need to be addressed.

In this chapter we introduce the crystal structure of pentacene and a general description of the electronic states. Further, we present experimental results and

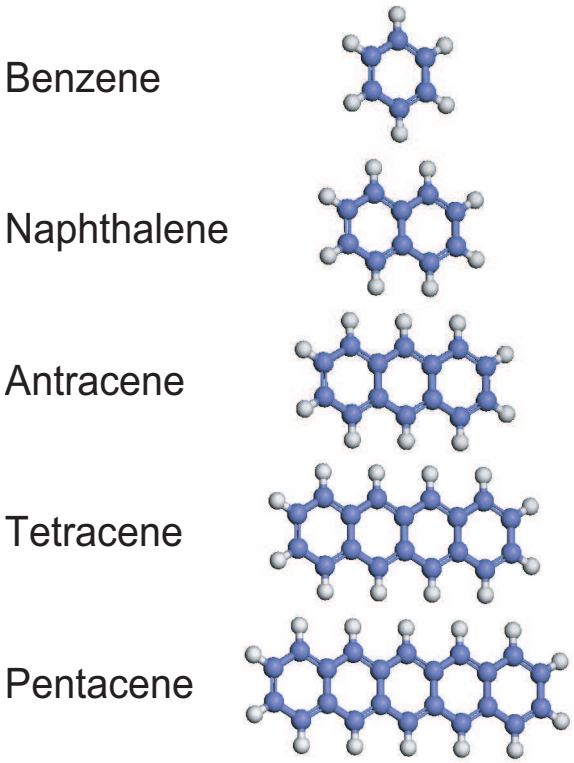

Figure 1.2: The molecular structure of the first polyacenes.

theoretical interpretations reported in the literature, which address the unresolved topic of transport properties in organic crystals.

1.2 Crystal Structure of Pentacene

Van der Waals intermolecular interactions affect the manner in which the polyacenes crystallize. Their molecular arrangement is influenced by the shape of the molecules which determines the topography of the van der Waals interaction surface. The maximum density of molecular packing is reached when energy surfaces of adjacent molecules are complementary to each other, resulting in a minimum of the potential energy of the lattice [9]. This complementary principle explains why relatively symmetrical linear polyacene molecules form the lowest lattice symmetry types.

The crystal structure of pentacene has been a subject of study since the early sixties [10, 11]. The crystal data reported by Campbell [10] shows that the Pn crystal is triclinic (a = 7.93 Å, b = 6.14 Å, c = 16.03 Å, $\alpha = 101.9°$, $\beta = 112°$, $\gamma = 85.8°$) and belongs to the space group P1 with two molecules per unit cell, with the symmetry centers situated at $(0, 0, 0)$ and $(1/2, 1/2, 0)$. The Pn molecules form a Herringbone structure, characterized by the layer periodicity $d(001)$ = 14.4 Å (See Fig. 1.3). Similarities of the crystal structure of the polyacene series from naphthalene to Pn have been observed [12, 13, 14].

The morphology of pentacene thin films was first studied by Dimitrakopoulos *et al.* [4, 15] using X-ray diffraction. In these reports, the authors investigated the

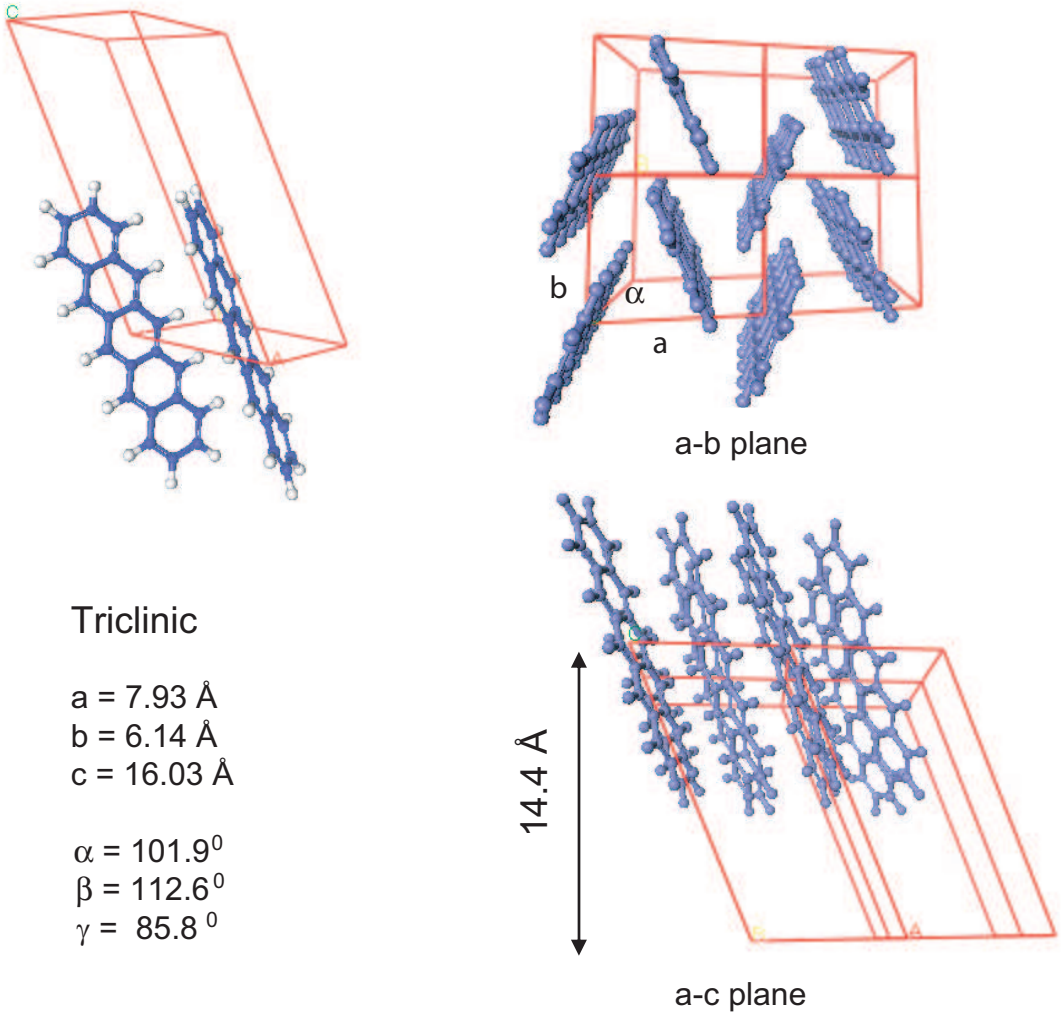

Figure 1.3: The crystalline structure of pentacene.

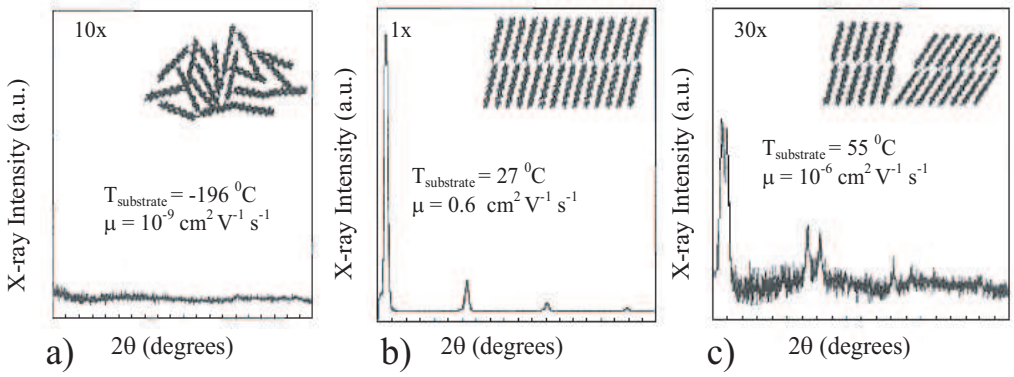

Figure 1.4: X-ray diffraction spectra of pentacene thin films deposited at different temperatures of the substrate [15]: a) $T_{substrate} = -196°$C; b) $T_{substrate} = 27°$C; a) $T_{substrate} = 55°$C.

effects of the substrate temperature and deposition rate on the film morphology. For the temperature of $-196°$C and the deposition rate of 0.5 Å/s, an insulating film was obtained, characterized by disorder and a limited overlap of the nearest neighbor molecular orbitals, as presented in Fig. 1.4 a). When the substrate was kept at room temperature during deposition, a very ordered film was deposited. In this case, the measured hole mobility was 0.6 cm^2/Vs. The structure of this film was characterized by a layer periodicity $d(001) = 15.4$ Å and was referred to as the "thin film phase" of pentacene. The coexistence of the thin film phase and the single crystal phase, characterized by layer periodicity 14.4 Å, was observed in films deposited at a substrate temperature of 55°C with 0.5 Å/s deposition rate. In this case, the measured mobility was very low, and the authors suggested that

a high concentration of defect resulting from the coexistence of the two phases is responsible for the observed low mobility.

More recent investigations have revealed the existence of four polymorphs of pentacene, with the $d(001)$ spacing of 14.1, 14.4, 15.0 and 15.4 Å[16]. Single crystals usually adopt the tightest $d(001)$ spacing, 14.1 Å, while all four polymorphs are present in thin films. In agreement with others [17, 18], Mattheus et al. reported that the growth of the polymorphs depends on the deposition parameters and the nature of the substrate [16].

1.3 Electronic Structure of Pentacene

1.3.1 Electronic States in Pentacene

The carbon aromatic ring structure of Pn is responsible for its semiconducting properties. The chemical bonding of the carbon atoms in aromatic molecules is characterized by three sp^2 hybridized orbitals at angles of 120° within the plane, and a p orbital perpendicular to this plane. One of the sp^2 orbitals covalently bonds with a hydrogen atom, while the other two bind neighboring carbon atoms creating two types of molecular orbitals: a bonding molecular orbital, σ, and an antibonding molecular orbital, σ^*. These chemical bonds are responsible for the structure of the Pn molecule. On the other hand, the overlap between the p orbitals account for the low-energy electronic properties of pentacene. The overlap of two p orbitals creates a π bond. Whereas σ and σ^* orbitals concentrate electrons along the axis between the nuclei of the C atoms, the electron density associated with the π and π^* orbitals

is above and below this axis.

Electrons occupy the energy levels up to the π orbital, thus making it the highest occupied molecular orbital (HOMO). Consequently, the π^* orbital form the lowest unoccupied molecular orbital (LUMO). Thus, lowest energy interband optical transition in Pn corresponds to the π-π^* transitions. The HOMO (LUMO) of a π bond in a molecule is analogous to the valence (conduction) band-edge in a crystalline semiconductor. Due to this analogy, the energy difference between HOMO and LUMO is called the optical band gap. The optical band gap for polyacene crystals are: 4.40 eV for anthracene, 3.43 eV for tetracene, and 2.83 eV for pentacene [9].

However, the term band gap for an organic semiconductor can be used with different meanings in different settings. The difference between the ionization potential and the electron affinity is called the adiabatic band gap, and has a different value than the optical band gap. When an electron is taken away from the HOMO or added to the LUMO of a neutral molecule, the molecular orbitals and the position of the nuclei relax to a slightly different minimum energy. As a consequence, the HOMO and LUMO are shifted. These deformed ionized molecules are referred to as molecular polarons, in analogy with inorganic semiconductor terminology. The energy difference between the vacuum level and the shifted HOMO is defined as the ionization potential, whereas the energy difference between the vacuum level the shifted LUMO is called electron affinity. Thus, the formation of the molecular polarons determines the adiabatic band gap. Photoconductivity experiments reveal that the adiabatic band gap for polyacene crystals decreases from 4.10 eV for

anthracene to 3.13 eV for tetracene, and to 2.47 eV for pentacene [9].

1.3.2 Optical Excitations in Pentacene

When an electron in an isolated molecule is excited from the HOMO into the LUMO, via the absorption of a photon, the π electron redistribute into the anti-bonding orbital. The excitation leads to a structural relaxation of the surrounding molecular geometry. Due to the attraction between the electron-hole pair created by the optical transition and the structural relaxation of the molecule, the energy difference between the excited state and the ground state is smaller than the adiabatic band gap.

When the molecule is embedded into a lattice of N molecules interacting with each other, the N-fold degenerate level corresponding to the noninteracting molecules will form a band of crystal states. The band width depends on the interaction between the neighboring molecules, while the center of the band is shifted downward with respect to the position of the free molecular level [19]. The electron-hole pair resulting from an optical transition between the ground state and an excited crystal state is called the Frenkel exciton, and the pair is characteristically located on the same molecule.

Davydov first applied Frenkel's exciton theory to organic crystals [20]. He showed that a molecular energy level may split into a number of components, determined by the number of translationally nonequivalent molecules per unit cell. For a crystal with 2 nonequivalent molecules, the crystal spectrum presents 2 bands

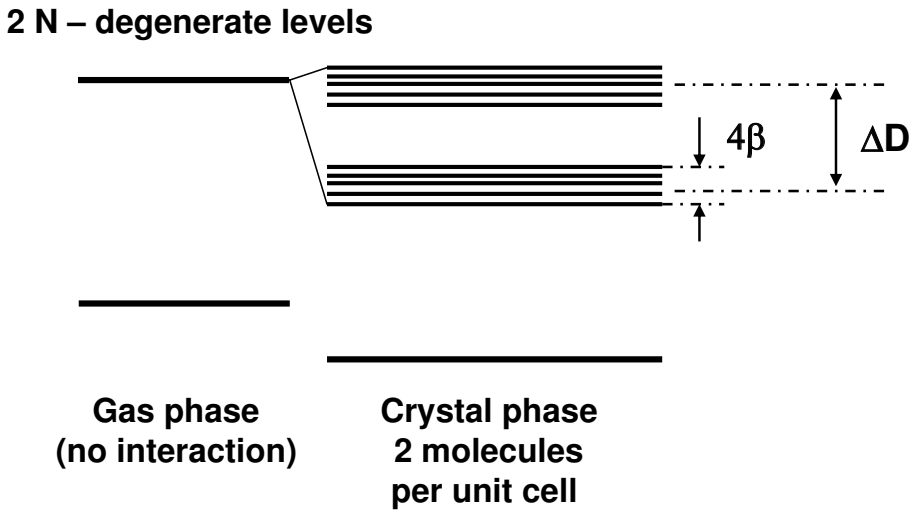

Figure 1.5: Splitting of the 2N-fold degenerate levels for a crystal with 2 nonequivalent molecules per unit cell. The Davydov splitting, ΔD, is determined by the interaction between the nonequivalent molecules. The band width depends on interaction between the neighboring molecules, β [19].

with a separation called the Davydov splitting, ΔD (see Fig. 1.5). The Davydov splitting is determined only by the nonequivalent intermolecular interactions. The band width 4β depends on the overlap of the atomic orbital wavefunctions between the neighboring molecules. The most convenient way to generate singlet excitons is by direct optical excitation. If a singlet exciton is generated in the highest Davydov band, it decays to the lowest-lying band. The excitons in the lowest-lying Davydov band have a longer life-time, and they may decay radiatively to the ground or pass to the triplet manifold $S_1 \longrightarrow T_1$ [19].

The reported Davydov doublet for Pn crystals is at 1.82 and 1.94 eV above the HOMO [21]. Pentacene polycrystalline thin films were also investigated and shown to have the singlet Davydov doublet at 1.83 and 1.97 eV [22]. The singlet excitons in the upper level of the Davydov doublet in Pn thin films were shown to relax, using pump-probe spectroscopy, to the lower excited state with a time constant less than 20 fs. Ref. [22] shows that the singlet excitons S_1 dissociate into pairs of triplet excitons T_1 with a rate of $1.3 \times 10^{13}\ s^{-1}$.

Another type of exciton characteristic of organic semiconductors is the charge transfer exciton. In this case, the excited electron is transferred to a nearest or next-nearest neighbor molecule, but it still remains correlated with the parent hole. The energy levels associated with charge transfer transitions can be calculated using the Rydberg formula,

$$E = E_G - \frac{e^2}{4\pi\varepsilon\epsilon_0 r_{CT}},$$

where E_G represents the energy required to ionize the molecule in the crystal and

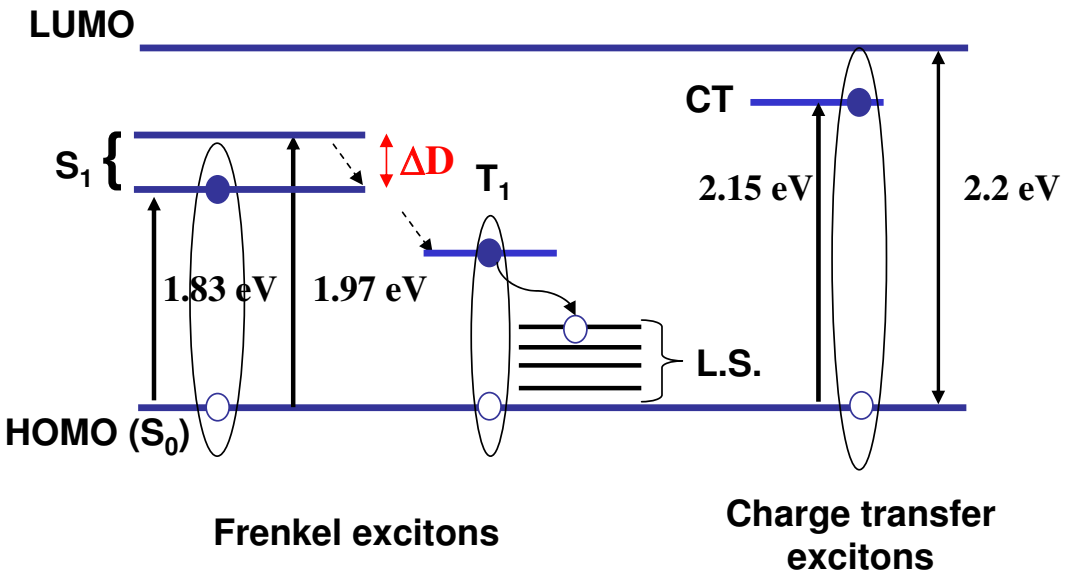

Figure 1.6: Diagram describing Frenkel (singlet and triplet intra-molecular) and Charge Transfer (inter-molecular) Excitons, CT, in Pn thin films. The singlet excitons, S_1, forming two bands separated by the Davydov split ΔD, dissociate in pairs of triplet excitons, T_1, with a rate constant of $1.3 \times 10^{13} s^{-1}$ [22]. The energies associated with the Pn bad gap and exciton states are provided by Ref. [21, 22, 23]. L.S. represent localized states situates in the Pn band gap.

r_{CT} is the separation distance [19]. In pentacene, charge-transfer excitons are associated with transitions to the three non-equivalent near-neighbor molecules. This is confirmed by electric field modulated absorption spectra of Pn films [23] in which existence of charge transfer transitions between the molecule located at (0, 0, 0), and the neighboring molecules located at (1/2, 1/2,0), (0, 1, 0) and (1, 0, 0) were observed. The corresponding reported energies are: 2.120 eV, 2.270 eV and 2.345 eV. For the crystal structure of Pn, please refer to Section 1.2.1.

1.4 Charge-Transport in Organic Semiconductors

Carrier transport in organic semiconductors is still not well understood. There are two types of models used to describe carrier transport in solids: band transport and hopping.

The Band Model applies to the case of a carrier which is highly delocalized, moving like a plane wave in a wide transport band, and having a relatively large mean free path. In this case, charge transport is limited by inelastic phonon scattering. Thus, one expects the mobility increases with increasing temperature because of the freezing out of the phonon excitations. The temperature dependence of the mobility goes like T^{-n}, where $n > 1$. It is generally considered that band transport applies in materials with carrier mobilities much larger than 1 cm^2/Vs. Glaeser and Berry [24] suggested that the band transport cannot be valid for organic semiconductors, since the mean free path of the carriers is comparable to the lattice constant. Indeed, for low temperature (T < 150 K), theoretical estimates in poly-

acene crystals have shown that the carriers along the a crystallographic direction are scattered at every lattice site [25, 26].

The Hopping Model applies to conduction in materials where the carrier is highly localized because of interactions with electronic and nuclear subsystems of the crystal. This model was developed to explain experimental findings in organic materials where the mobilities are much smaller than 1 cm^2/Vs. Holstein [27] pointed out that a strong electron-phonon interaction can cause "self-trapping" of an electron. Thus, electron transport is accompanied by an induced lattice distortion, forming a polaron. Polaron motion takes place via a succession of random jumps, in which the localized charge hops to a neighboring site. Each hop is associated with an activation energy, E_a. Therefore, the mobility increases with increasing temperature as $\exp(-E_a/kT)$.

However, organic molecular crystals have displayed mobilities of approximately 1 cm^2/Vs at room temperature or even higher [28, 29], and thus fall into an intermediate category. The description of charge transport in this regime is an active area of investigation because of the technological ramifications of building robust flexible organic devices. So we next briefly describe published experimental and theoretical studies addressing the temperature dependence of the mobility in organic crystals.

An experimental technique used to determine the mobility in molecular crystals is time-of-flight. The crystal is sandwiched between a rear metal electrode and a semi-transparent front electrode. In this technique, charge carriers of both signs are optically generated close to the front surface of the crystal using short laser pulses. If a positive potential is applied to the front electrode, the electrons are collected by

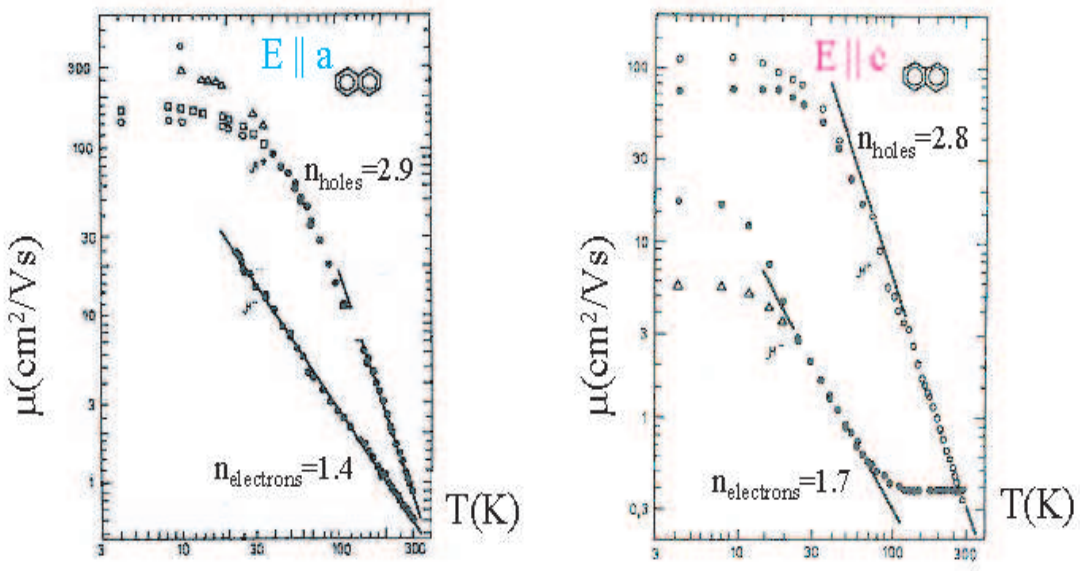

Figure 1.7: Electron μ^- and hole μ^+ mobilities versus temperature T, in log-log plot, in the a and c crystallographic directions of naphthalene [9].

the electrode while the holes drift through the bulk of the crystal. The drift velocity can be determined, which directly relates to the carrier mobility. Thus, the mobility values can be measured independently for both electrons and holes by changing the polarity of the sample.

Karl [30, 31] reported mobility measurements in naphthalene crystals, along both the a and c crystallographic directs, as presented in Fig. 1.7. For higher temperatures, a power-law dependence on temperature was measured for mobilities of both electrons and holes along the a crystallographic direction of naphthalene. The measured exponent for holes was higher than that of electrons, indicating that the mobility for holes increases faster than for electrons as the temperature is decreased.

It was also observed that for electrons the mobility along the c axis is independent of temperature between 100 and 300 K. Embracing an empirical approach, Karl [32] explained the T-independent mobility as a superposition of two different mobilities, corresponding to two types of carriers: $\mu_1 = aT^{-n}$ and $\mu_2 = b\exp(-E_a/kT)$. Others [33, 34] have suggested that a transition occurs at approximately 100 K between band-like transport, where the mobility goes like T^{-n}, and hopping transport, where the mobility is constant. However, the existing hopping models cannot explain a temperature independent mobility for a wide temperature range.

Silinsh [26] explains the temperature dependence of the mobility by introducing the nearly small molecular polaron (NSMP) model. The formation of NSMP was suggested by the observation that the mean time interval, τ_h, between separate hopping events in polyacene crystals is longer than the vibronic relaxation time of a molecule. A hopping time of $\sim 10^{-14}$ s was estimated using the intrinsic mobility of the carrier, $\tau_h = er_{ij}/(6\mu kT)$, where r_{ij} is the distance between two hopping sites in the polyacene crystal. The typical vibronic energy range, E_v, of 480 to 3000 cm^{-1} results in a vibronic relaxation time, $\tau_v = h/(2\pi E_v)$, of $1.7\times10^{-15} - 1.1\times10^{-14}$ s [9]. The fact that τ_h of the carrier on the lattice site is one order of magnitude greater than τ_v suggests that a strong coupling of the charge carrier with the intramolecular vibration modes should take place, resulting in the formation of a molecular polaron state. After the first scattering event, the carrier transforms into a heavy quasiparticle, and consequently obtains the corresponding effective mass of a molecular polaron, due to strong coupling with intramolecular vibrations. The NSMP moves farther by tunneling, without activation energy. To explain the temperature

dependence of the mobility as $\sim T^{-n}$, Silinsh suggested that the effective mass of the NSMP increases exponentially with temperature [9].

The temperature independent electron mobility in the c-direction in Nph crystals was explained as a coexistence of two quasiparticles. One is the NSMP, which moves without activation, $\mu_{NSMP} = aT^{-n}$, and a small lattice polaron (SLP) which moves by thermally activated hopping, and thus exhibits the typical exponential T-dependence $\mu_{SLP} = b\exp(-E_a/kT)$, where E_a is the activation energy. However, with exception of the c-direction in naphthalene, a SLP does not seem to form in polyacene crystals, since the characteristic relaxation time for intermolecular vibrations is $4.4 \times 10^{-14} - 1.1 \times 10^{-13}$ s, which is much longer than the residence time on the lattice site. Silinsh suggested that the carrier may be trapped in shallow defects with a large capture time. In this case, local deformations may be due to the interaction of the localized charge with dipoles that are induced on neighboring molecules, and thus form a SLP.

Recently, much effort has been invested in growing high quality crystals for a better understanding of transport properties [28, 29, 35]. Hole mobility in Pn crystals up to 35 cm^2/Vs at room temperature have been reported and a temperature dependence consistent with band like transport model, as presented in Fig. 1.8 [29]. However, when high quality crystals were used to fabricate field effect transistors, the extracted field effect mobility was orders of magnitude smaller, ranging between 0.1 and 0.5 cm^2/Vs [35]. Moreover, the temperature dependence of the mobility was found to be thermally activated at low temperatures and nearly temperature independent above 150 K, as presented in Fig. 1.9. In this case, the properties of

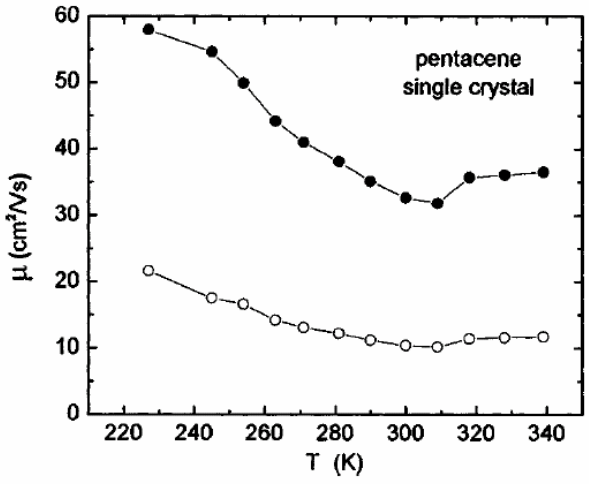

Figure 1.8: The temperature dependence of the hole mobility in Pn crystal, measured using the space charge limited current technique. A mobility of 35 cm^2/Vs at room temperature was obtained by purifying the starting material. The main chemical impurity eliminated in this process was pentacene quinone. The data is presented in Ref. [29].

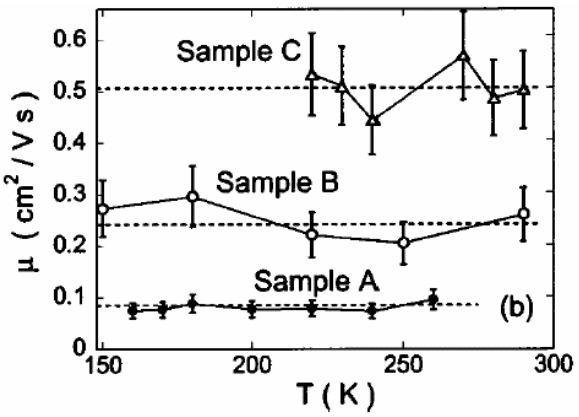

Figure 1.9: The temperature dependence of the field effect mobility in three transistors fabricated with single Pn crystals, reported in Ref. [35].

the transistor are determined by the pentacene-dielectric material interface.

From a practical point of view, thin films of organic semiconductors are important in order to fabricate cost-effective flexible electronics. These microcrystalline thin films incorporate grain boundaries, structural defects, and most probably chemical impurities in the active channel of the devices. Consequently, the transport properties become more complex and harder to elucidate.

1.5 Thesis Overview

In this thesis we investigate the thin film properties of pentacene by using an optical excitation technique. First, we describe in Chapter 2 our high vacuum evaporation system and the experimental techniques used to characterize thin film transistors fabricated with pentacene as active layer.

Next, we propose and develop photocurrent spectroscopy as a novel experimental tool to address transport properties in Pn TFTs. Direct current and photocurrent voltage characteristics are simultaneously measured, allowing for extraction of the field effect mobility and density of free carriers in the transistor channel as a function of the applied gate voltage. The results are presented in Chapter 3.

In Chapter 4, we use modulated photocurrent technique to extract information about the localized states in Pn TFTs. We model the photocarrier generation process as exciton dissociation via interaction with localized states. The experimental data is described using a gaussian distribution of localized states. Best fits to the data reveal that the position of the gaussian is located around 0.3 eV above the HOMO in Pn thin films. The influence of the dielectric material is also investigated.

Chapter 5 is reserved for practical applications of Pn TFTs. First, we describe a simple method to stabilize the current in these devices in order to evaluate the sensing capabilities of Pn TFTs. The transistor response to water vapor is addressed using Raman spectroscopy and electrical characterization. Further, we present a simple inverter circuit, fabricated with Pn transistors on flexible transparent substrates. This integrated circuit successfully modulated the output of a commercial liquid crystal display, suggesting that the viability of Pn TFTs for integrated circuits is promising.

Chapter 2

Pentacene Thin Film Transistors - Fabrication and Characterization Techniques

2.1 Overview

In this chapter we describe our high vacuum deposition system developed to fabricate and characterize pentacene thin film transistors. Further, we briefly introduce the characterization techniques and present the experimental set-ups used to investigate our devices.

2.2 Pn TFT Fabrication

2.2.1 Transistor Geometry

Fabrication of organic thin film transistors employed the two device geometries described as bottom and top electrode configurations, presented in Fig. 2.1. The active organic layer is a thin film, typically less than 100 nm, that is deposited on the gate insulator by thermal evaporation techniques. In the bottom electrode configuration the organic layer is incorporated into the device after the source and drain electrodes are deposited onto the gate dielectric. For the top electrode devices, the organic layer is deposited first, followed by the source and drain electrode

deposition.

Currently, Pn is the most promising organic material for p-type transistor applications. In these devices, efficient hole-injection is achieved through the use of source-drain electrodes with high work function. Gold is generally used for electrode fabrication in these devices because its work function is close to the position of Pn's HOMO level (work function of 5.1 eV). As alluded to above, the order of the deposition of the organic layer and the source-drain electrodes matters. A photoemission spectroscopy study [36] shows that there is a 0.5 eV hole injection barrier for Pn deposited on Au and 1 eV for Au deposited on Pn. In Fig. 2.1 we present an example of current-voltage characteristics for top and bottom electrode devices, fabricated under similar conditions. As can be discerned from the data, for the same applied voltages, the drain-source current for the bottom electrode transistor is one order of magnitude smaller, in agreement with other published reports [37]. In spite of a lower expected injection barrier, as suggested by the photoemission results, the overall contact resistance deduced from the I-V characteristics for bottom electrode configuration is larger. The contact resistance may increase due to a higher degree of disorder in the Pn film deposited on the edge of the Au electrode. This can be seen in Fig. 2.2, which shows a scanning electron microscope image of the contact morphology. *For the rest of the thesis, the devices that will be investigated are top electrode Pn thin film transistors.*

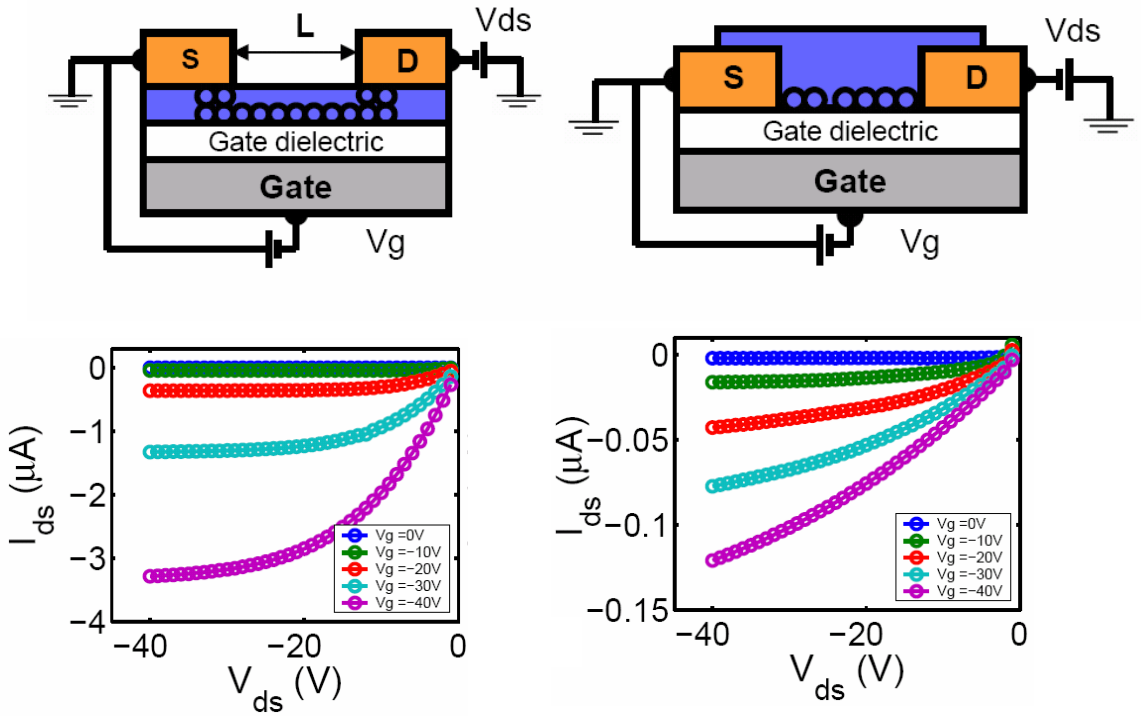

Figure 2.1: Schematics of two geometries for pentacene thin film transistors and I-V characteristics for top (right) and bottom (left) electrode Pn devices fabricated under similar deposition conditions.

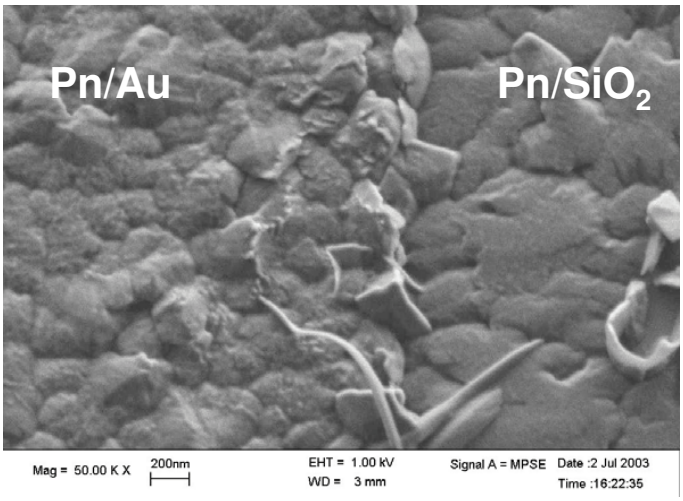

Figure 2.2: SEM image of 100 nm of Pn deposited on a 50nm Au/SiO_2 interface from left to right.

2.2.2 High Vacuum System

The experimental set-up used to fabricate our Pn thin film transistors (TFTs) is presented in Fig. 2.3.

2.2.2.1 Deposition Chamber

The MBE vacuum chamber is equipped with two effusion cells for Pn and gold deposition. In this chamber we prepare the Pn-TFTs in both bottom and top electrode configurations using shadow masks. The film thickness is monitored with a quartz-crystal microbalance. This vacuum chamber is evacuated with mechanical, turbo and cryogenic pumps. A base pressure of 10^{-9} Torr is routinely obtained.

Our typical devices are fabricated on degenerate n-type Si wafers with 5000

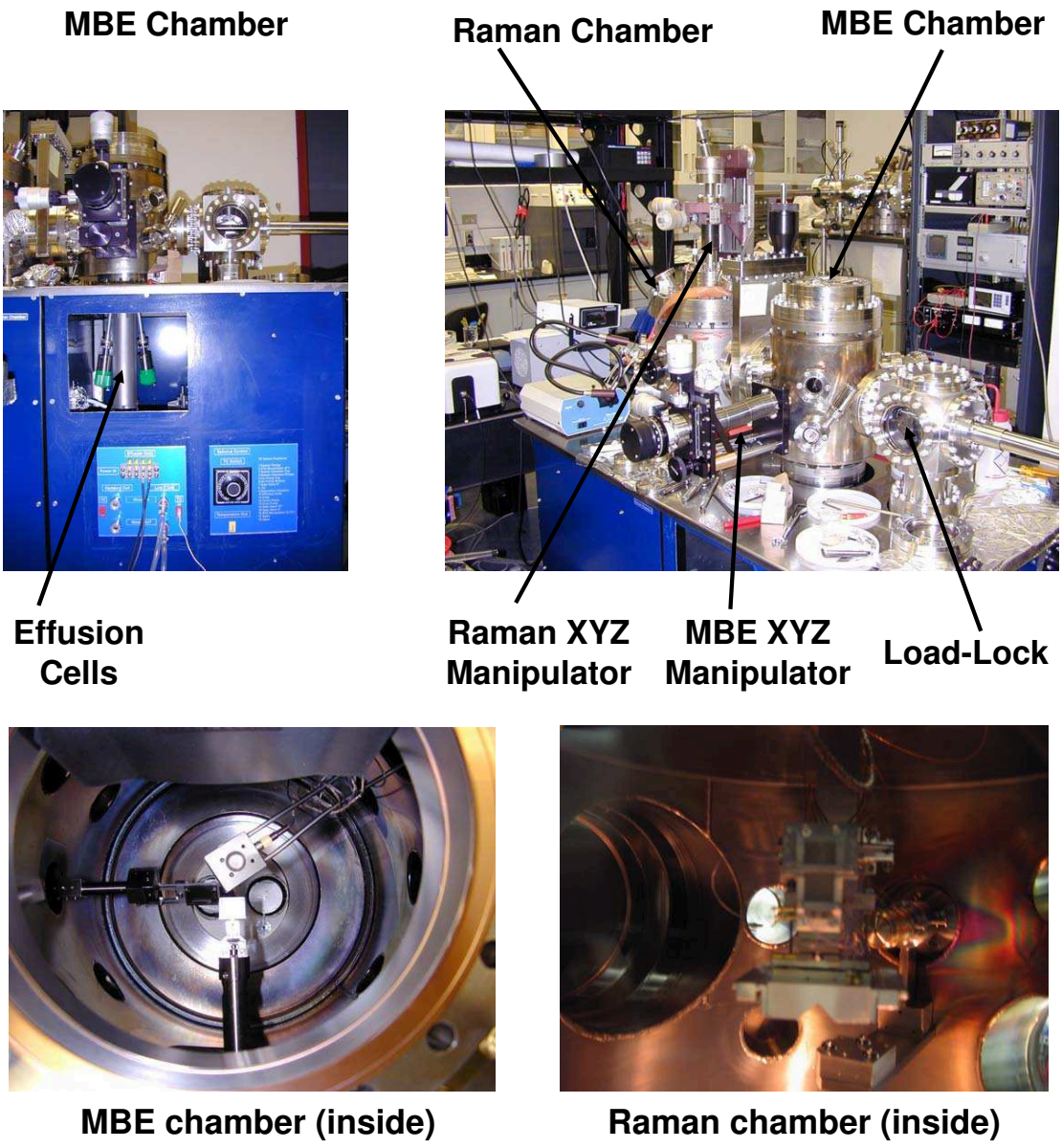

Figure 2.3: Molecular growth system and in-situ Raman characterization. The MBE chamber is equipped with two effusion cells for Pn and Au deposition. The film thickness is monitored with QCM. Inside the Raman chamber the sample is placed on a 3-axis MS5 nano-stage mounted on a kinematic stage for precise positioning in front of the in-situ Raman objective lens.

Å of thermal oxide as a dielectric. The wafers are sonicated in acetone for 5 min and rinsed with methanol and isopropanol prior to device fabrication. The pentacene, purchased from Aldrich without any further purification, is degassed at T = 120^{o}C for approximately 1 hour prior to the deposition, to sublime some of the pentacenequinone, a residue from the Pn synthesization process. The thin film is formed by vacuum sublimation at a pressure of approximately 5×10^{-9} Torr while the effusion cell temperature is kept at 180 ^{o}C. The films are grown at deposition rate of 0.1 Å/s while the substrate is held at room temperature. For higher deposition rates the performance of Pn TFTs degrades. The source and the drain electrodes are made from gold, with channel length of L = 100 μm and channel width W = 3 mm. The gold is evaporated through a shadow mask with a deposition rate of 7 Å/s to form a 100 nm thick film on top of the pentacene.

2.2.2.2 Raman Chamber

The Pn-TFTs fabricated in the deposition chamber can be transferred into a second chamber designed for in situ Raman spectroscopy. The sample is placed on a 3-axis MS5 nano-stage from Omicron (80 nm per step) mounted on a kinematic stage for precise positioning of the sample in front of the Raman objective lens (N.A. = 0.9), as can be seen in Fig. 2.3. The Raman vacuum chamber is evacuated with an ion pump with a titanium sublimation unit. Base pressure of 10^{-9} Torr is also obtained. A custom gas dosing system is also connected to the chamber.

2.3 Pn-TFT Characterization Techniques

2.3.1 Raman Spectroscopy

Raman spectroscopy can provide chemical information from light scattering by molecular vibrational excitation [38, 39]. This chemical information is contained in changes in the polarizability of the molecule, as part of the incident radiation is inelastically scattered by the Raman-active vibrational modes. The measured Raman scattered frequency, the difference between the incident and scattered photon frequency, corresponds to the vibration frequency of the molecule, providing a fingerprint for molecular binding. The technique can be used to characterize the purity of a sample or probe chemical interactions. We use Raman spectroscopy in Chapter 5 for testing possible chemical interactions between Pn and water vapor.

Our Kaiser Raman system consists of a 30 mW power He-Ne laser (see Fig. 2.4), fiber optic probe, axial transmissive spectrograph, and a CCD detector. The unpolarized 632.8 nm light is coupled to the filtered fiber optic probe and then to an objective lens, mounted on a dove tail, to deliver the incident laser radiation to the sample mounted inside the Raman vacuum chamber, as well as collect the inelastically scattered light in a back-scattering configuration. To probe the low-frequency vibrational modes, the collected light is passed to a pair of notch filters, which removes the directly reflected laser light and allows only the Raman scattered light to reach and be dispersed inside the spectrometer. The diffracted light is focused onto the CCD detector allowing the recording of a broad Raman spectrum at once. The spectral resolution of our system is 4 cm^{-1} and the spatial resolution

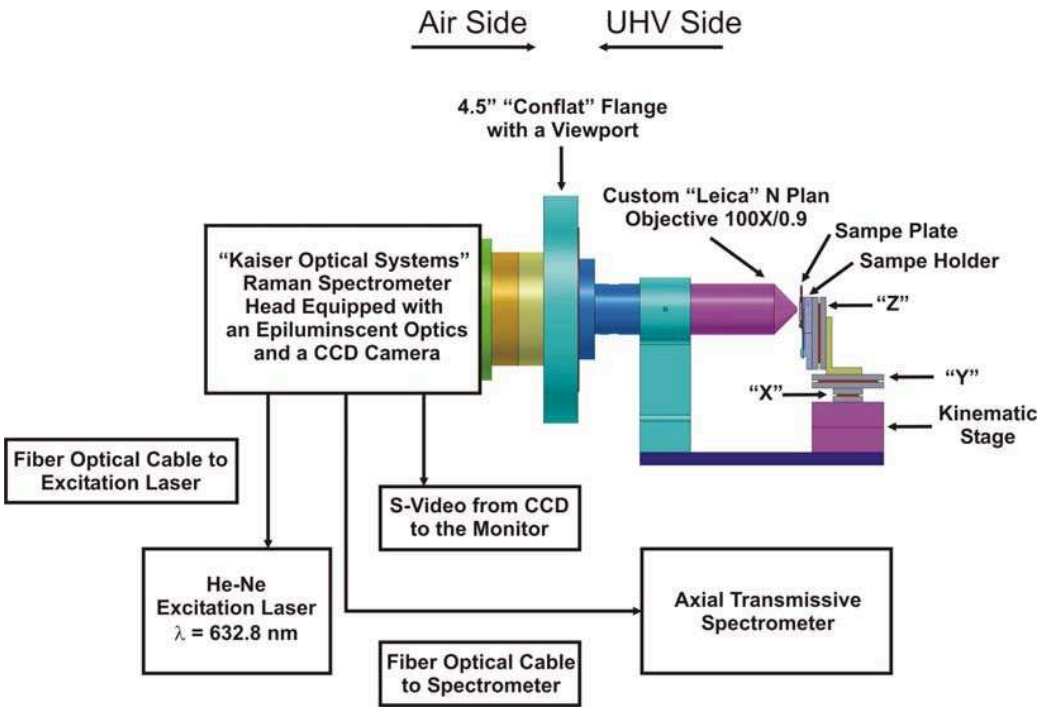

Figure 2.4: Confocal UHV Raman Microscope.

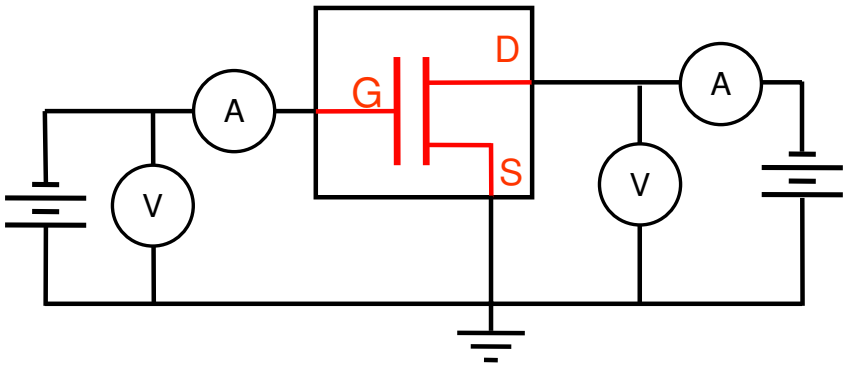

Figure 2.5: Electrical diagram for device characterization. The voltage supplies drive the transistor, one to sweep the drain-source voltage while the second one control the gate bias.

is 1.1 μm.

2.3.2 Electrical Characterization

The evaluation of the current-voltage (I-V) characteristics in a TFT provides information about the field effect mobility and the transistor threshold voltage. Transistor I-V curves are measured using two Keithley 2400 Source Meters. One is used to sweep the drain-source voltage and measure the current, while the other is used to increment the gate-source voltage, as seen in Fig. 2.5. The device is placed into a stainless steel vessel, presented in Fig. 2.6, designed to control the environmental conditions. The electrical measurements are performed in dry nitrogen. The vessel has a top and a bottom quartz window, which allow for optical investigations. LabView programs were written to control the experiments and acquire data and

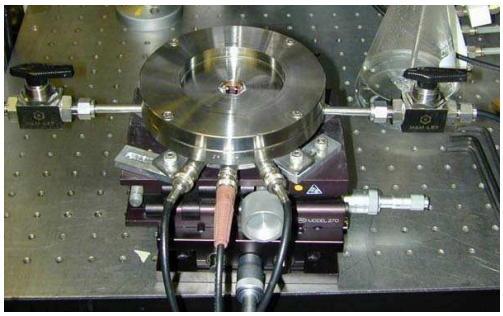

Figure 2.6: Stainless steel vessel designed for controlling the environmental conditions during the device characterization. The chamber has 2 quartz windows, top and bottom, to allow for transmission and photocurrent measurements.

MatLab programs were generated to analyze the results.

2.3.3 Photocurrent Spectroscopy

Photocurrent spectroscopy is a powerful probe of interband electronic transitions in a semiconductor. Such interaction of a semiconductor with light can lead to the creation of excess free carriers, which is detected as a photocurrent. The carrier generation by photoexcitation in general occurs via three different processes: 1) the transition of an electron from the valence band to the conduction band, 2) the transition between a localized state in the band gap and the delocalized transport bands, and 3) exciton creation and their subsequent dissociation to produce free carriers. We shall explore in detail the last process to investigate the effects of traps on charge transport in Pn TFTs. In Chapter 3 we develop this technique as a probe of the transport properties and in Chapter 4 we use it to extract information about

defect density of states.

We generate photocurrent in the Pn TFT using a tungsten-halogen lamp, whose output radiation is passed through a spectrometer with 0.5 nm spectral resolution to produce a narrow-band excitation. The experimental set-up is presented in Fig. 2.7. This excitation is mechanically chopped before passing through a set of lenses and ultimately through an objective lens (NA = 90) for a precise focusing on the transistor channel. The spot size is about 50 μm while the channel length is 100 μm. During the experiments the device is placed in the stainless steel vessel to assure a dry nitrogen environment.

The photocurrent is measured using phase-sensitive detection, where the chopper signal is used as the reference signal. The lock-in amplifier is connected in series with the source-meter biasing the drain-source electrodes. A second source-meter is used to control the gate voltage. LabView was used to control the experimental set-up. For a given set of drain-source and gate voltages, photocurrent spectra were accumulated in the 450-750 nm range. For every wavelength of the incident radiation, 10 photocurrent data sampled at 100 ms time interval, were averaged in order to improve the signal-to-noise ratio. Also, direct current and photocurrent voltage characteristics were generated for a fixed wavelength of the incident radiation and photocurrent magnitude and phase as a function of the modulation frequency.

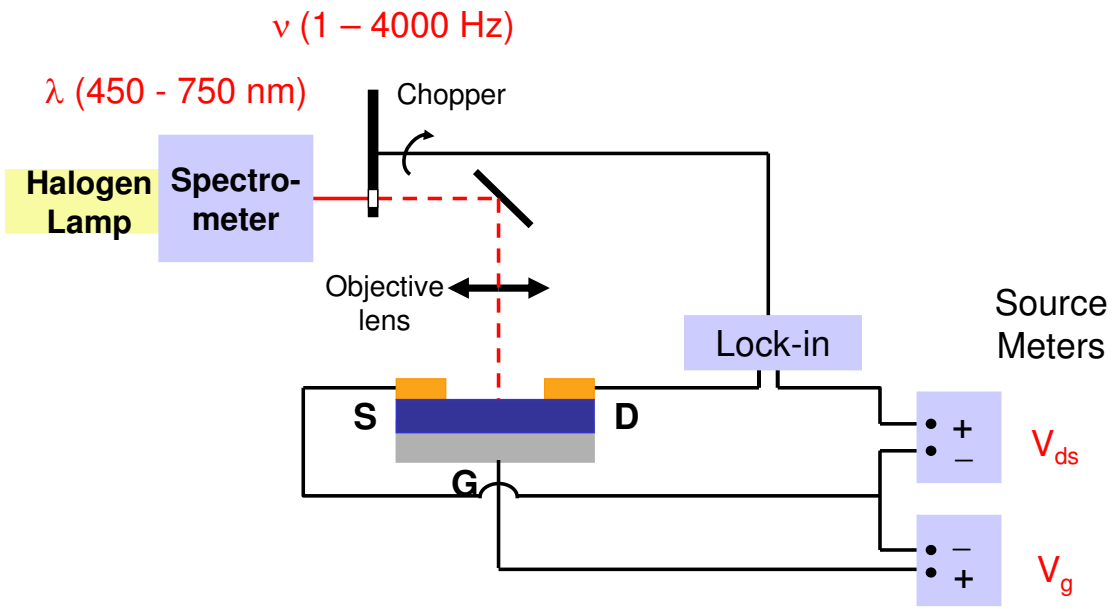

Figure 2.7: Experimental set-up for photocurrent measurements. For a given modulation frequency of the incident radiation, ν=100 Hz, we generate photocurrent spectra, η_p^λ, at fixed V_{ds} and V_g. Also direct current, $I_{ds}^{dc}(V_{ds},V_g)$ (measured with the source meter), and photocurrent $\delta I_{ds}^{\lambda}(V_{ds},V_g)$ (measured with the lock-in) voltage characteristics are measured, at fixed λ. The data is presented in Chapter 3. In Chapter 4 we present the photocurrent Magnitude and Phase as a function of the modulation frequency, $\omega = 2\pi\nu$, for a given wavelength of the incident radiation, λ=667 nm. For the last set of data the source meters are replaced with batteries for a precise phase recording.

Chapter 3

Charge-Transport in Pentacene Thin-Film Transistors

3.1 Overview

In this chapter we present different models used to describe charge transport in Pn TFTs. Further, we introduce the Photocurrent Spectroscopy as a technique that allows a model-free determination of the field-dependent mobility, and the free- and trapped-charge densities in actual TFT devices. Our results are in agreement with the widely accepted multiple-trap and release model of transport for organic TFTs [40, 41].

3.2 Pentacene Thin-Film Transistors: I-V Characteristics

The output characteristics for a top electrode Pn TFT are presented in Fig. 3.1. The bias voltage, V_{ds}, applied between the source and the drain drives the charge carriers in the transistor channel. The rise in the source-drain current, I_{ds}, with increasingly negative gate voltage, V_g, is associated with the electric field-induced modification of the charge carrier density in the channel. From analysis of the current-voltage characteristics, we can extract the transistor parameters and assess the performance of the device.

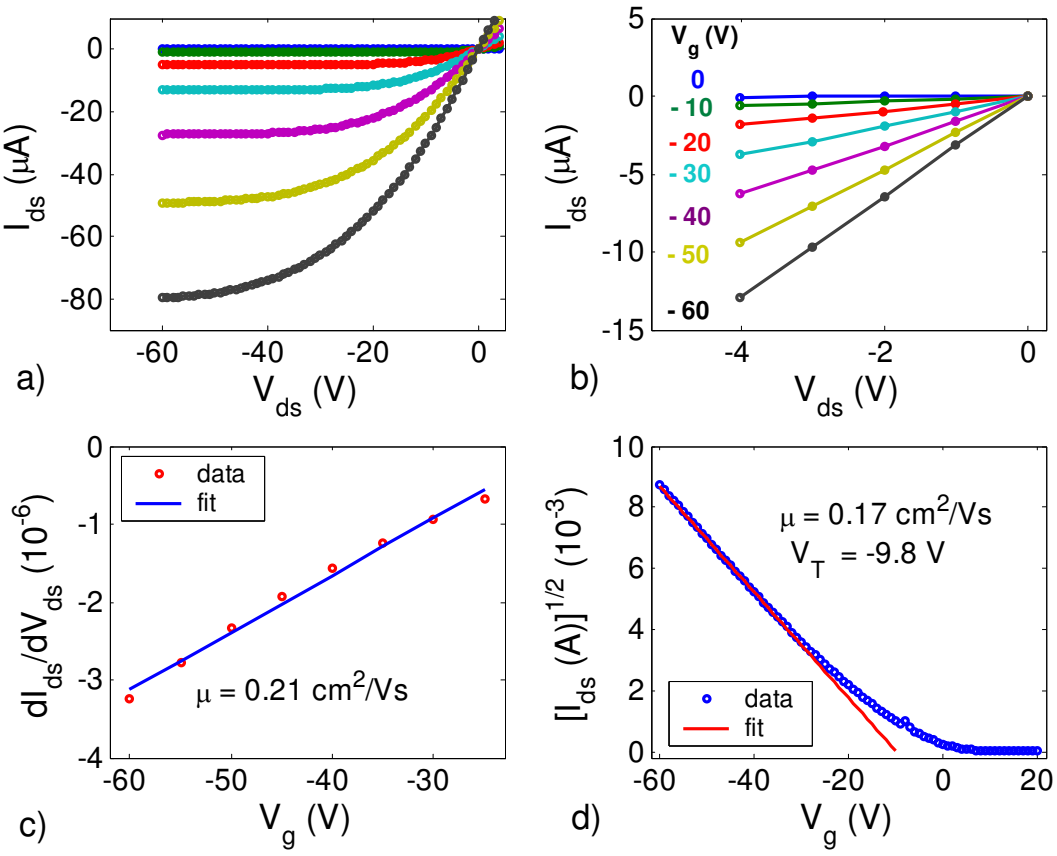

Figure 3.1: Typical I-V characteristic for our top electrode Pn/Au devices.

3.2.1 The Standard MOSFET Model

The current-voltage characteristics of organic thin-film transistors are widely-modeled by standard field effect transistor (FET) equations [44, 45]. In this case, the drain-source current for $V_{ds} > V_g - V_T$ is given by Eq. 3.1,

$$I_{ds} = \frac{WC_i}{L}\mu\left(V_g - V_T - \frac{V_{ds}}{2}\right)V_{ds}, \tag{3.1}$$

where L is the transistor channel length, W is the channel width, C_i is the capacitance per unit area of the insulating layer ($C_i = \varepsilon_0\varepsilon/t$, where t is the thickness of the dielectric layer), V_T is the threshold voltage and μ is the field-effect mobility. The threshold voltage physically represents the value of the gate voltage for which the channel conductance corresponds to the conductance of the whole semiconducting layer [45].

There are two limiting cases in Eq. 3.1 that are often used to extract the threshold voltage and mobility from the data. For small drain-source voltage, I_{ds} increases linearly with V_{ds}, which is exemplified in Fig. 3.1 b). From Eq. 3.1, this linear regime is approximated by,

$$I_{ds} = \frac{WC_i}{L}\mu(V_g - V_T)V_{ds}. \tag{3.2}$$

From Eq. 3.2, the mobility is determined from the slope of the channel transconductance, $\frac{dI_{ds}}{dV_{ds}}$, versus V_g. This analysis is demonstrated in Fig. 3.1 c). As V_{ds} is increased, a situation is reached in which the conducting channel is pinched at the drain electrode leading to the saturation of the source-drain current. This situation

occurs when $V_{ds} = V_g$ - V_T. Under this condition, the value of the saturation current is obtained as,

$$I_{ds} = \frac{WC_i}{2L}\mu \left(V_g - V_T\right)^2 . \tag{3.3}$$

It is readily seen in Eq. 3.3 that the saturation mobility is calculated from the slope of the plot of $(I_{ds})^{1/2}$ vs. V_g. Furthermore, the extrapolated intercept determines the threshold voltage. However, it is found that the values of the mobility and the threshold voltage obtained from the linear and the saturation regime do not often agree [45]. In our example, the parameters extracted using Eq. 3.2 are, μ = 0.21 cm^2/Vs and V_T = -17.3 V, while applying the FET model in the saturation regime yields a mobility of 0.17 cm^2/Vs and V_T = -9.8 V. The question naturally arises as to the validity of applying the standard FET equations in the analysis of OTFT performance. This model assumes a constant mobility, an assumption which does not hold for organic semiconductors [46]. The standard FET model has been extended to include a gate-dependent mobility [40, 43]. Multiple trap and release and variable range hopping models have been proposed as mechanisms for the field-dependent mobility. In the next two sections, we describe these models qualitatively.

3.2.2 The Multiple Trapping and Release Model

Organic thin films are typically amorphous or polycrystalline and have significantly lower carrier mobilities than the corresponding single crystalline material.

This is a consequence of the presence of localized levels in the energy gap related to grain boundaries, structural defects, or impurities which can act as traps for charge carriers. In amorphous silicon, the multiple trapping and release model is widely used to describe charge transport [47]. This model is based on a mechanism in which carriers moving in the extended levels are trapped by localized defects. The trapped carriers are eventually thermally released and participate in the conduction process. Dimitrakopoulos *et al.* [46] measured the mobility dependence on the gate electric field in Pn TFT using devices with different dielectric constants and the same gate voltages. They found that the carrier mobility initially increases linearly and eventually saturates with gate voltage. In addition, they showed that the mobility increases as the concentration of carriers in the channel region increases. Based on these results, Dimitrakopoulos *et al.* [46] concluded that the trapping and release model is applicable to carrier transport in thin films of pentacene.

The trapping-and-release model was developed by Horowitz and Delannoy [40]. This model can explain the increase in mobility as a function of the gate voltage, as observed experimentally [46, 48]. It is assumed that the low conductivity of organic materials is due to a large concentration of traps that limit the charge-carrier transport. During carrier transit through the delocalized levels, (valence band for p-type semiconductors) the charge carrier interacts with the localized levels through trapping and thermal release processes. As a charge carrier arrives near a trap, the probability of being trapped is close to one and the deep traps are filled first. When the gate bias is increased, the Fermi energy position approaches the delocalized band edge and more of the traps are filled. Consequently, the injected carriers are

free to move with a higher mobility. If all traps are filled, the field effect mobility approaches the mobility associated with carriers in the delocalized band.

3.2.3 The Variable Range Hopping Model

An alternative to the trapping-and-release model, applicable for amorphous organic films where the charge carriers are strongly localized, is the variable-range hopping model [42]. The model explains the carrier transport via hops from one localized state to another, with a constant distribution of localized states. Hopping is either phonon assisted or induced by an external electric field, with the carrier finding the site with the lowest activation energy and the shortest hopping distance. Motts Variable Range Hopping model predicts the temperature dependence of the mobility as $\mu \sim \exp[(-T_1/T)^{1/4}]$. This behavior is strongly dependent on the assumed distribution of localized states.

Vissenberg considers that the carriers accumulated in the transistor channel fill up an exponential distribution of localized states such that the higher the energy the lower the activation energy needed to hop to a neighboring site [43]. Moreover, the carriers that have a higher activation energy will hop a shorter distance than the ones with a lower activation energy. Since the carrier mobility is determined by its mean free path, an increase of the mobility with the applied gate voltage can be explained because the activation energy decreases with the applied gate voltage. Furthermore, the model predicts an exponential dependence of the mobility with temperature, $\mu \sim \exp(-E_a/kT)$, where the activation energy, E_a, depends on the

applied gate voltage.

The above two models describe the transport properties in organic semiconductors and both predict gate voltage-dependent mobilities in organic semiconductor devices. However, choosing one over the other to describe real Pn TFTs is still debatable.

3.3 The Photocurrent Spectroscopy as a Model-Free Technique for Extracting Organic Thin-Film Transistor Characteristics

We now introduce Photocurrent Spectroscopy as a model-free probe of the transport properties in Pn TFTs. First, we present the experimental data before describing the use of the technique to characterize our devices.

The photocurrent was generated using the experimental set-up presented in Chapter 2, with the excitation modulated at 100 Hz. For a given set of drain-source and gate voltages, photocurrent spectra were accumulated in the 450-750 nm range, as seen in Fig. 3.2. For every wavelength of the incident radiation, 10 photocurrent measurements were averaged in order to improve the signal-to-noise ratio. Also, direct current (Fig. 3.5) and photocurrent (Fig. 3.6) voltage characteristics were generated for a fixed wavelength of the incident radiation. From a parallel analysis of these characteristics, presented in the following sections, we were able to extract the field effect mobility and the density of carriers in the transistor channel as a function of the applied gate voltage.

3.3.1 Photocurrent Spectra in Pentacene Thin Film Transistors

In Fig. 3.2 we present a typical photocurrent spectrum measured in Pn TFT fabricated on SiO_2. The spectrum was measured over the energy range 1.7-2.7 eV to explore the transitions below the Pn band gap. To correct for the response of the spectrometer system, the photocurrent spectrum was normalized to the absolute lamp spectrum measured with a calibrated Si photodiode. We estimate the photocurrent yield spectrum as

$$\eta_P^{\lambda} = \frac{hc}{e}\frac{\delta I_{ds}^{\lambda}}{P\lambda},$$

where δI_{ds}^{λ} is the measured source-drain photocurrent and P is the incident power on the device channel at the photon wavelength λ.

The first two excitonic bands correspond to the Davydov-split singlet excitons, and they are in agreement with previous reports for bulk Pn [22, 23]. In the 2.1-2.6 eV energy range, we observe the charge transfer (CT) excitonic bands. We clearly can resolve the bands at 2.13 and 2.28 eV in agreement with Sebastian's results [23].

Photocarrier generation associated with singlet exciton formation in Pn has been attributed to the interaction of triplet excitons with trapped holes, where the triplet excitons are created by dissociation of the singlet excitons [21, 22, 49]. In this process only excess free holes are created. However, we do not have information about the photocarrier generation process involving CT excitons. Since the binding energy for the CT excitons is smaller than for singlet excitons, it is possible that the applied electric field on the transistor configuration could separate the CT excitonic electron-hole pair in order to produce free carriers.

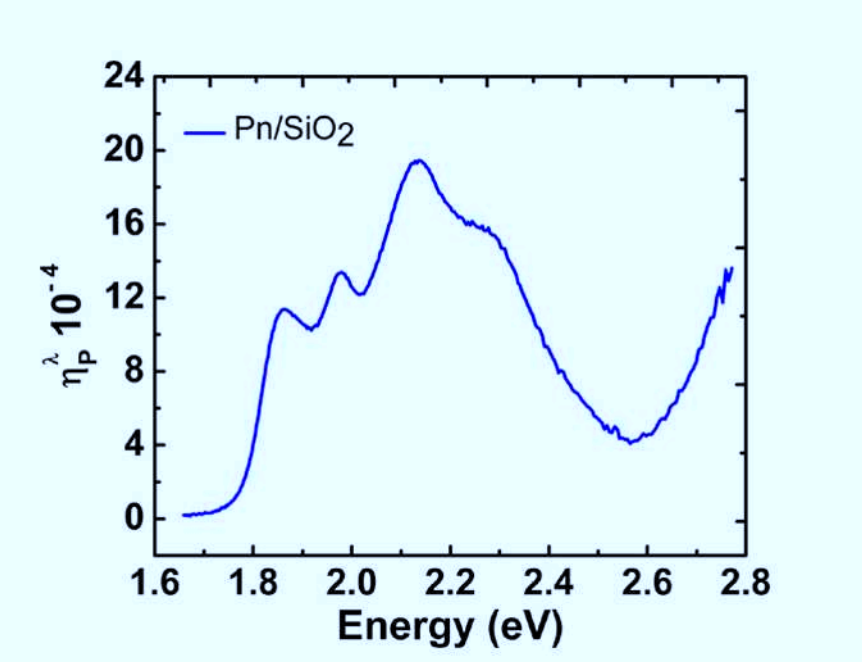

Figure 3.2: Photocurrent spectrum for Pn TFT fabricated on SiO_2. The two low-energy peaks at 1.86 eV (667 nm) and 1.97 eV (630 nm) have previously been identified [22, 23] as transitions to the Davydov-split singlet excitons [22] while the ones at 2.13 eV and 2.28 eV are charge-transfer transitions between pentacene molecules [23].

3.3.2 The Gate Voltage Dependence of the Photocurrent Spectra

Fig. 3.3 presents a set of photocurrent spectra measured for a Pn TFT at different gate voltages. Taken at a constant source-drain voltage $V_{ds} = -25$ V, the data show a linear rise in the photocurrent yield with increasing V_g. In this section we demonstrate that this observed increase in the photocurrent with the applied gate voltage is related to the well known gate-voltage increase of the mobility in organic TFTs reported earlier [46, 50, 51, 52].

One possible explanation for the gate-voltage dependence of the photocurrent spectrum is field enhanced light absorption. We investigated this possibility in Pn films by using electroabsorption measurements. In general, the electroabsorption signal is given by

$$d\Delta\alpha(h\nu) = -\frac{\Delta T}{T} = Im\chi^{(3)}(h\nu)E^2,$$

where $\Delta\alpha$ is the variation in the absorption coefficient, $h\nu$ is the photon energy of the incident radiation, T is the transmission through the organic film characterized by the thickness d, $Im\chi^{(3)}$ is the imaginary part of the third-order susceptibility, and E is the applied electric field [53]. For an externally applied sinusoidal electric field, $E = E_0 \sin(\omega_0 t)$, the electroabsorption is modulated at the second harmonic frequency of the applied ac voltage. This contribution can be detected by the lock-in technique.

We prepared transparent Pn films, with thickness of 400 nm, on quartz covered with patterned ITO. A subsequent transparent Al electrode was evaporated onto the organic material. The sample was positioned inside the test chamber with

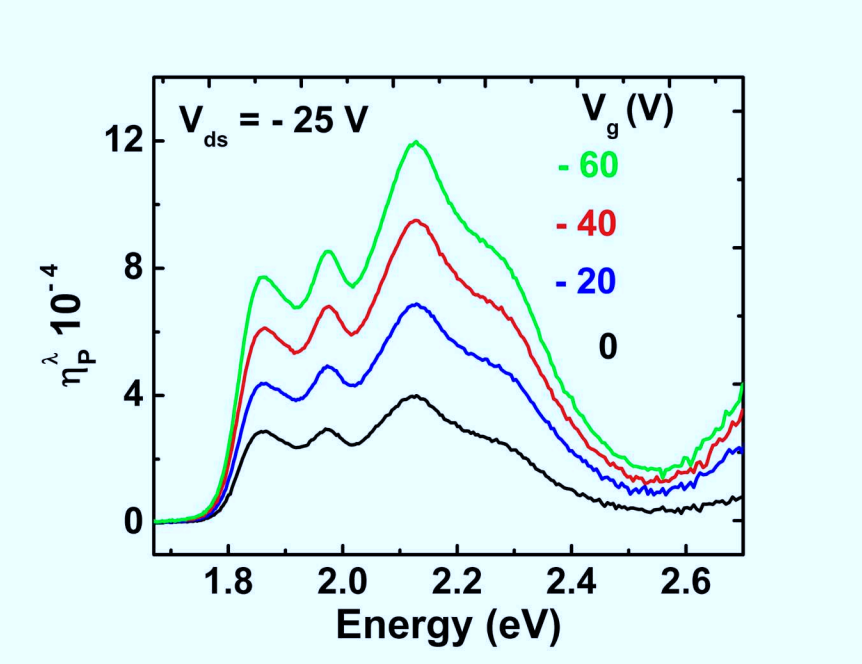

Figure 3.3: Photocurrent yield spectra measured at different gate voltages. We observe a linear increase of the photocurrent in agreement with an increase of the carrier mobility with the applied gate field.

a photodetector underneath to allow transmission measurements. The external electric field applied on the ITO/Al electrodes, with an amplitude of 1.2×10^5 V/cm (the same order of magnitude with the applied gate electric field in the transistor configuration), was modulated at a frequency of 1000 Hz. The amplified signal from the detector, ΔT, was recorded with a lock-in amplifier at the second harmonic of the applied external field frequency, while the incident radiation was swept between 450-750 nm. The direct output of the detector, T, was also recorded in order to calculate the change in absorption coefficient. The data, $\Delta T/T$, is presented in Fig. 3.4.

Absorption spectra were also measured in order to extract the absorption coefficient, α, for the 450-750 nm spectral range. Since our electroabsorption measurements on Pn films yield a voltage-induced change in the absorption of $\frac{\delta\alpha}{\alpha} \sim 10^{-4}$ (consistent with previous results [23]), we can reject the variation in the photoexcitation rate with gate voltage as a possible explanation of the observed gate-voltage dependence. It follows that the singlet-to-triplet transition rate is also unlikely to be sensitive to the changes in the gate voltage, since similar physical mechanisms are involved.

3.3.3 Photocurrent vs Direct Current Voltage Characteristics

We measured the V_{ds} dependence of the photocurrent at photon wavelengths corresponding to the singlet exciton peaks because the exciton dynamics are well established. Figure 3.5a displays typical $\delta I_{ds}^{\lambda} - V_{ds}$ characteristics obtained at $\lambda =$

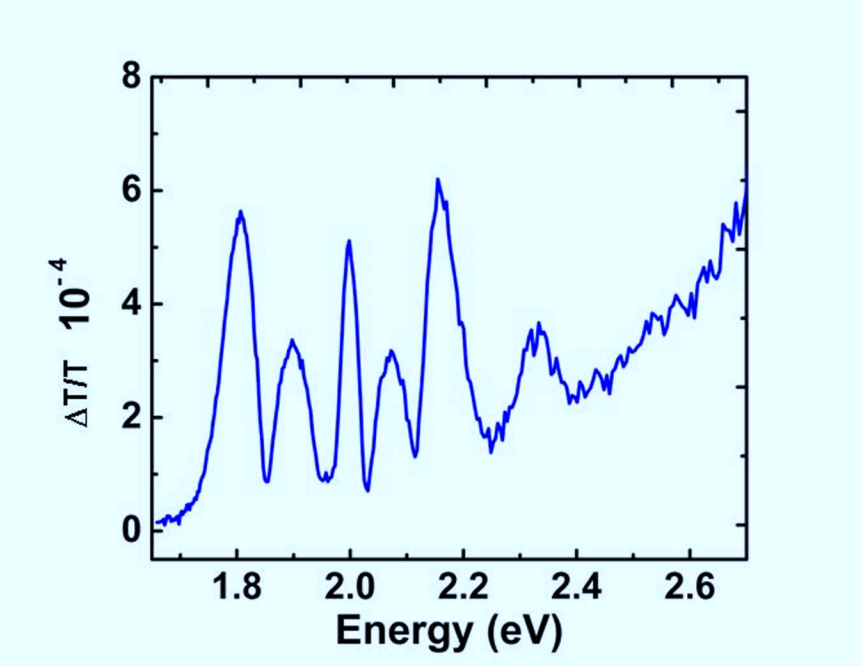

Figure 3.4: Electroabsorption spectrum in a Pn thin film in the presence of an external sinusoidal electric field with amplitude of 1.2×10^5 V/cm.

630 nm. The photocurrent δI_{ds}^{λ} increases linearly with V_g for any V_{ds} over the entire range of our measurement, as shown in Fig. 3.5b, consistent with the behavior of the photocurrent spectra in Fig. 3.3.

In contrast, the V_g dependence of the direct source-drain current, I_{ds}^{dc}, illustrated in Fig. 3.6, is initially linear below $V_{ds} \sim 5$ V followed by quadratic V_g dependence at higher V_{ds}. The total current is also three orders of magnitude larger than the photocurrent. Thus, the modulation in the device behavior introduced by the photocurrent is a minor perturbation.

3.3.4 Implications on Charge-Transport

To account for the different gate voltage dependence between the photocurrent and the direct current, recall the standard equation for the transistor source-drain current neglecting the contribution from diffusion current and assuming a two-dimensional conduction channel for holes:

$$I_{ds}^{dc} = -e\frac{W}{L}\int_0^{V_{ds}} \mu\left(V_g, V\right) n\left(V_g, V\right) dV, \tag{3.4}$$

where e is the electronic charge, V is the voltage at any point along the channel and the quantities $n\left(V_g, V\right)$ and $\mu\left(V_g, V\right)$ are the voltage dependent carrier density within the channel and the hole mobility, respectively. The photocurrent is characterized by the density of photoinduced charge carriers δn_{λ} in the channel. To evaluate δn_{λ} we assume (to be tested later) that there are sufficient trapped holes at $V_g = 0$ V to maintain a steady-state de-excitation rate of the triplet excitons.

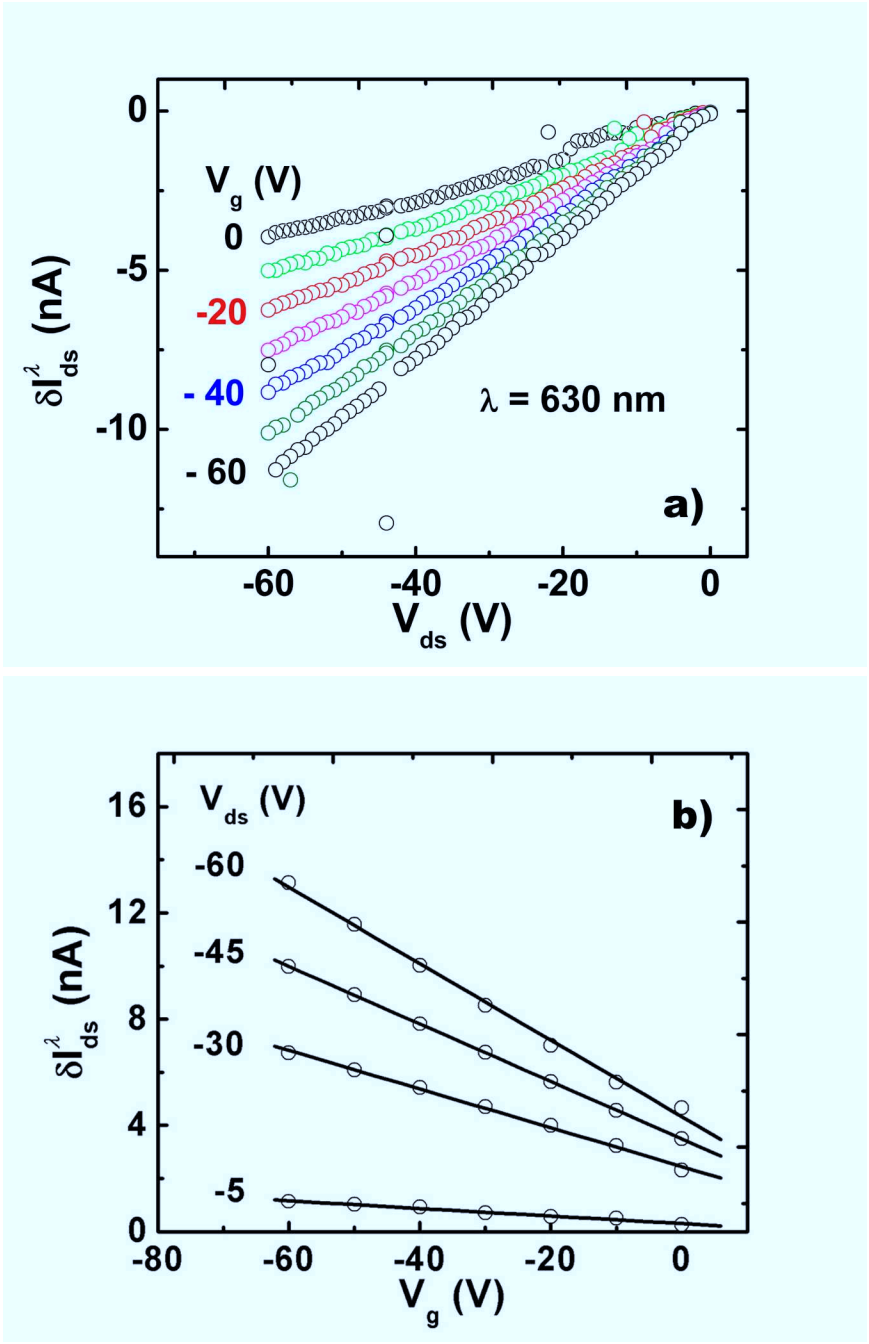

Figure 3.5: Photocurrent voltage characteristics measured with incident wavelength tuned to the second singlet excitation (1.97 eV). The lower graph presents the gate voltage dependence of the photocurrent for various source-drain voltages. The lines are linear fits to the data.

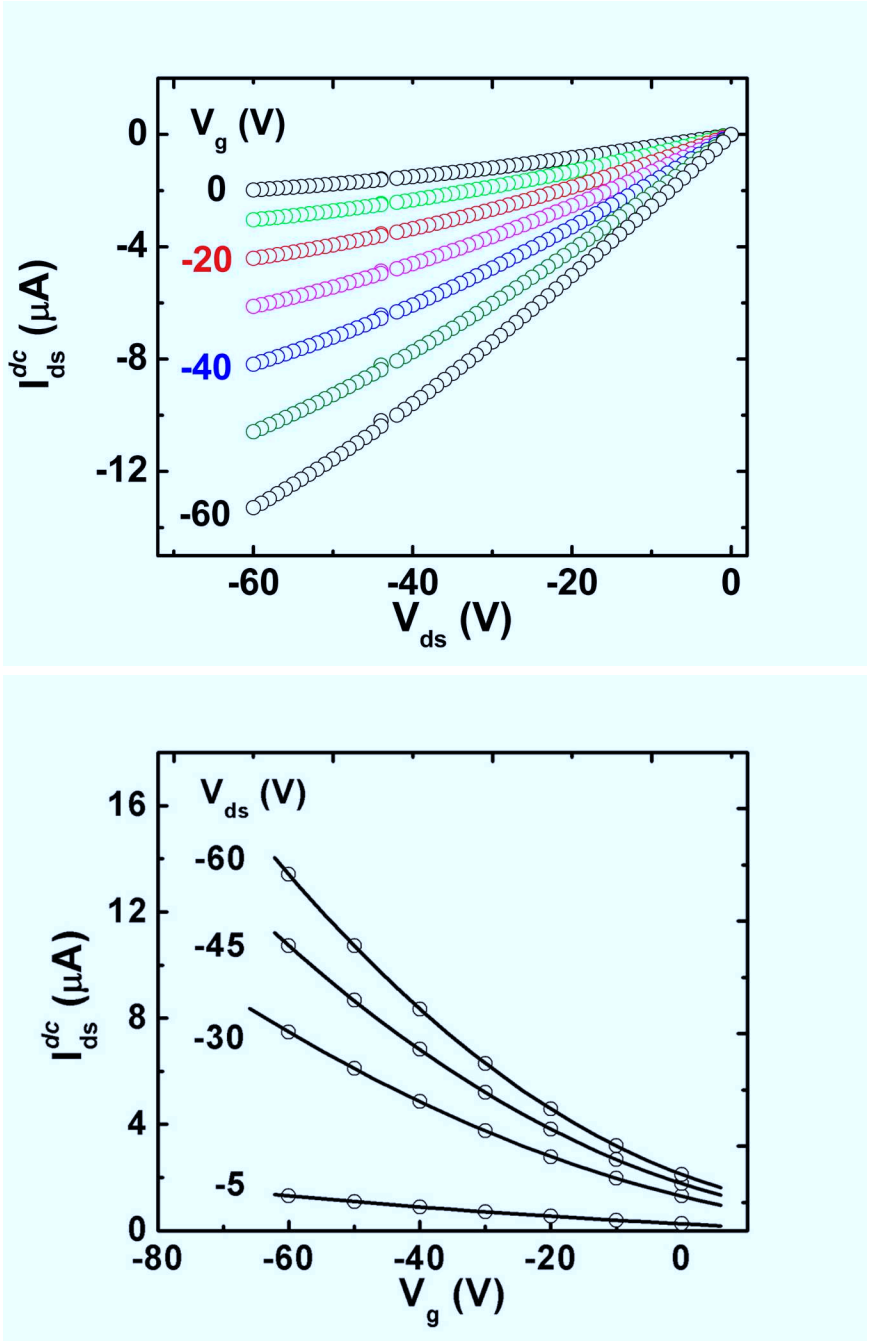

Figure 3.6: Direct current voltage I-V curves for various gate voltages. The lower graph presents the gate voltage dependence of the direct current for various source-drain voltages. The lines are quadratic fits to the data.

Vg(V)	a $(10^{-9}A/V)$	b $(10^{-12}A/V^2)$	μ_0 (cm^2/Vs)	α_0 (V^{-1})
0	0.0833	0.0519	0.0296	0.0012
-10	0.1288	0.5453	0.0458	0.0085
-20	0.1601	0.6616	0.0569	0.0083
-30	0.1814	0.6056	0.0645	0.0067
-40	0.1968	0.4826	0.0700	0.0049
-50	0.2155	0.3651	0.0766	0.0034
-60	0.2304	0.1884	0.0819	0.0016

Table 3.1: The parameters for the second order polynomial fit to the photocurrent voltage characteristics and the extracted hole mobility.

For the modulation frequency used in our experiment, 100 Hz, we can assume a quasi-static condition, in which case Eq. 3.4 provides a good approximation for the photocurrent. Thus, the photocurrent contribution is analogously given by,

$$\delta I_{ds}^{\lambda} \simeq -e\frac{W}{L}\delta n_{\lambda}\int_{0}^{V_{ds}}\mu\left(V_g, V\right)dV \tag{3.5}$$

where δn_{λ} is taken out of the integral since it is assumed to be field independent. Equation 3.5 provides an integral equation for determining the mobility from the measured photocurrent I-V characteristics of the TFTs. In these calculations, $\delta n_{\lambda} \simeq \frac{\Phi N_{ph} T}{2WL}$ where Φ is the photocarrier generation efficiency and T is the modulation period of the incident photons N_{ph}. We estimate Φ using the experimental photocurrent yield $\eta_P^{\lambda} = \Phi \times G$ measured at $V_g = 0$ V [9]. The transit coefficient $G = 1 - \exp(-L'/L)$ is determined by the characteristic length L' that is linearly dependent on V_{ds} and the channel length L. A second-order polynomial fit to the

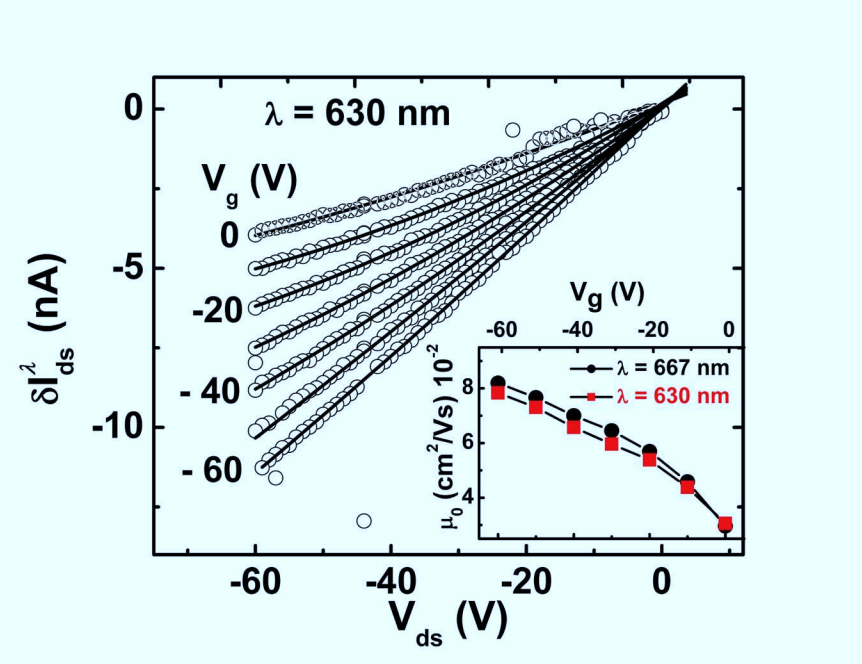

Figure 3.7: Photocurrent voltage characteristics measured with incident wavelength tuned to the second singlet excitation (1.97 eV). The lines are second order polynomial fits to the data as described in the text. Inset: gate voltage dependence of the hole mobility determined using Eq. 3.5.

Vg(V)	$A(10^{-6}A/V)$	$B(10^{-9}A/V^2)$	$C(10^{-11}A/V^3)$	$n_0(10^{11}cm^{-2})$	$\beta_0(V^{-1})$
0	0.0487	0.1586	-0.1200	3.4203	0.0053
-10	0.0765	0.3632	-0.0507	3.4762	0.0010
-20	0.1069	0.4623	-0.0879	3.9068	0.0004
-30	0.1407	0.4762	-0.2079	4.5383	0.0001
-40	0.1775	0.4096	-0.3927	5.2780	-0.0003
-50	0.2161	0.2418	-0.6447	5.8682	-0.0012
-60	0.2567	0.0112	-0.9171	6.5174	-0.0015

Table 3.2: The parameters for the third order polynomial fit to the direct current voltage characteristics and the extracted hole density.

photocurrent yield data in the low V_{ds} limit gives $\Phi \sim 1 \times 10^{-5}$ carriers per incident photon. To extract $\mu(V_g, V)$ from Eq. 3.5, the functional dependence of the photocurrent I-V characteristics is obtained phenomenologically by fitting the data in Fig. 3.7 to $-\delta I_{ds}^{\lambda} = aV_{ds} + bV_{ds}^2$ where a and b are fit parameters determined for each value of the gate voltage.

The quality of the fits to the data (correlation coefficient $R^2 = 0.99$) is indicated by the good agreement of the curves with the data in Fig. 3.7. These results indicate that the functional form of the mobility must be $\mu(V_g, V_{ds}) = \mu_0(V_g)[1 + \alpha_0 V_{ds}]$, and fits to the data yield typical values of $\alpha_0 \sim 10^{-3}V^{-1}$. The values of μ_0 are shown as a function of the gate voltage in the inset of Fig. 3.7. In Table 3.1 we present the fitting parameters for the second order polynomial fit to the photocurrent voltage characteristics and the extracted values of μ_0 and α_0 for the applied gate voltages.

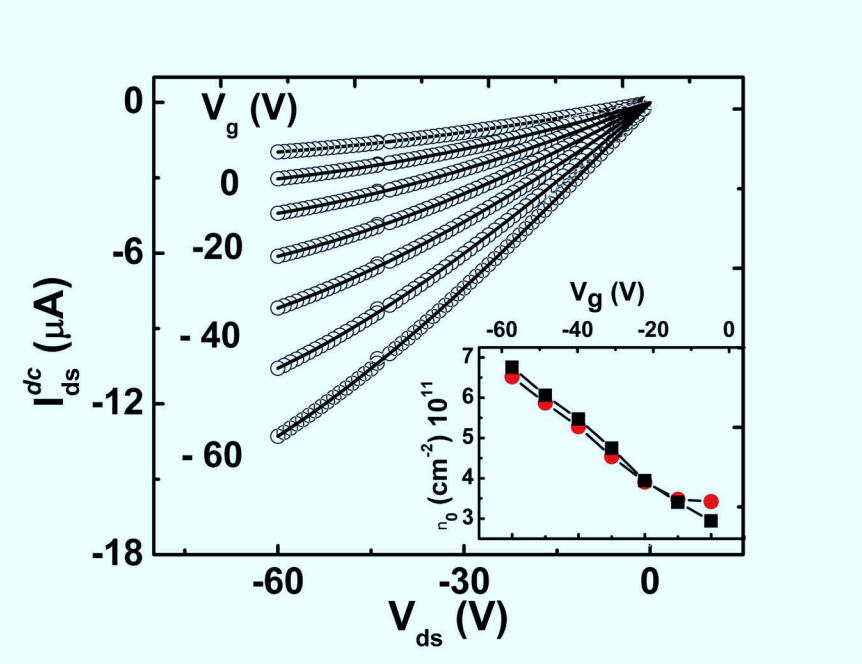

Figure 3.8: Direct current voltage I-V curves for various gate voltages. The lines are third order polynomial fits to the data as described in the text. Inset: gate voltage dependence of the hole density determined using Eq. 3.4 and the field effect mobility extract from photocurrent voltage characteristics.

Using these mobilities, the direct current data can be analyzed by substituting $\mu\left(V_g, V\right)$ into Eq. 3.4, arriving at an integral equation to determine the free carrier density $n\left(V_g, V\right)$ from the measured I_{ds}^{dc}. Excellent fits (correlation coefficient $R^2 = 0.98$) to the data in Fig. 3.8 are obtained using $-I_{ds}^{dc} = AV_{ds} + BV_{ds}^2 + CV_{ds}^3$ from which we derive the field dependence of the free carrier density in the channel as $n\left(V_g, V_{ds}\right) = n_0(V_g)[1 + \beta_0 V_{ds}]$, and with typical value for $\beta_0 \sim 10^{-3}V^{-1}$. The fitting parameters and the extracted values of n_0 and β_0 for every gate voltage are presented in Table 3.2.

Using the above analysis, we obtained μ_0 and n_0, shown in Fig. 3.9, corresponding to the singlet exciton optical transitions in Fig. 3.3. For a given V_g, we find that $n_0(V_g)$ is about a tenth of the total carrier density, N, derived using the gate capacitance (see Fig. 3.9) . The difference is the trapped hole density, which is thus about three orders of magnitude bigger than the photocarrier density, strengthening our initial assumption that the density of photocarriers is field independent. Fitting our $\mu_0 - V_g$ data, we find that μ_0 varies as $V_g^{1/3}$. In comparison, Vissenberg [43] found a $V_g^{2/3}$ dependence using the variable-range hopping model to describe Pn TFTs. The inset in Fig. 3.9 shows the increase of μ_0 with n_0 that is consistent with the trap and release model [41, 46] for organic TFTs.

In the next chapters we shall use the multiple trapping and release model concepts to describe the Pn films: narrow transport bands and high density of defects states in the band gap. Recent experimental work, using Time-resolved Terahertz Pulse Spectroscopy [54] reveals bandlike transport in both Pn crystals and thin films over subpicosecond time scales. The technique allows probing the

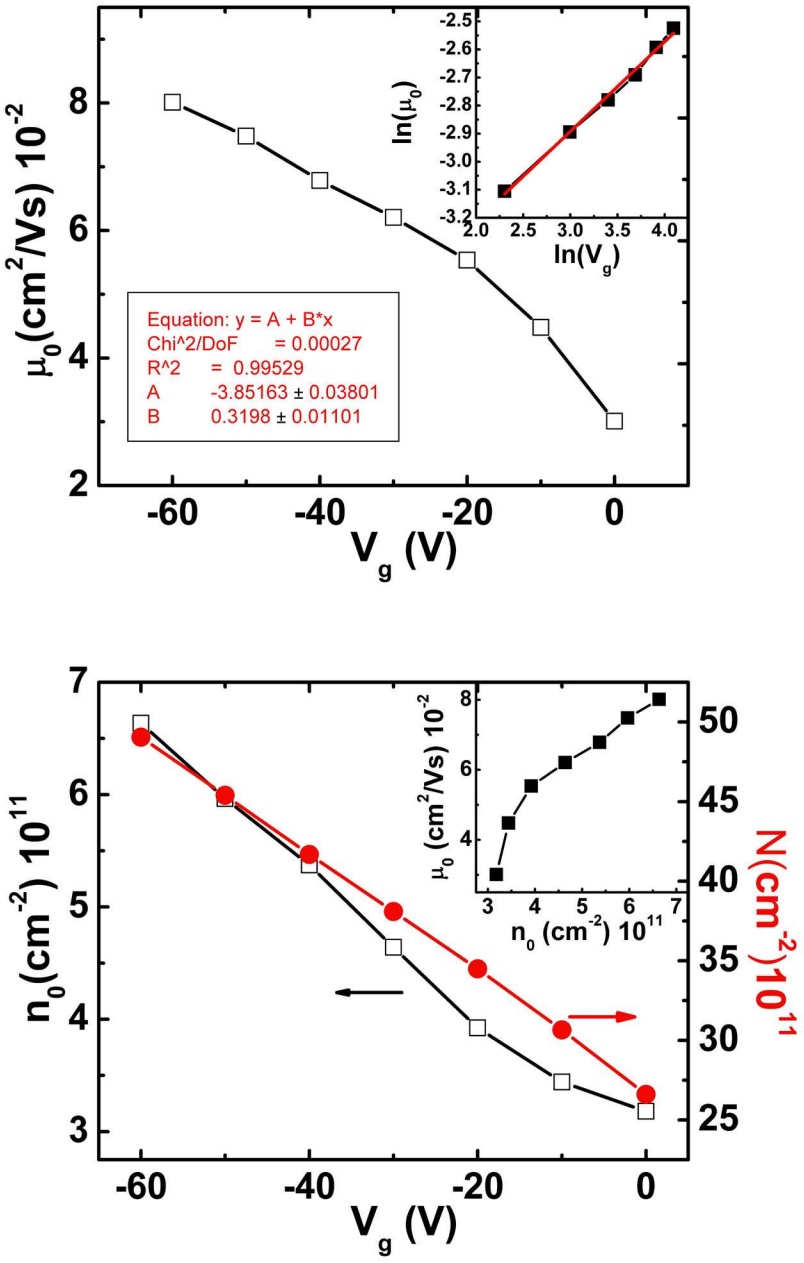

Figure 3.9: Gate voltage dependence of the hole mobility extracted from the photocurrent measurements. Inset: ln-ln plot of μ_0 as a function of V_g. The lower graph presents the free carrier density, n_0 (left axis), determined by fitting the direct IV measurements using the average experimental mobility and the charge density, N (right axis), extracted with the capacitance formula. Inset: the average mobility as a function of free hole density.

dynamics of mobile charge carriers in materials before they are trapped at defect sites. The authors of reference [54] claim that the thermally activated mobility in Pn films is the effective trap-limited mobility, while the mobility over a time scale shorter than typical carrier trapping time increases as the temperature decreases.

3.4 Conclusions

In conclusion, we demonstrate a new technique for determining the field-dependent mobility in organic TFTs using photocurrent modulation spectroscopy. In contrast with previous methods [40, 41, 50, 55], this technique does not rely on assumed models of transport in organic semiconductors [40, 41, 43] and it is not restricted to the linear regime of the TFT operation to obtain the gate dependence of the mobility. It also allows a separation of the total charge in the conductive channel into free and trapped charge carriers. Our results show that approximately a half of the total density represents trapped carriers. Furthermore, we find that $\mu_0 \sim V_g^{1/3}$ and that μ_0 increases with n_0.

Chapter 4

Probing the Defect States in Pentacene Thin-Film Transistors

4.1 Overview

In this chapter we present photocurrent modulation spectroscopy as a probe of defect states in pentacene thin-film transistors. Simultaneous measurement of the magnitude and phase of the photocurrent as a function of the modulation frequency allows us to extract information about the distribution of localized states in Pn TFTs. This is carried out by modeling the photo-carrier generation process as exciton dissociation via interaction with localized traps. Experimental data reveal a Gaussian distribution of localized states centered at 0.3 eV above the highest occupied molecular orbital. The behavior of these localized states in Pn evaporated on different gate dielectric materials is presented.

4.2 The Origin of Defects in Organic Semiconductors

The low-energy electronic states in crystalline organic semiconductors are characterized by an energy gap of the allowed states between highest-occupied molecular orbital (HOMO) and the lowest-unoccupied molecular orbital (LUMO). The density of occupied and unoccupied states at the HOMO and LUMO, respectively, portrays a sharp square-root singularity akin to that of inorganic semiconductors [56]. When

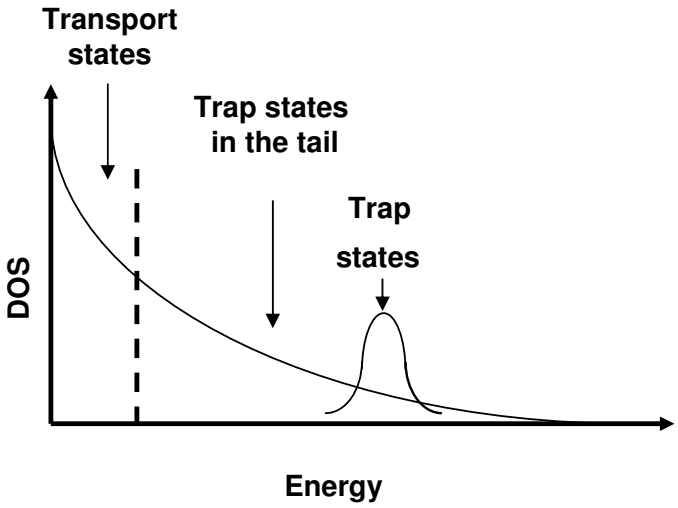

Figure 4.1: Transport and localized states in organic semiconductors.

disorder is present, the low-lying electronic states are described using the mobility edge picture developed for amorphous semiconductors [57]. A high degree of disorder can give rise to tails of localized electronic states at the extremity of the energy bands. In organic molecular semiconductors, the main source of disorder is the random variation of the HOMO-LUMO levels from molecule to molecule, their positions being perturbed by polarization effects induced by surrounding neighboring molecules. This quasi-continuous tail distribution is usually described by an exponential density-of-states [21, 58]. In addition to disorder effects, certain structural defects can also give rise to discrete states in the band gap. In Fig. 4.1 we present a qualitative description of the quasi-continuous tail and discrete localized states in organic semiconductors.

Discrete states can also arise from chemical impurities if the HOMO or LUMO

of an incorporated molecule is situated in the band gap of the host lattice. On the other hand, independent of the positions of the guest molecule's energy levels, if the guest molecule is polar it changes the polarization energy locally resulting in the appearance of local states in its vicinity. If the shape of the impurity molecule is different from that of the host, then one should expect an additional local modification of the polarization energy. The last effect is equivalent to the appearance of a structural trap.

Besides structural and chemical traps, excess carriers can be self trapped due to the interaction with local vibrations. This interaction will induce a distortion of the lattice around the carrier, creating a quasiparticle, the polaron, associated with carrier motion renormalized by the lattice distortion. If the polaron band is narrow, such that the excess carrier residence time is large compared with atomic vibrations, the polaron is considered to be self-trapped.

4.3 Photocurrent Modulation Spectroscopy: Trap Detection Technique for Pn TFT

In the photocurrent technique, intensity modulated radiation is used to produce excess free carriers in the material. Conventionally, the energy of the excitation light is greater than the band gap of the semiconductor such that the electrons undergo band to band transitions [59]. The resulting photocarriers undergo trapping and release processes due to the interaction with localized states, resulting in a phase shift between the excitation and the photocurrent. Therefore, an analysis of

the photocurrent phase in the frequency domain can be a powerful tool to characterize disordered semiconductors [60, 61].

Our goal is to apply the principles of this technique to study Pn thin films. Optical transitions in organic semiconductors imply the creation of excitons. It is generally believed that the triplet excitons in Pn interact with trapped carriers producing excess free holes [9, 49, 62]. Levinson's [63] studies in anthracene crystals determined a correspondence between triplet exciton absorption and photogeneration of carriers, supporting the idea that excess photocarriers are generated by the interaction of the triplet exciton and trapped carriers. The process can be described by the equation:

$$T_1 + h_t \longrightarrow S_0 + h,$$

where T_1 is the triplet exciton, h_t represents a trapped hole, S_0 is the number of molecules in ground state and h is the resulting free carrier. The rate constant reported for the triplet exciton detrapping in anthracene is about 3.2×10^{-11} $\mathrm{cm^3 s^{-1}}$. Studies of the photoconductivity of the anthracene crystals in a magnetic field also concluded that the carrier generation in the bulk is due to detrapping by triplet excitons [64], suggesting that this is a viable mechanism in polyacenes.

Direct optical excitation of triplet excitons is forbidden by selection rules. However, these excitons can be produced by intersystem crossing, or by fission of singlet excitons. Pentacene polycrystalline thin films have been investigated by pump-probe spectroscopy and photons with 2 eV energy were used to create singlet excitons, S_1 [22]. The experimental observation was a very fast creation of triplet

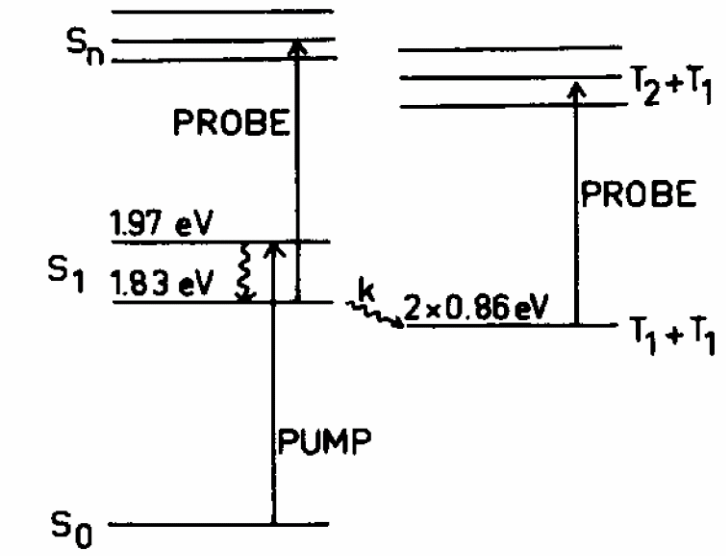

Figure 4.2: The energy level scheme of the pentacene thin film. The singlet exciton, S_1, is represented by the Davydov doublet. $T_1 + T_1$ represents two triplet excitons with no significant binding energy at room temperature. The diagram is from Ref. [22].

excitons. It was found that the singlet excitons in the upper level of the Davydov split state relax to the lower excited state with time constant less than 20 fs. The creation of the triplet excitons is attributed to a fission process from the lower energy singlet exciton to a pair of triplet excitons, T_1. The process, with a rate constant of 1.3×10^{13} s^{-1}, is illustrated in Fig. 4.2. Based on these observations we can understand photocarrier generation through initial excitation into the singlet state in Pn as exciton dissociation via interaction with localized traps.

4.4 Experimental Results and Discussion

The samples employed in this experiment are top-electrode Pn TFTs (see Chapter 2 for device geometry), fabricated on different dielectric materials: SiO_2, polyvinylpyrrolidone (PVP) and polymethyl methacrylate (PMMA). The polymeric dielectric materials were spincoated on 3000 Å SiO_2 at 4000 rot/min for 1 min and further baked out at 180°C for 5 min. The resulting polymer thickness was 2000 Å. Sets of 2 Pn TFTs were fabricated simultaneously on SiO_2 and one of the polymer substrates.

We generated photocurrent in these devices by selecting a narrow excitation band around 667 nm, the wavelength corresponding to singlet exciton absorption. The radiation was focused on the transistor channel using a high numerical aperture microscope objective to eliminate contact effects. The photocurrent magnitude and phase as a function of the modulation frequency were measured using the lock-in technique presented in Chapter 2.

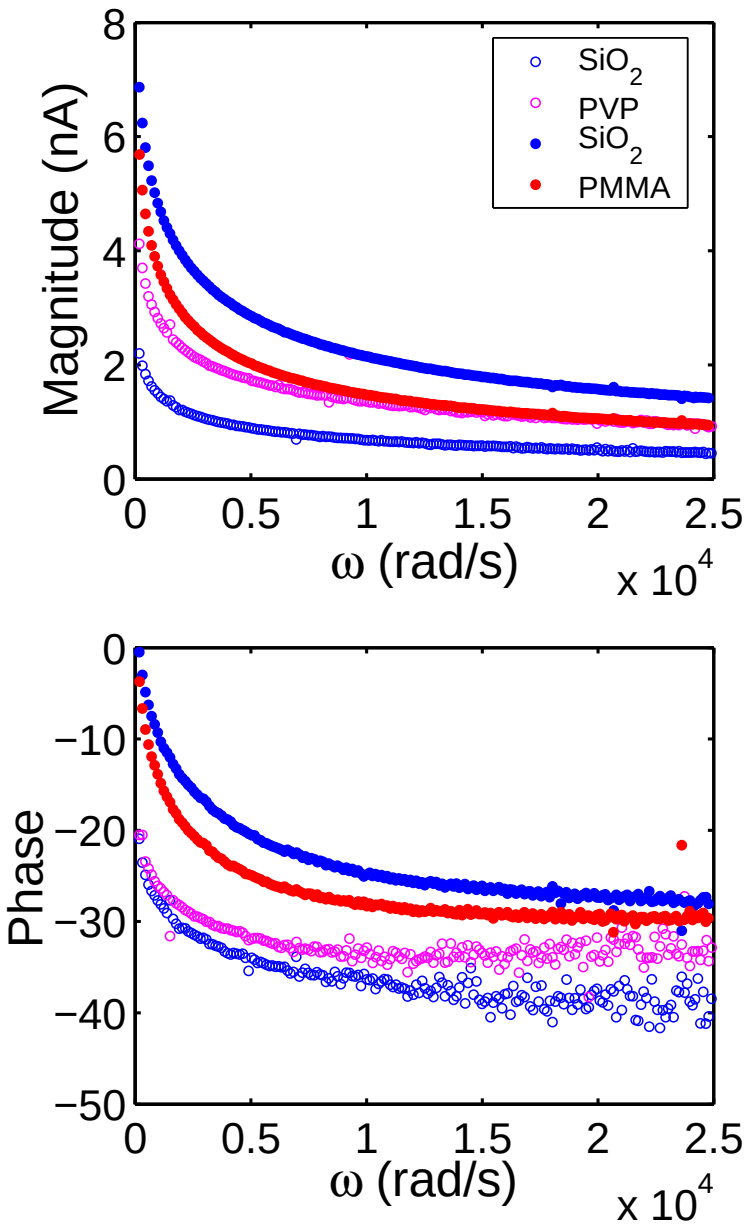

Figure 4.3: Photocurrent magnitude and phase as a function of the modulation frequency. Two sets of data for Pn simultaneously deposited on SiO_2 and PVP (open circles) and SiO_2 and PMMA (full circles) are presented. The deposition conditions are different, as mentioned in text.

Representative data of the photocurrent magnitude and phase measurements carried out on SiO_2 and PVP or SiO_2 and PMMA devices are presented in Fig. 4.3. The deposition rate was < 0.1 Å/s in both cases, but the Pn was degassed for 4 hours at 120°C prior to deposition for the SiO_2/PMMA pair versus 1 hour for SiO_2/PVP set. It is particularly interesting to note that devices with Pn active layer grown simultaneously manifest qualitatively similar phase behavior, as can be seen in Fig. 4.3. These data suggest that the measured phase of the photocurrent is dependent on the thin-film deposition conditions as well as the gate-dielectric used in the fabrication of the Pn TFTs. To quantify these effects, we extract the trap density of states from these data by modeling the photocarrier generation process as exciton dissociation via interaction with trapped carriers.

4.4.1 A Model of the Photocarrier Generation Process in Pn TFTs

Figure 4.4 summarizes the mechanism for the photocarrier generation process in Pn TFTs. The organic electronic states in the semiconductor are characterized by the density of occupied states up to the HOMO, the density of unoccupied states starting from the LUMO and a quasi-continuous distribution of localized states within the band gap, up to an energy E_d. The first step in this process is the absorption of the incident radiation, leading to the creation of singlet excitons via the HOMO-S1 transitions. The singlet excitons then decay as pairs of triplet excitons [22]. Photocurrent is generated by charge separation associated with the triplet exciton-trapped hole interaction. We describe this multi-step process, illustrated in

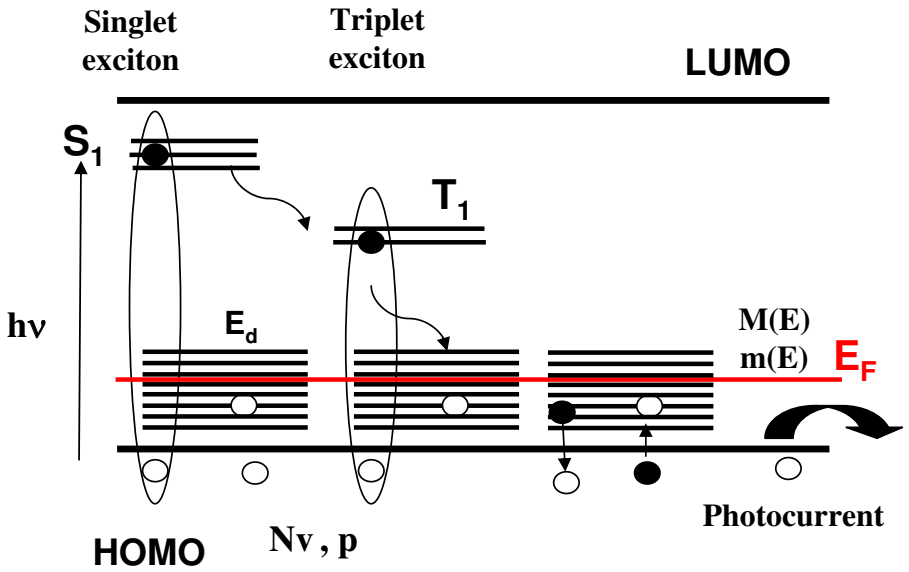

Figure 4.4: Diagram describing the photocurrent generation multi-step process: 1) absorbtion of a photon and creation of a singlet exciton, 2) singlet-triplet exciton dissociation, 3) triplet exciton-trapped hole interaction.

Fig. 4.4, in order to extract an expression for the photocurrent as function of the modulation frequency.

The dynamics of the singlet exciton (S) generation in the Pn is described by Eq. 4.1,

$$\frac{dS}{dt} = \Sigma N_v I_0 e^{i\omega t} - KS. \tag{4.1}$$

The number of excited electrons from the HOMO to the singlet exciton states S_1 is determined by the absorption cross-section corresponding to the incident radiation, Σ, the number of states in the transport band, designated N_v, and the intensity of the incident radiation characterized by the magnitude I_0 and modulation frequency

ω. The singlet exciton loss mechanism is the fission process, $S_1 \longrightarrow 2T_1$, with a fission rate, K, experimentally determined to be $1.3 \times 10^{13} s^{-1}$ [22].

The free carriers are created by the interaction of the triplet excitons T with trapped holes:

$$\frac{dT}{dt} = 2KS - \gamma TH. \tag{4.2}$$

H represents the density of trapped holes and γ is the rate constant for the triplet exciton detrapping. The factor of two represents the requirement that the triplet excitons are always created in pairs from the singlet exciton states [22]. For anthracene the rate constant γ is reported to be $3.2 \times 10^{-11} \mathrm{cm}^3 \mathrm{s}^{-1}$ [62]. Considering the similarities between the pentacene and anthracene crystalline structures, we expect this rate constant for Pn to be almost the same order of magnitude. Equation 4.2 gives us the number of triplet excitons, while the number of photocarriers is determined by the dynamics of the population of these trap states in the presence of light, using Eq. 4.3:

$$\frac{dp}{dt} = -\int_0^{E_d} \frac{dm(E)}{dt} dE. \tag{4.3}$$

The population of the trapped holes is represented by $m(E)$ while $M(E)$ describes the distribution of states into the band gap up to an energy E_d above the HOMO. The total density of trapped holes is determined by: $H = \int_0^{E_d} m(E) dE$.

The rate equation for trapped holes also involves terms corresponding to interaction between these trap states and the HOMO:

$$\frac{dm(E)}{dt} = p[M(E) - m(E)]v\sigma_p - m(E)N_v v\sigma_p e^{-E/kT} - \gamma T m(E). \qquad (4.4)$$

The first term in Eq. 4.4 represents the trapping process, where p is the density of holes or available states in the transport band, v is the thermal velocity and σ_p is the hole capture cross section. The last two terms correspond to thermal detrapping and triplet exciton detrapping. We understand the triplet exciton interaction with the trapped hole as a transition of the excited electron to one of the available localized states into the band gap (the electron is detrapping a hole). In this process, the electron-hole pair forming the triplet exciton dissociates and the hole becomes free to participate in the conduction.

Given the periodic modulation imposed on the incident radiation at frequency ω, we expect the same behavior for the solution of these equations. A Fourier analysis allows us to extract an expression for the density of photo-carriers. The general form of the solution of Eq. 4.1 is $S = S_0 e^{i\omega t}$, where

$$S_0 = \frac{\Sigma N_v I_0 e^{-i\phi}}{[K^2 + \omega^2]^{1/2}}; \quad \tan(\phi) = \frac{\omega}{K}.$$

Using S_0 we can solve Eq. 4.2, assuming the form $T = T_0 e^{i\omega t}$ and ignoring the second harmonic contributions:

$$T_0 = \frac{2KS_0 e^{-i\eta}}{[(\gamma H_0)^2 + \omega^2]^{1/2}}; \quad \tan(\eta) = \frac{\omega}{\gamma H_0}; \quad H_0 = \int_0^{E_d} m_0(E)dE;$$

where $m(E) = m_0(E) + m_1(E)e^{i\omega t}$ is the density of trapped holes at a localized state characterized by energy E.

Assuming a solution for $p = p_0 + p_1 e^{i\omega t}$ with $p_0 = N_v \; e^{\frac{-E_F}{kT}}$, we solve the rate equation for the trapped holes (Eq. 4.4). From the time independent part of the equation, we extract an expression for $m_0(E) = \frac{M(E)}{\xi+1}$, where $M(E)$ represents the distribution of localized states in the Pn band gap and $\xi = e^{\frac{E_F - E}{kT}}$. The time dependent part allows us to extract $m_1(E)$, which is directly related to the density of photocarriers generated in the Pn transistor, p_1, through Eq. 4.3. The final expression for the photocurrent is:

$$p_1 = \frac{\int_0^{E_d} \frac{\gamma T_0 M(E)}{(\xi+1)\{v\sigma_p p_0(\xi+1)+i\omega\}} dE}{1 + \int_0^{E_d} \frac{v\sigma_p \xi M(E)}{(\xi+1)\{v\sigma_p p_0(\xi+1)+i\omega\}} dE}. \tag{4.5}$$

Thus, our analysis shows that the photocurrent is determined by the distribution of the localized states, $M(E)$, the modulation frequency, ω, and parameters characterizing the Pn sample, like the quasi-Fermi position with respect to the HOMO, E_F, thermal velocity, v, and the capture cross section for holes, σ_p. The expression in Eq. 4.5 tells us that the experimental photocurrent magnitude and phase as a function of the modulation frequency should allow us to extract information about the distribution of the localized states.

To gain an intuitive understanding of each term in Eq. 4.5, we evaluate numerically the behavior of the terms involved in the expression of the photocurrent. We define ω in terms of a corresponding energy E_ω such that $\omega = v\sigma_p p_0 e^{\frac{E_F - E_\omega}{kT}}$, and we define $\Omega = e^{\frac{E_F - E_\omega}{kT}}$. E_ω represents the energy of the states where the thermal detrapping rate of a hole becomes equal with the modulation frequency, ω. With these notations p_1 becomes:

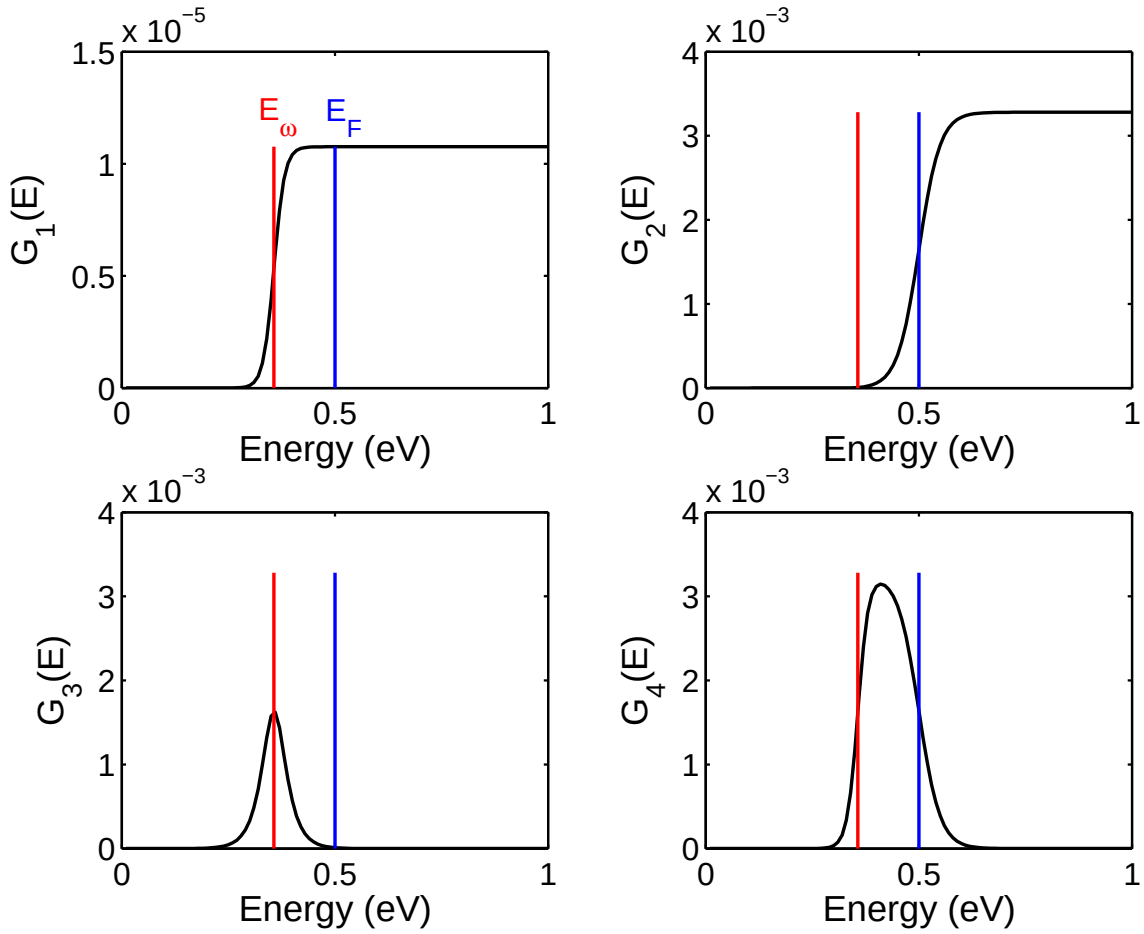

Figure 4.5: The behavior of the G functions for 1000 Hz modulation frequency. The red line represents the position of E_ω while the blue one marks the position of E_F above the HOMO.

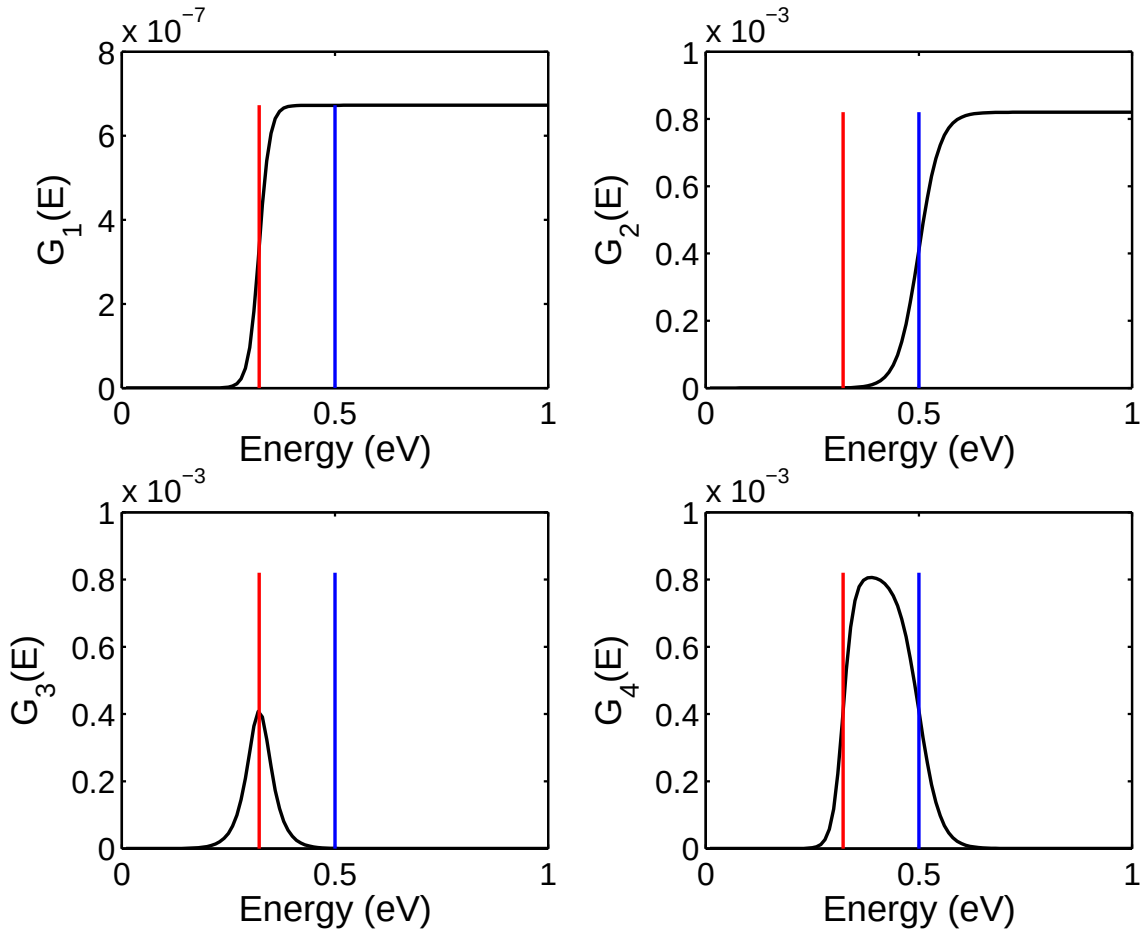

Figure 4.6: The behavior of the G functions for 4000 Hz modulation frequency. The red line represents the position of E_ω while the blue one marks the position of E_F above the HOMO.

$$p_1 = \frac{\int_0^{E_d} \frac{T_0 \gamma M}{p_0 v \sigma_p}(G_1 - iG_2)dE}{1 + \int_0^{E_d} \frac{M}{p_0}(G_3 - iG_4)dE}.$$

In Fig. 4.5 and 4.6 we plot the G functions defined as:

$$G_1 = \frac{1}{(\xi+1)^2 + \Omega^2}; \quad G_2 = \frac{\Omega/(\xi+1)}{(\xi+1)^2 + \Omega^2};$$

$$G_3 = \frac{\xi}{(\xi+1)^2 + \Omega^2}; \quad G_4 = \frac{\xi\Omega/(\xi+1)}{(\xi+1)^2 + \Omega^2};$$

for two different modulation frequencies, 1000 and 4000 Hz. The parameters used for these numerical calculations are: $kT = 25$ meV, $N_v = 10^{21}$ cm^{-3} (the upper limit which corresponds to the density of molecules in the Pn crystal), $v = 10$ cm/s, $\sigma = 10^{-12}$ cm^2 [62], and $E_F = 0.5$ eV. The G functions behave almost like step functions around E_ω or E_F and their values are negligible for energies smaller than E_ω. The result of the simulation tells us that the photocurrent technique applied for this particular system allows us to extract the distribution of localized states in the Pn band gap with energies higher than E_ω relative to the HOMO.

In Fig. 4.7 we present E_ω as function of the modulation frequency. With increasing ω, E_ω moves closer to the HOMO in a logarithmic fashion, $E_\omega \sim \log(1/\omega)$, approaching a lower limit E_{LL} for probing the density of states. This low energy limit, determined by the maximum experimental modulation frequency, $\omega = 2\pi\times$ 4000 Hz, and the two sample parameters, E_F and N, suggests that the technique is appropriate for probing deep states in the Pn gap.

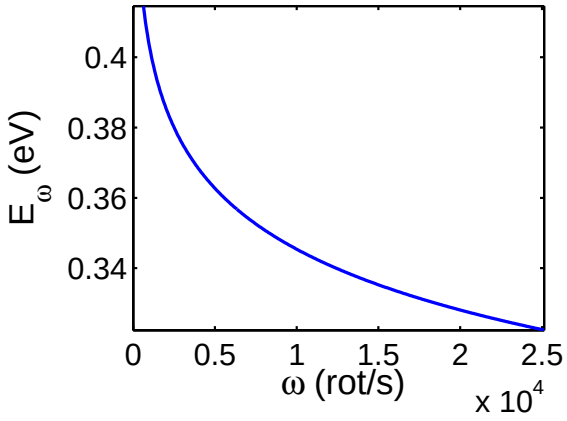

Figure 4.7: The lower limit of gap states energy distribution (with respect to the HOMO) that we can probe with photocurrent technique as a function of the modulation frequency. Simulation parameters: $kT = 25$ meV, $N_v = 10^{21}$ cm^{-3}, $v = 10$ cm/s, $\sigma_p = 10^{-12}$cm^2 [62], and $E_F = 0.5$ eV.

4.4.2 Defect Density-of-States in Pn TFTs

To model the experimental data using our expression for the photocurrent (Eq. 4.5), we have to assume a distribution for the localized states that characterizes the defect states in the Pn thin film. The expression for the photocurrent, up to a constant, is determined by two material parameters describing the Pn film, E_F and $N = N_v v \sigma_p$, and parameters characterizing the defect distribution. A MatLab code was written to numerically solve the complex expression in Eq. 4.5. The fitting parameters are varied while the G functions are computed. For every set of parameters the numerical integration is carried out assuming an integration limit E_d of 2 eV to completely cover the band gap of the Pn. The goodness of fit is determined by minimizing the χ^2 of the difference between the simulated and experimental data.

Assuming that a simple exponential describes the distribution of the localized

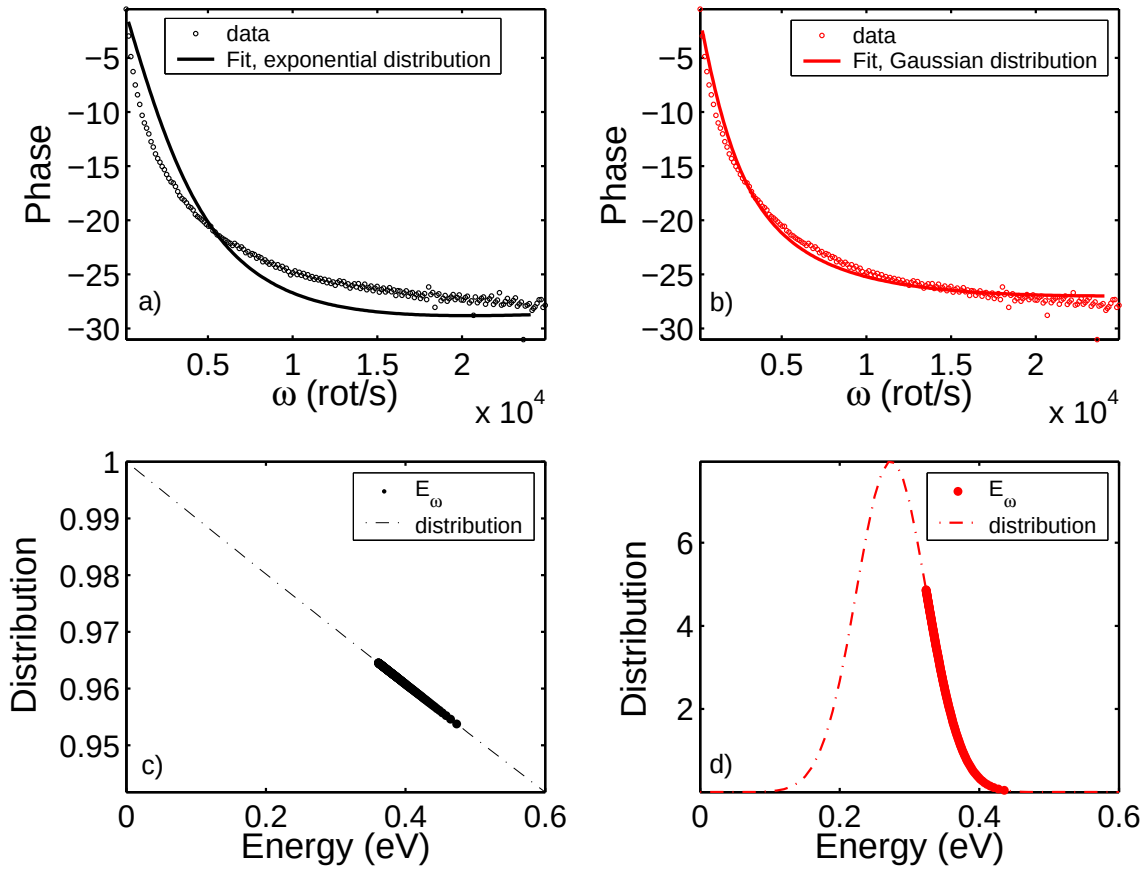

Figure 4.8: Fit to the data assuming two distributions for the defect states: exponential and gaussian. Sample fitting parameters: E_F, $N = N_v v \sigma_p$; distribution fitting parameters a) exponential distribution, $M(E) = M_0 \exp(-\beta E)$: the width of the distribution, β, b) gaussian distribution, $M(E) = M_0/((2\pi)^{1/2}\sigma) \times \exp(-(E - E_0)^2/2\sigma^2)$: the width of the distribution, σ, and the position with respect to the HOMO, E_0.

states, we fit the data and find qualitative agreement between the experiment and the prediction, as can be seen in Fig. 4.8 a). The best fit of the data is obtained for $E_F = 0.40$ eV, $N = 2.8\times10^{10}$ s^{-1} and $\beta = 0.1$ eV^{-1}. In this case, the best fit also gives an E_{LL} of 0.361 eV. However, the fit is not quite satisfactory. Therefore, we conclude that a simple exponential distribution does not describe the localized density of states in the Pn band gap probed under our experimental conditions.

Instead of exponential tail states arising from disorder, we now consider a gaussian distribution describing deep localized states in these Pn films. In Fig. 4.8 b) we present the best fit to the data, obtained with the assumed gaussian distribution. The fitting parameters are: $E_F = 0.389$ eV, $N = 6.6\times10^{9}$ s^{-1}, the position of the gaussian with respect to the HOMO is $E_0 = 0.274$ eV, the width of the gaussian is $\sigma = 0.05$ eV^{-1} and $E_{LL} = 0.325$ eV. Notice that the sample parameters extracted from the best fit of the data for the two assumed distributions are similar. However, the quality of the fit is significantly better for the gaussian distribution. We note that for our modulation frequency range we scan only a third of the presumed gaussian distribution, as can be seen in Fig. 4.8 d). The reason for this is that the technique is limited by the lower limit of the energy domain, E_{LL}.

Because E_{LL} is inversely proportional to the modulation frequency, ω, simplistically one would increase the modulation frequency in order to decrease E_{LL}. However, since the model is valid for quasi-equilibrium conditions, an upper limit of the modulation frequency is necessary to assure a thermodynamic equilibrium between the free carriers and the ones trapped in states close to the quasi-Fermi level. The upper limit of the modulation frequency is determined by $\omega^* = 2\pi \times N_v v \sigma_p e^{\frac{-E_F}{kT}}$

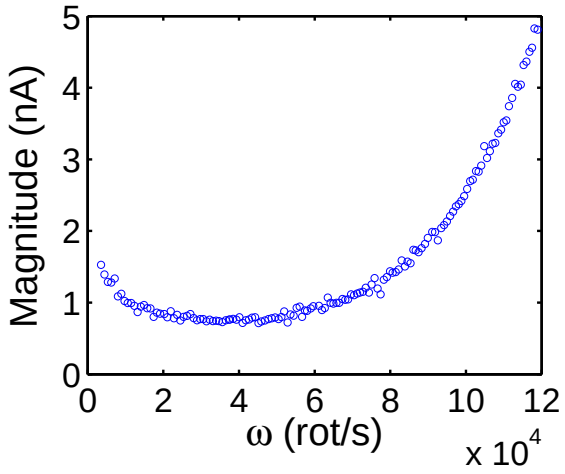

Figure 4.9: The magnitude of the photocurrent as a function of the modulation frequency. The data suggest that for higher frequencies the quasi-stable condition is no longer satisfied. We limit our analysis to $\omega = 2.5 \times 10^4$ kHz and below.

[68], which is expected to be order of kHz. With the parameters extracted from our fit to the data, E_F = 0.38 eV and $N = 6.6{\times}10^9$ s^{-1}, ω^* becomes 1.7 $\times 10^4$ kHz. Experimentally we find that when the modulation frequency is increased, the magnitude of the photocurrent passes through a minimum, then rapidly increases, as can be seen in Fig. 4.9. As a consequence we limit the analysis of the data to $\omega = 2.5 \times 10^4$ kHz and below.

To acquire more confidence for our assumed gaussian distribution of localized states, we also analyzed photocurrent magnitude and phase spectra collected from a Pn TFT on SiO_2 at different temperatures. In Fig. 4.10 we present experimental data collected with the applied bias V_{ds} = -15 V and V_g = 0 V. As we decrease the temperature from 300 to 220 K, the photocurrent magnitude decreases while the phase is shifted towards more negative values. We simultaneously fit the magnitude

and the phase versus ω, measured at 300 K with E_F, N, E_0 and σ as fitting parameters. From the minimum χ^2 we extract the parameters of the gaussian distribution which describe the data. The best fit to the data is obtained assuming a gaussian distribution centered at 0.292 eV.

For the rest of the data, measured at different temperatures, we fix the Gaussian parameters while we perform the fit. As we can see in Fig. 4.10, both the magnitude and the phase are well described by our model (Eq. 4.5). The fitting parameters are presented in Table 4.1. The magnitude is fitted up to a constant, A, which is temperature dependent and increases almost linearly with the carriers' field effect mobility, as can be seen in Table 4.1. This behavior is expected since the model predicts the density of photocarriers while the experimental data represents photocurrent, being determined by the product between the photocarrier density and mobility. The measured phase of the photocurrent is also well described by our model. From the fitting parameters we can extract the Fermi energy position as a function of temperature. The data, presented in Fig. 4.10, shows an almost linear increase of E_F versus T. Assuming some of the defects in the Pn film acting as acceptors, the position of the Fermi level should follow $E_F = \mathrm{kT}\ \ln(N_v/N_a)$, where N_v and N_a are densities of states in the transport band and acceptor states. Our results gives us reasonable confidence that the gaussian distribution describes the localized states.

Now we present the experimental photocurrent data measured on a different Pn TFT for various gate voltages, as shown in Fig. 4.11. The best fit to the data is obtained for a gaussian distribution of defects centered at 0.304 eV. Using the

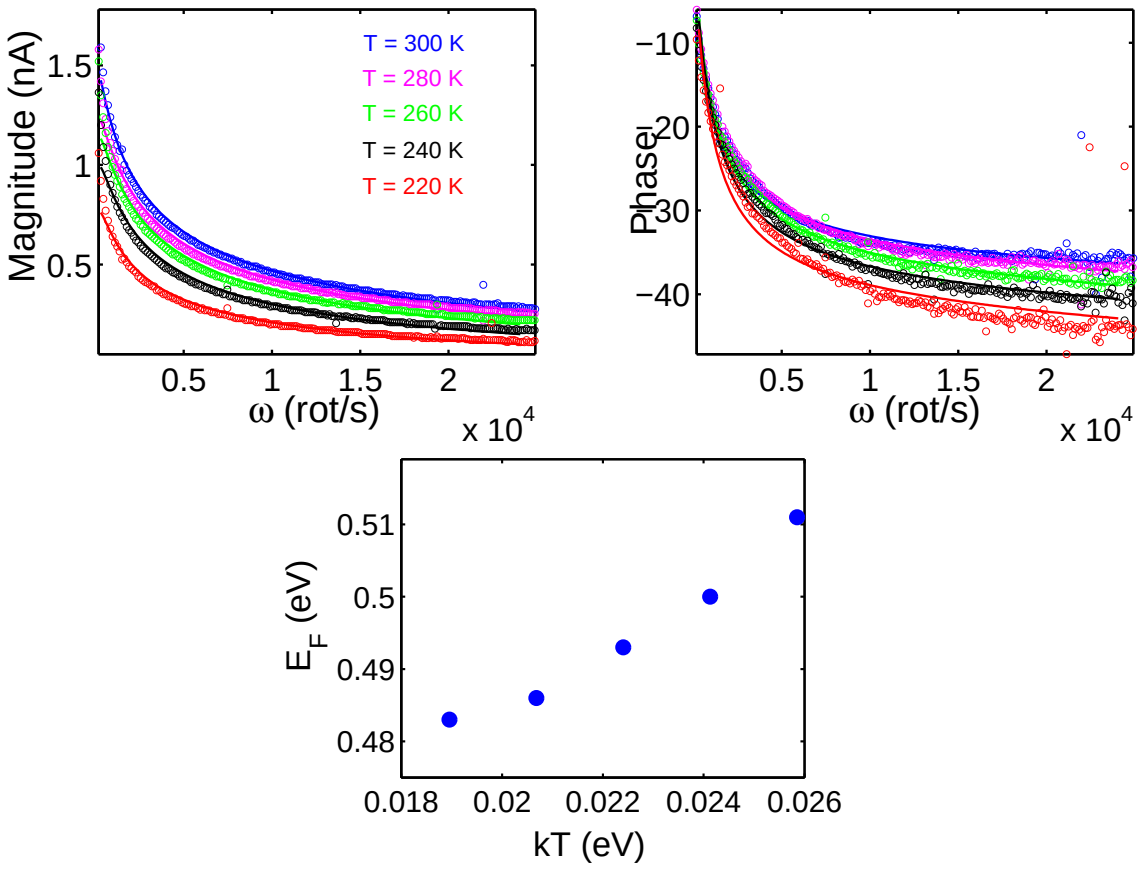

Figure 4.10: The magnitude and the phase of the photocurrent as a function of the modulation frequency measured at different temperatures (opened circles). The best fit of the magnitude and the phase (full lines) is based on a model of defect states described by a gaussian distribution centered at 0.292 eV above the HOMO. The Fermi energy, E_F, as a function of temperature, is extracted from the fitting parameters.

T(K)	$E_F(V)$	$N(s^{-1}) \times 10^{10}$	A	$\mu(cm^2/Vs)$
300	0.511	9.12	0.030	0.123
280	0.500	40.9	0.020	0.104
260	0.493	177	0.014	0.0799
240	0.486	910	0.008	0.0571
220	0.483	6500	0.0043	0.037

Table 4.1: The fitting parameters of the magnitude and phase of the photocurrent as a function of the modulation frequency and the extracted filed effect mobility from I-V curves, for different temperatures. The extracted gaussian distribution is located at E_0=0.292 eV above the HOMO with characteristic width σ=0.05$(eV)^{-1}$. The applied voltages were V_{ds} = 0 V and V_g = -15 V.

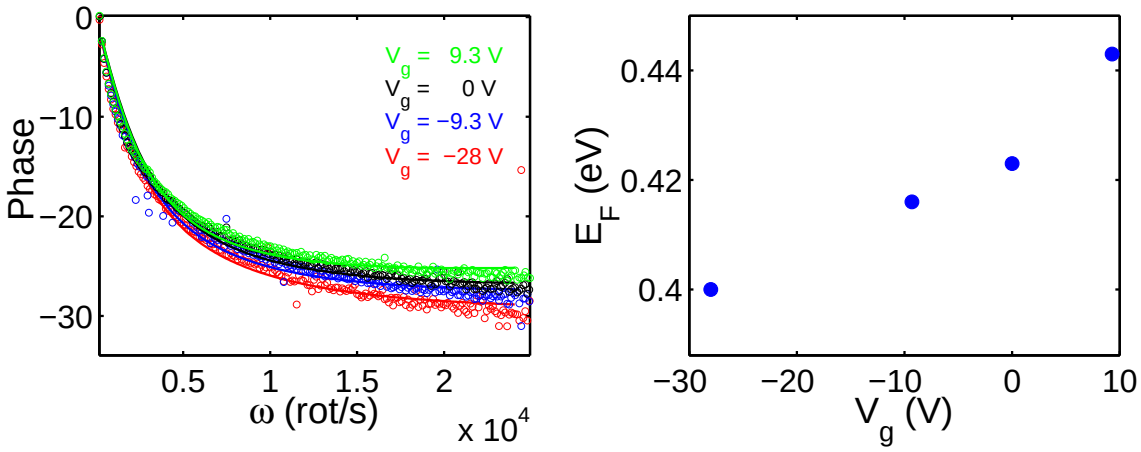

Figure 4.11: The the phase of the photocurrent as a function of the modulation frequency measured at different gate voltages (opened circles). The best fit of the data (full lines) reveal defect states described by a gaussian distribution centered at 0.304 eV above HOMO. The Fermi energy, E_F, as a function of applied gate voltage is extracted from fitting parameters.

$V_g(V)$	$E_F(V)$	$N(s^{-1}) \times 10^{10}$	A
0	0.423	2.6	0.074
- 9.3	0.416	2.2	0.106
- 28	0.40	1.2	0.185
+ 9.3	0.443	5.0	0.042

Table 4.2: The fitting parameters of the magnitude and phase of the photocurrent as a function of the modulation frequency for different gate voltages. The extracted gaussian distribution is located at E_0=0.304 eV above the HOMO with characteristic width σ=0.05$(eV)^{-1}$.

same fitting procedure as described above, we obtain the Fermi energy position as a function of gate voltage. As can be seen in Fig. 4.11, E_F moves closer to the HOMO with negative gate bias, as expected, suggesting that our approach of interpreting the experimental data is reasonable.

The analysis of the photocurrent phase measurements suggests the existence of a localized distribution of defect states with an energy of about 0.3 eV above the HOMO. This result is in good agreement with other reports in the literature using different experimental techniques [65, 66, 67]. Further, we want to address the influence of the Pn morphology and the effects of dielectric material on these defect states. We analyze the data collected from the two sets of Pn transistors simultaneously fabricated one the control substrate (SiO_2) and the second substrate either PVP or PMMA. The dielectric materials chosen for these experiments are polymeric materials of current interest, since the technological trend is to fabricate Pn

transistors on flexible substrates. We also mention small variations in the dielectric constants associated with these materials, as presented in Table 4.3.

4.4.3 Morphological and dielectric effects on the localized states in Pn TFTs

Structural differences in Pn films fabricated on different dielectric materials are expected to influence the transport properties in these films. In Fig. 4.12 we present current-voltage characteristics for the two sets of Pn transistors. For instance, in Fig. 4.12 a) and c) we have output and transfer curves for the control sample grown on a SiO_2 versus the sample grown on a PVP substrate. The extracted mobilities and threshold voltages are 0.04 cm^2/Vs and -15.5 V for SiO_2 and 0.2 cm^2/Vs and +9.5 V for PVP substrate. In Fig. 4.12 b) and d) we have the corresponding characteristics for SiO_2 and PMMA. In this case, the extracted mobilities and threshold voltages are 0.10 cm^2/Vs and +21 V for SiO_2 and 0.03 cm^2/Vs and -11.8 V for PMMA. In both cases we note important differences in the carrier mobilities and threshold voltages attributed to structural differences in the Pn films evaporated on different dielectric materials. On the other hand, different deposition conditions are reflected in the Pn/SiO_2 device parameters, as compared between the control samples in the two sets. The most noticeable difference is in the threshold voltage, V_T, which is negative in one case and positive in the other.

For further characterization of the differences in the Pn films, we measured the photocurrent spectra in these devices. In Fig. 4.13, notice the striking differences

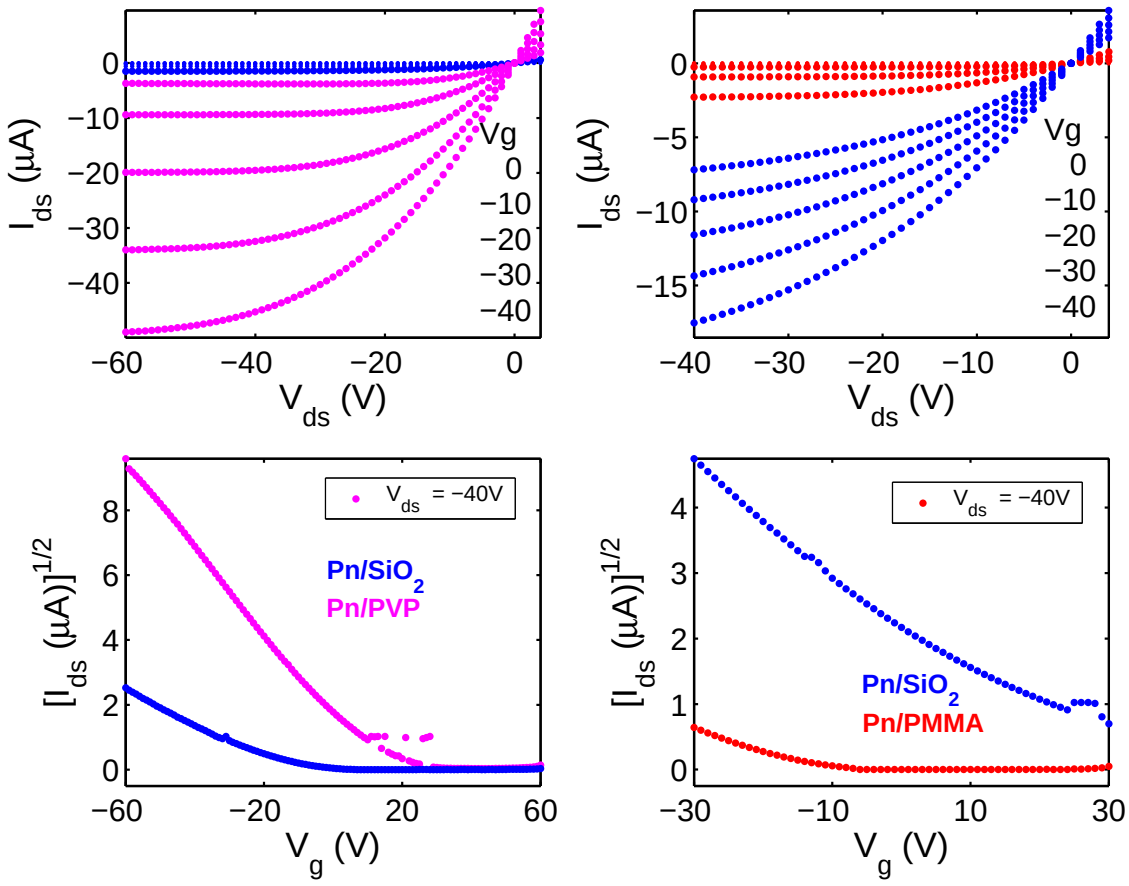

Figure 4.12: Current-voltage characteristics for pairs of Pn transistors fabricated simultaneously on SiO_2 and PVP or SiO_2 and PMMA. The extracted mobilities and threshold voltages are presented in Table 4.3.

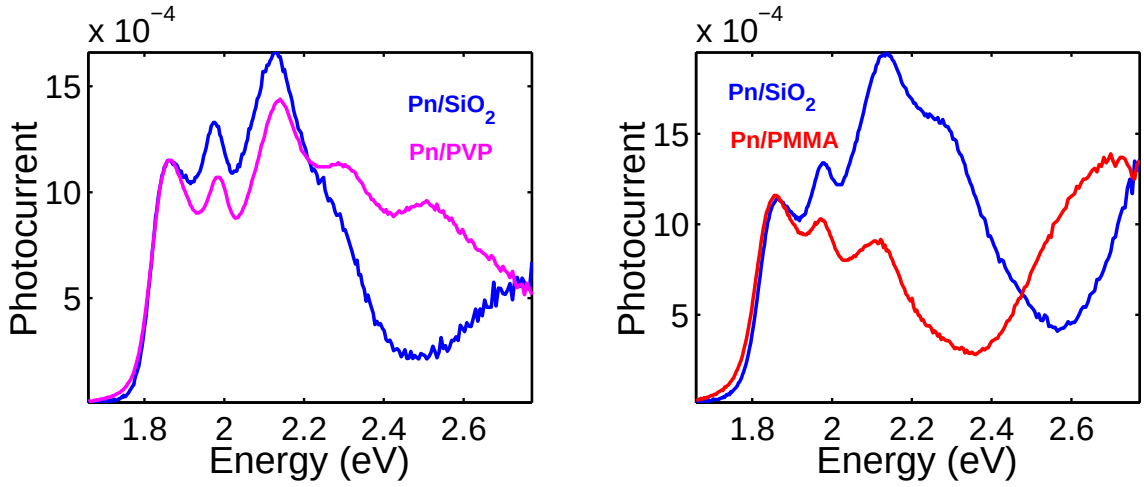

Figure 4.13: Normalized photocurrent spectra for Pn transistors fabricated on different dielectric materials.

among these spectra. The most obvious difference is in the relative intensities of the peaks in the 2.1 - 2.6 eV energy domain. However, this part of the spectrum can arise from a convolution of two classes of optical transitions.

First, we have direct charge transfer transitions between the molecules in the a-b plane of the unit cell, located at (0, 0, 0) and its nearest-neighbor molecules located at (1/2, 1/2, 0), (0, 1, 0) and (1, 0, 0). These transitions have been experimentally observed at 2.12, 2.27 and 2.345 eV [23]. For the Pn crystal structure refer to Chapter 1. The probability of these transitions is determined by the intermolecular overlap. The larger the electron-hole distance in the CT exciton (and a higher energy in the spectrum), the smaller the transition probability. However, a large CT exciton has a smaller binding energy and needs a lower energy to dissociate and produce photocurrent.

Second, photons with energy in this domain also produce high energy Frenkel excitons. For Pn, several satellites are reported at 2.02, 2.195 and 2.37 eV [23]. These Frenkel excitons can be further subjected to ionization [70] and the ejected electron is subsequently capture by a neighboring molecule creating a secondary charge transfer exciton. The efficiency of this transition may also be determined by the intermolecular overlap.

In our data presented in Fig. 4.13 we clearly observe a peak around 2.1 eV in all of these spectra and a peak around 2.3 eV, which have a different relative strength, I_{CT}, from one sample to another with respect to the 2.1 eV peak. I_{CT} is defined as ratio of absolute intensities. Comparing the relative intensity, I_{CT}, for these samples with the field effect mobilities extracted from I-V curves, we observe that I_{CT} increases with the mobility (as presented in Table 4.3). A possible explanation for this correlation is that the mobility is strongly influenced by the film morphology, which is reflected in the spectroscopic signature. Assuming that the main contribution to the spectrum is coming from direct CT transitions, the intensity of these peaks should provide the spectroscopic probe of local Pn structures formed at the interface with the gate-dielectric. This is because the optical selection rule between these electronic states involves a coupling of their corresponding dipole moment with the electric field component of the incident radiation. This coupling, which determines the strength of the optical transition, is maximum when the electronic transition dipole is parallel to the electric field. In our photocurrent experiment, the incident radiation is polarized parallel to the Pn/gate-dielectric interface. The dipole moment of the charge-transfer transition lies along the direc-

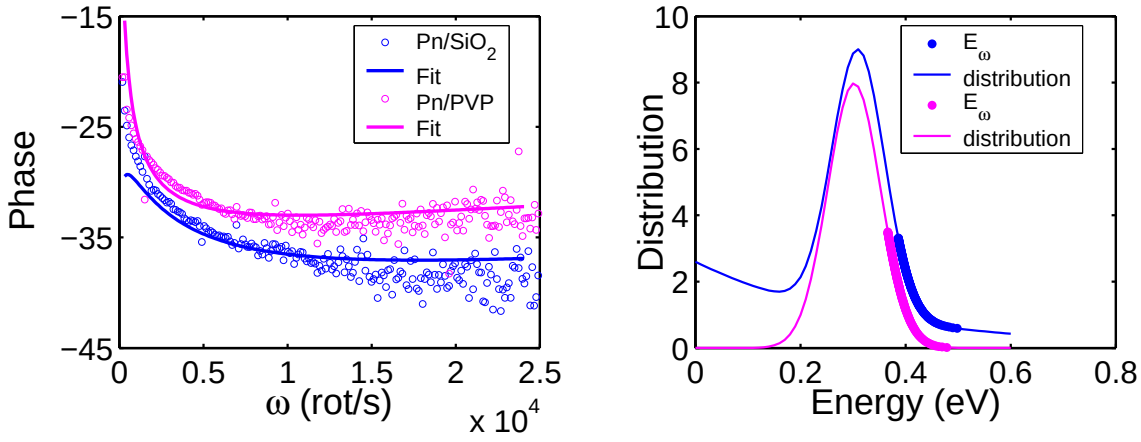

Figure 4.14: The phase of the photocurrent as a function of the modulation frequency for Pn films deposited simultaneously on SiO_2 and PVP (opened circles). Applied voltages: V_{ds} = -6.5 V for both samples, V_g = -69 V for Pn/SiO_2 and -20 V for Pn/PVP. The best fit of the data (full lines) reveal defect states described by gaussian distributions centered at 0.310 eV above HOMO for SiO_2 substrate and 0.302 for PVP. The data for SiO_2 substrate is better represented (for low modulation frequency) if an exponential distribution is added M' $\sim \exp(-\beta E)$. The best fit of the data is obtained for $\beta = 3.0$ eV^{-1}.

tion connecting the two near-neighbor molecules involved in the transition. Based on the assumption of a primary contribution from CT transitions, the differences that we observe in the photocurrent spectra indicate morphological differences in the films. This experimental observation suggests the use of polarized photocurrent spectroscopy as a tool to characterize the performance of a Pn TFT.

Next, we consider the photocurrent magnitude and phase as a function of the modulation frequency. In Fig. 4.14 and 4.15 we have the phase of the photocurrent and the extracted gaussian distributions for the PVP and PMMA sets. The best fits to the data reveal gaussian distributions centered around 0.3 eV above the HOMO for all of these devices. However, we observe slight shifts in the energy from the

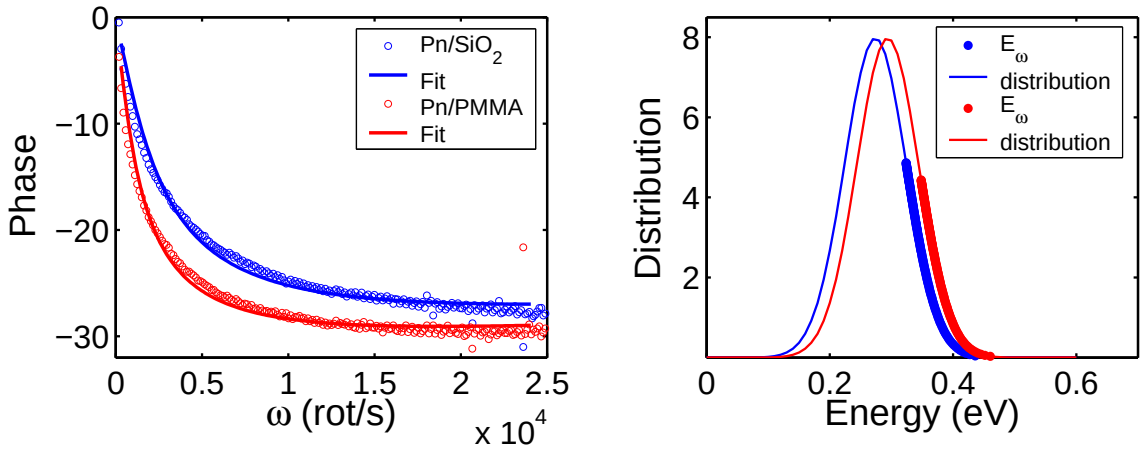

Figure 4.15: The phase of the photocurrent as a function of the modulation frequency for Pn films deposited simultaneously on SiO_2 and PMMA (opened circles). Applied voltages: V_{ds} = -28 V for both samples, V_g = 0 V for Pn/SiO_2 and -64 V for Pn/PMMA. The best fit of the data (full lines) reveal defect states described by gaussian distributions centered at 0.274 eV above HOMO for SiO_2 substrate and 0.294 for PMMA.

$Substrate$	ϵ	$E_0(eV)$	$E_F(eV)$	$N(s^{-1}) \times 10^{10}$	A	$\mu(cm^2/Vs)$	I_{CT}
SiO_2	3.9	0.310	0.585	3.50	0.0165	0.04	0.48
PVP	4.8	0.302	0.496	3.12	0.0948	0.20	0.78
SiO_2	3.9	0.274	0.389	0.66	0.3646	0.10	0.73
$PMMA$	3.4	0.294	0.432	1.70	0.2229	0.03	0.33

Table 4.3: Parameters for pairs of Pn transistors fabricated simultaneously on different dielectric materials. The dielectric constants for PVP and PMMA are reported in Ref. [69].

control sample to the sample with a different dielectric material. Looking at Table 4.3 we see that the shift in the gaussian position seems to correlate with the substrate dielectric constant.

To understand the shift in the gaussian position relative to the dielectric constants we use a simple electrostatic model to describe a negatively charged impurity embedded in Pn in the presence of an interface. The image field generated at the interface can be attractive or repulsive, depending on the dielectric constants of the two materials. The image charge is determined by [71]

$$q' = -\frac{\epsilon - \epsilon_{Pn}}{\epsilon + \epsilon_{Pn}} q,$$

where ϵ_{Pn} is the dielectric constant for Pn and ϵ corresponds to the dielectric material. The electrostatic interaction can be seen as a perturbation in the binding energy associated with the impurity level,

$$E' = \frac{qq'}{8\pi\epsilon_0\epsilon_{Pn}z},$$

where z represents the separation between the impurity and the dielectric material. Assuming the impurity in the first layer of Pn (z=7 Å), the perturbation in the binding energy, E', becomes 0.0447, 0.0790 and 0.0214 eV for SiO_2, PVP and PMMA dielectric. The dielectric constants used in this estimation are presented in Table 4.3. For Pn we used a dielectric constant of $\epsilon_{Pn} = 3$ [72]. This simple estimation shows that a shift of - 0.0344 eV in the gaussian position for Pn on PVP in respect with SiO_2 and of + 0.0233 eV for Pn on PMMA in respect with SiO_2 are expected. This simple electrostatic description is in agreement with the results from our modeling of the photocurrent data.

Analyzing data from the control devices, we cannot ignore the shifts in the gaussian position for Pn on SiO_2 fabricated with different deposition conditions. This experimental observation can be explained using the same electrostatic model described above. In this case, we attribute the differences in the gaussian positions to variations in dielectric constants associated with Pn films. According to Ref. [73] the dielectric constant for Pn is highly anisotropic: ϵ^a_{Pn}= 5.336, ϵ^b_{Pn}= 3.211, ϵ^c_{Pn}= 2.413. Using our data and the simple electrostatic model we can extract an average ϵ_{Pn} for each of the films, assuming the dielectric constant for a particular sample. For instance, in Table 4.4 we chose ϵ_{Pn}=3 [72] for the first Pn film on SiO_2 and the remaining values can be determined from the shifts in the gaussian position. The variation in the dielectric constant suggests, once again, that there are morphological differences in Pn films deposited on different dielectric materials and different deposition conditions, in agreement with the photocurrent spectra presented in Fig. 4.13.

$Substrate$	ϵ_{Pn}
SiO_2	3
PVP	3.38
SiO_2	3.66
$PMMA$	3.68

Table 4.4: Relative dielectric constants for Pn thin films extracted from shifts in the gaussian position.

In summary, we found that transport properties are strongly affected by the dielectric material and the deposition conditions. Inspection of the photocurrent spectra shows that there are structural differences in the Pn films deposited on different dielectric materials. However, these effects cannot explain the presence of the 0.3 eV defect. The morphology differences can account only for small deviations in the position of the localized states.

4.5 Conclusions

In this chapter we have introduced photocurrent modulated spectroscopy as a probe of defect states in Pn TFTs. Photocurrent magnitude and phase as a function of the modulation frequency were measured in Pn TFTs on different dielectric materials. An expression for the photocurrent was deduced to model the photocarrier generation process as a multi-step excitonic process. Applying the model to our experimental data revealed the presence of localized states in the Pn bandgap,

represented by a gaussian distribution, located about 0.3 eV above HOMO. This experimental finding agrees quite well with other published results using different techniques [65, 66, 67].

The influence of the dielectric material on these localized states was addressed via measurements on Pn transistors fabricated on SiO_2, PVP and PMMA. Current-voltage characteristics and photocurrent spectra suggest differences in the Pn thin film structure correlated with different dielectric materials. The origin of the ubiquitous 0.3 eV defect in Pn seems to be unrelated to the morphological differences in Pn films. However, shifts in its position with variable deposition conditions are convincingly correlated with changes in Pn morphology via the orientation dependence of the Pn dielectric constant. Furthermore, small variation in the gaussian position of the defect peak for Pn on different dielectric materials is consistent with the expected image charge effect for Pn through the dielectric substrate.

Chapter 5

Pentacene Thin Film Transistors: Applications

5.1 Overview

Organic electronic materials are currently being investigated as inexpensive alternatives to existing chemical sensing technology and niche electronic applications. In this chapter we demonstrate the capability of Pn-TFT in practical applications such as a humidity sensor and a voltage inverter. However, the bias stress effect is a critical issue that must be addressed for practical operation of Pn TFTs. Bias stress is characterized by the temporal decrease in the source-drain current at an applied constant source-drain voltage which can be exacerbated by the application of high gate biases. We describe here a simple method to overcome the bias stress effect in these devices and quantitatively assess the performance of Pn-TFT as a humidity sensor. Finally, we discuss the design considerations that led to the fabrication of a Pn-TFT inverter on plastic substrate to be used to drive a commercial liquid crystal display.

5.2 Assessing Pn TFT for Chemical Sensing Applications

As a chemical sensor, the active layer of the TFT acts as the sensing membrane. In our case, the signal transduction is achieved by the interaction between pentacene and a chemical agent that leads to a modification of the film conductivity. Thus, the chemical sensing can be accomplished by monitoring the drain-source current. However, such conductivity measurements are complicated by the bias stress effect. As mentioned above, this common but undesired property of TFT manifests itself as a slow decrease in the drain current when the device is turned on for long period of time [74, 75, 76, 77, 78].

5.2.1 Bias-Stress Effect

In Fig. 5.1 we show an example of the drain current of a typical pentacene TFT as a function of time when operating in the linear regime (V_{ds} = -5 V, V_g = -20 V). The curve illustrates how the current decreases continuously with time in a manner that is consistent with bias stress effect seen in organic TFT. Although not shown, the current continues to decrease for at least hundreds of seconds. These data can be fitted with a two-component exponential decay curve given by

$$I(t) = I_0 + A_1 \exp(-t/\tau_1) + A_2 \exp(-t/\tau_2),$$

suggesting the existence of two types of traps in the Pn film. This can be seen from the expression for the time constant which is given by [79]:

$$1/\tau = N_v v \sigma \exp(-\frac{E}{kT}),$$

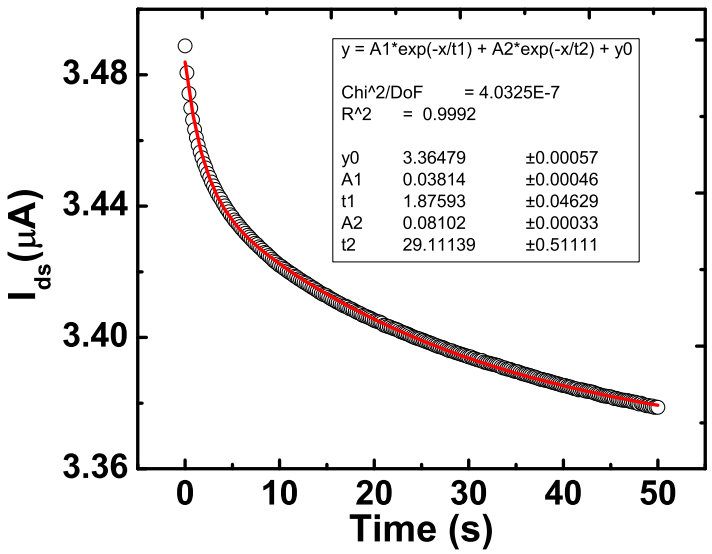

Figure 5.1: The decrease in drain current when the device is operated in the linear regime. The data is very well described by a two-component exponential decay suggesting the presence of two types of traps in the Pn film.

where N_v is the valence band density of states, E is the energetic position of the trap, v is the thermal velocity and σ is the capture cross-section for holes. The time constants for the trapped carriers are $\tau_1 = 1.87$ s and $\tau_2 = 29.11$ s.

5.2.1.1 Overcoming Device Instability Due to the Bias-Stress Effect

Thus, it is imperative that the bias stress effect be controlled. Here we present a simple method for stabilizing the drain current in a Pn TFT so that the sensing capability can be quantitatively assessed.

To overcome the bias stress effect in our devices, we apply voltages of alternating polarity to the gate electrode while the device is operating in linear mode. We find that continually switching the gate voltage polarity from negative (ON state) to positive (OFF state) quickly stabilizes the drain current after a slight initial increase. In Fig. 5.2 we see that stability of the drain-source current as a function of time for a constant drain-source voltage can be achieved by tuning the applied ON/OFF voltages and the time intervals for biasing the gate. The blue curve illustrates the bias stress effect for a time interval of 1000 s, with constant applied voltages of V_{ds} = -5 V and V_g = -15 V. The green and the red curves show the measured current for the same V_{ds} but the gate voltage is switch ON, V_g = -15 V, for 200 ms while the current is recorded in the middle of this time interval. For the next 400 ms the gate voltage is turned OFF, with V_g = 0 V for the green curve and +15 V for the red curve. Once the cycle is repeated the recorded current becomes more stable in time. For practical applications, we thus have found a simple method for stabilizing the

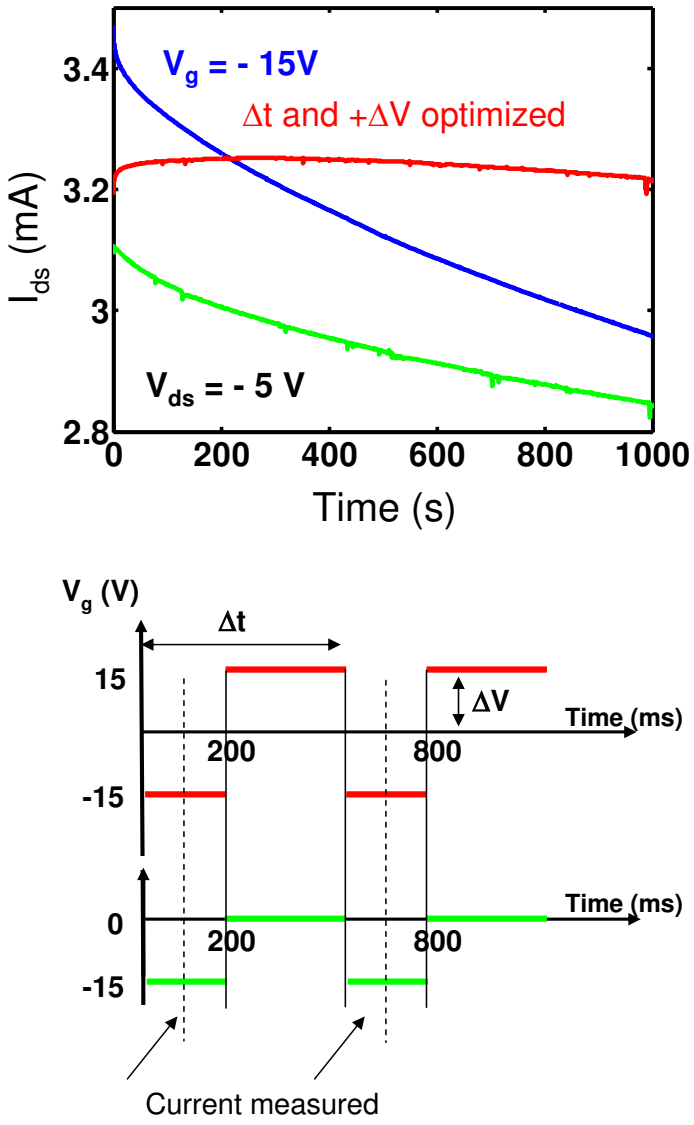

Figure 5.2: Overcoming the bias-stress effects: alternating polarity to the gate electrode. The optimization is achieved tuning the parameters described in the bottom diagram: Vg ON and OFF and the corresponding time intervals.

drain current which allows for evaluation of the sensing capabilities of a pentacene TFT.

Although carrier trapping kinetics is complex in general, we find that two-component exponential works well in describing the bias stress effect in our Pn TFTs. However, alternating the polarity of the gate voltage stabilizes the drain current. It is possible that flipping the gate polarity minimizes the rate of trapping so that the carrier concentration is stabilized. We are not aware of other reports on pentacene TFTs that successfully overcomes bias stress by alternating the gate voltage polarity. Pulsing the gate voltage has been tested for polymer TFTs but was shown not to overcome the bias stress [80]. Others have tried to deal with bias stress by modifying the device geometry or semiconductor dielectric interface or limiting the amount of drain current [80, 81, 82, 83]. The practical result is that once the drain current is stabilized, the device can be tested in a controlled manner.

5.2.2 The Response of the Pn TFT to Water Vapor

Next, we investigate the electrical response of Pn TFTs to water vapor while concurrently controlling the bias stress. We will also analyze the chemical interaction between pentacene and water vapor with Raman spectroscopy.

5.2.2.1 Electrical Investigation

The device under test is placed in the stainless steel vessel designed to allow for controlled introduction of test gases. When testing the effect of water vapor,

dry-nitrogen gas is bubbled into a water bath before being introduced into the test vessel. The saturated water vapor pressure at T = 20 ^{o}C is 17.5 mmHg. In all cases described here the flow rates are 0.5 l/min.

With the device stabilized by alternating the gate voltage polarity, the effect of water vapor on the active layer can be investigated. The drain current is first stabilized at approximately 3.8 μA as the gate voltage is switched ON for 0.3 s then switched OFF for 0.3 s. For this particular ON-OFF cycle, the ON voltage is -20 V and the OFF voltage is +10 V while the source-drain voltage is kept constant at -5 V. We note that the drain current is measured 0.1 s after the device is turned ON.

Fig. 5.3 shows the effect of water vapor on the drain current. In the first 80 s the device is exposed only to dry nitrogen. The gas flow is then switched from dry nitrogen to nitrogen saturated with water vapor for about 15 s. As a result the drain ON current is reduced to approximately 3.6 μA. As can be seen in Fig. 5.3 the decrease in drain current appears to be linear for 4-5 s before decaying exponentially. The drain current can be fitted with a first order decay equation, with a time constant of τ = 1.7 s. After the 15 s exposure to water-saturated (wet) nitrogen, the gas flow is switched back to dry nitrogen. The drain current fluctuates around 3.6 μA before increasing. During this "drying" phase, the drain current can be fitted with first order growth equation and the current is completely recovered in 800 s.

To further characterize the effect of water vapor on Pn TFT, sets of I-V characteristics were measured when the device is exposed to dry nitrogen flow, then wet nitrogen flow, and then dry nitrogen flow again. The I-V characteristics are mea-

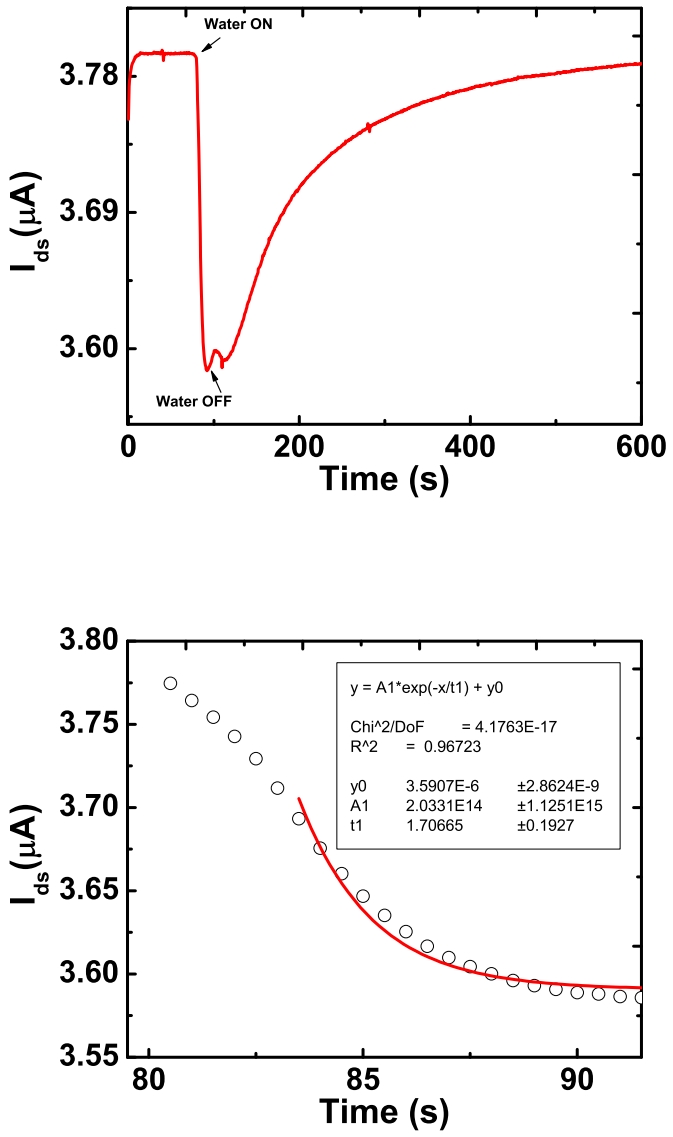

Figure 5.3: The effect of water vapor on the pentacene TFT drain current when the polarity of the gate voltage is alternating. The bottom graph presents the detailed behavior of the drain current while the water exposure is ON.

sured every 10 or 15 minutes to minimize the bias stress. The extracted linear and saturation mobilities are shown in Fig. 5.4. In the first 75 minutes when the device is exposed only to dry nitrogen flow, the linear mobility is found to be approximately 0.08 cm^2/Vs while the saturation mobility is about 0.05 cm^2/Vs. Then wet nitrogen flow is introduced for 15 minutes, and both saturation and linear mobilities decrease in the same manner to roughly half of their initial values. After 15 minutes of exposure to water vapor, the device is then dried in nitrogen flow. Notice that the mobilities nearly recover to their initial values during 15 minutes of exposure to dry nitrogen flow. The threshold voltage is also extracted from the acquired I-V characteristics. As seen with the mobilities, the threshold voltage of -3.2 V is nearly constant during the 75 minutes of exposure to dry nitrogen flow (Fig. 5.4). When the wet nitrogen flow is initiated, the threshold voltage shifts to approximately -1.0 V. When the dry nitrogen flow is re-introduced, the threshold voltage shifts back to the initial value of -3.2 V.

The drain current decreases when the device is exposed to water vapor. The initial decrease is linear, followed by subsequently decay in an exponential fashion. The linear part can be also looked upon as an exponential decay, characterized by a higher time constant. Thus, the water vapor seems to create hole traps in the active layer such that deep traps are filled first, giving rise to the apparent linear decrease, and then the shallow traps follow. We find it quite interesting that even though pentacene is hydrophobic, the conduction mechanism is affected by the presence of water vapor, and thus suggesting that pentacene might be permeable to water vapor. It is well known that hydrophobic organic polymers (e.g. PET) are permeable to

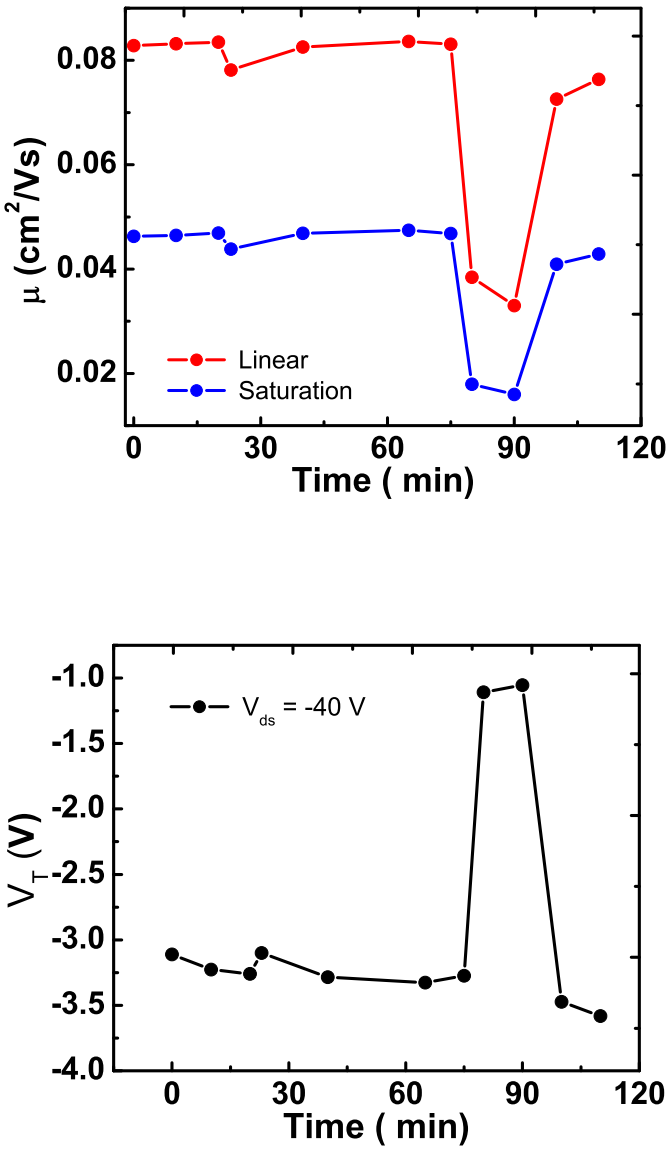

Figure 5.4: The effect of water vapor on pentacene TFT linear saturation mobility and threshold voltage. Each recovers after the wet nitrogen flow is switched to dry nitrogen flow.

water vapor [86, 87, 88]. Thus, it may be that the uptake of water by pentacene is also accomplished by the vapor diffusing through the film in the voids near the grain boundaries. The presence of water at the grain boundaries could effectively reduce the conductivity of the pentacene film and hence lower the mobility. In addition, the eventual presence of water at the pentacene/dielectric interface could effect the observed shift in the threshold voltage. It is well known that chemically modified silicon oxide, with self assembled monolayers having a permanent dipole moment, determine changes in the threshold voltage [80, 89, 90]. Even though little is known about pentacene permeability to water vapor, the presence of water at the edge of the grain boundaries nicely explains the reversibility of the effects of water.

5.2.2.2 Raman Investigation

We used vibrational Raman scattering spectroscopy as a probe to investigate possible chemical interaction between Pn and water vapor. The experiments were carried out under a controlled exposure to water vapor. Raman spectra for Pn were accumulated in ultra-high vacuum of 4×10^{-9} Torr. The vacuum chamber was subsequently saturated with water vapor (with a final pressure of 5×10^{-5} Torr) and the spectra were measured over a duration of 48 hours.

A typical Raman spectrum, collected from a 50 nm Pn film deposited on SiO_2, is presented in Fig. 5.5. We find the Pn vibrational peaks are in good agreement with reports in the literature [84]. The modes in the wavelength range of 180-550 cm^{-1} are characteristic of C-C-C out-of-plane bending modes, those at 751 and 996

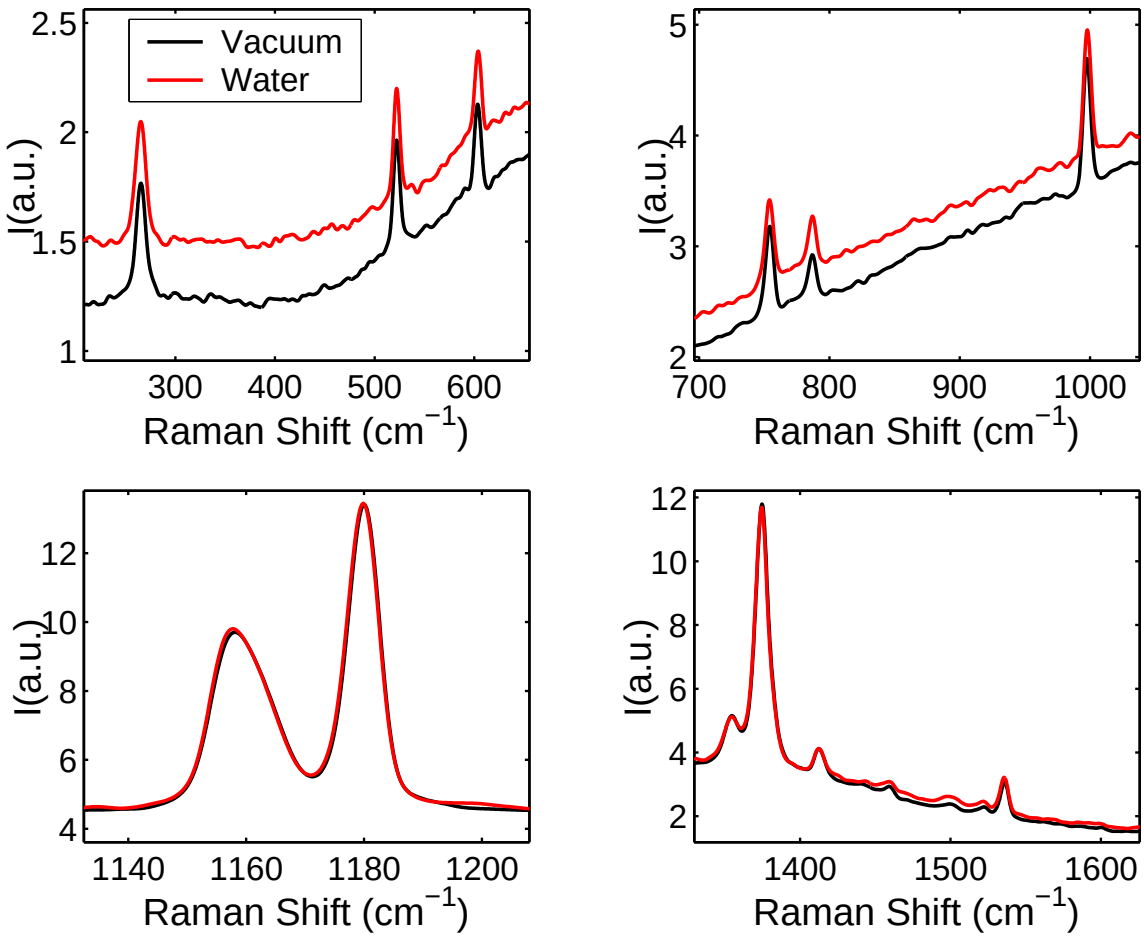

Figure 5.5: In-situ Raman spectra for a Pn thin film before and after water vapor exposure. The similarity in the Raman peaks in both cases indicates the absence of chemical interaction between Pn and water vapor.

cm^{-1} correspond to C-H out-of-plane bending modes, while the ones in the 1100-1200 cm^{-1} are characteristic of C-H in plane bending (or rocking) modes. The dominant vibrations found around 1300-1700 cm^{-1} represent the highly polarizable aromatic C-C stretching modes. The high frequency C-H aromatic stretching modes (3000-3100 cm^{-1}) are very weak and not distinguishable in our spectra.

The chemical interaction of Pn with water is expected to be reflected in Raman spectra as shifts in the position and/or modulation of the intensity of pertinent vibrational modes. The most reactive carbon atoms in the Pn molecule are situated in the middle aromatic ring [85]. Thus, one possible scenario is the hydrolytic interaction between the water vapor and Pn to form C-H_2 and C-H-OH chemical bonds. The expected Raman active modes for these bonds are in the 2870-2950 cm^{-1} range with a medium-strong intensity and 1310-1400 cm^{-1}, corresponding to medium-weak intensity, respectively. However, our in-situ Raman measurements for Pn before and after water vapor exposure did not detect the presence of any of these vibrational modes characterizing the reaction of the Pn molecule. Furthermore, as shown in Fig. 1.3, the observed modes in Pn are unchanged before and after the exposure. Our Raman experiment suggests negligible chemical interaction between Pn and water vapor at 10^{-5} Torr, at room temperature.

Since it is unlikely that chemistry is occurring between the film and the water in the voids, the vapor can diffuse in or out of the film. Thus, the effect of water on the device characteristics will be reversible. We also cannot rule out the possibility of water vapor affecting the gold/pentacene interface.

5.3 Simple Inverter with Pn TFTs

Next, we assess the viability of the Pn TFT as a electronic device. A simple voltage inverter consisting of two Pn TFTs was fabricated. As a demonstration, the inverter was successfully used to control the output of a liquid crystal display.

Two Pn transistors with different geometries are connected using diode-load logic [91, 92], as presented in Fig. 5.6. The input voltage is the gate voltage on the drive transistor and the output voltage is measured between the two transistors. When the input voltage is zero or positive the load transistor is heavily ON and the drive transistor is OFF, and as a result the output will be pulled down against the drive. Ideally, V_{out} approaches - V_{dd}. When the input is low the voltage drop across the drive is very small and V_{out} approaches V_s. To successfully transfer the output voltage of the inverter to a real device, we have to match the impedances: the output impedance of the drive should be lower ($< 1/10$) than the input impedance of the device that we want to control. However, the input impedance for the liquid crystal display is of order kΩ while the impedance for our standard devices is MΩ.

To minimize the impedance mismatch between the two devices, we fabricated interdigitated electrodes on the drive transistor such that the W/L was increased from 30 (our standard devices) to 4000 (or 8000 depending on configuration) for the new design while keeping the overall dimensions of the device 3 by 3 mm^2. These new devices were fabricated on a flexible transparent substrate (PET) using the transfer printing technique [93]. As expected, the current-voltage curves (Fig. 5.7) for these fingered electrode transistors are characterized by an increase of 3 orders

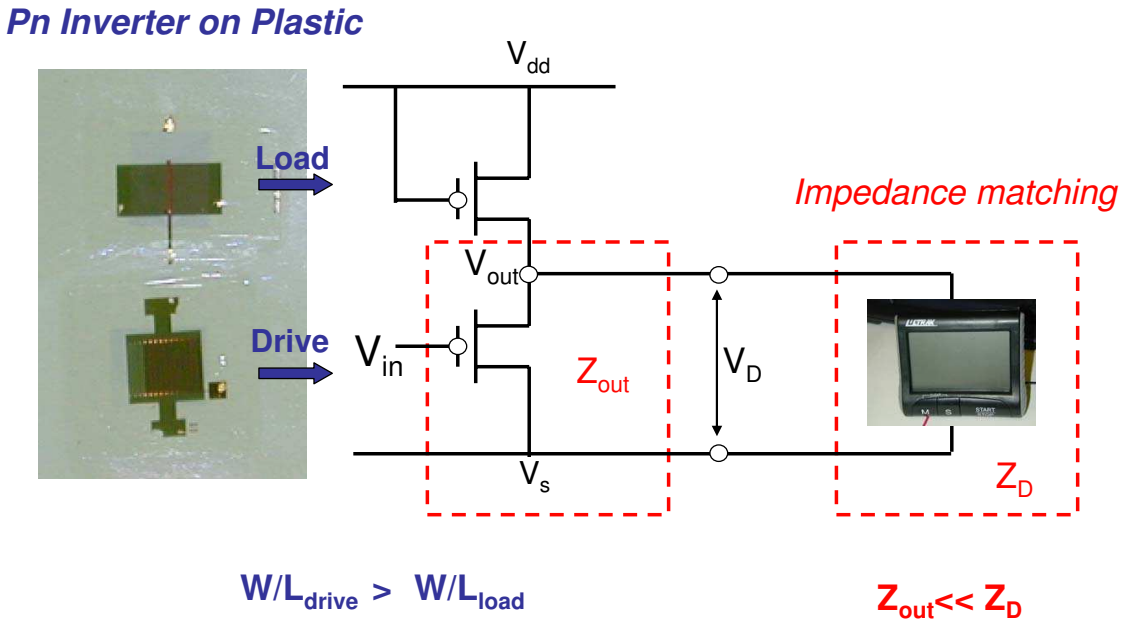

Figure 5.6: Diode-connected inverter with Pn TFTs. The devices are fabricated on plastic substrates using the imprinting technique [93]. The W/Ls are 30 for load and 4014 for drive. The circuit was used to control a liquid crystal display to prove the applicability of Pn TFTs.

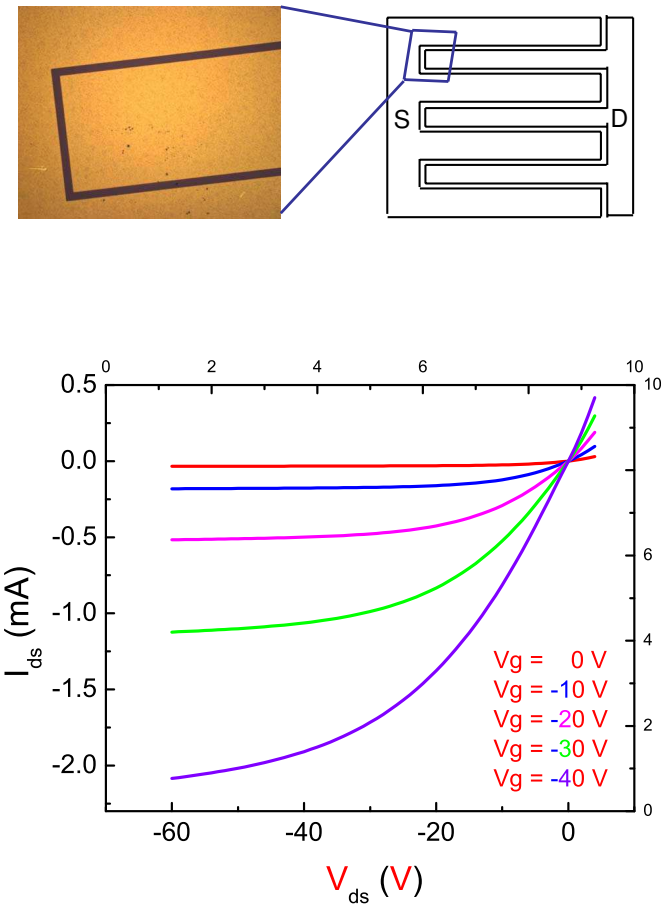

Figure 5.7: Interdigitate electrodes allow a substantial increase of the W/L ratio decreasing the device impedance. The current-voltage characteristics are measured in a bottom electrode Pn transistor with W = 88.91 mm, L = 200 μm, and 50 nm Pn thin film as active material.

of magnitude in the I_{ds} for the usually applied voltages. Since the impedance of the inverter is primarily determined by the drive transistor, we have also decreased the output impedance of the inverter by three orders of magnitude.

In Fig. 5.8 we present the measured input-output characteristic of our Pn inverter fabricated on PET, for applied voltages of V_{dd} = - 45 V and V_s = + 10 V. Notice that for input voltages larger than 20 V, the output has a constant value of approximately -20 V. For negative input voltages, V_{out} asymptotically approaches V_s. One feature of this inverter is the position of the trip point, corresponding to equal magnitudes for input and output voltages. The trip point is approximately 10 V for this particular choice of applied voltages. The trip point also coincides with the point of maximum gain, which we found to be 1.75 (g = $\frac{\Delta V_{out}}{\Delta V_{in}}$).

The inverter was also characterized by its response time to an alternating input voltage. This was accomplished by measuring the voltage across a load resistor every 100 ms. We show in Fig. 5.8 the voltage transferred across a 40 kΩ resistor while the input voltage is switched from 0 to -20 V. The resulting rise time is found to be approximately 200 ms.

In Fig. 5.6, we show our inverter circuit modulating the output of a commercial liquid crystal display (LCD). In this case, the output impedance of the inverter was reduced to roughly 80 kΩ which was low enough to permit a useful voltage across the LCD. As a result, we were able to successfully turn the LCD on and off even though the impedances of the devices were not quite matched.

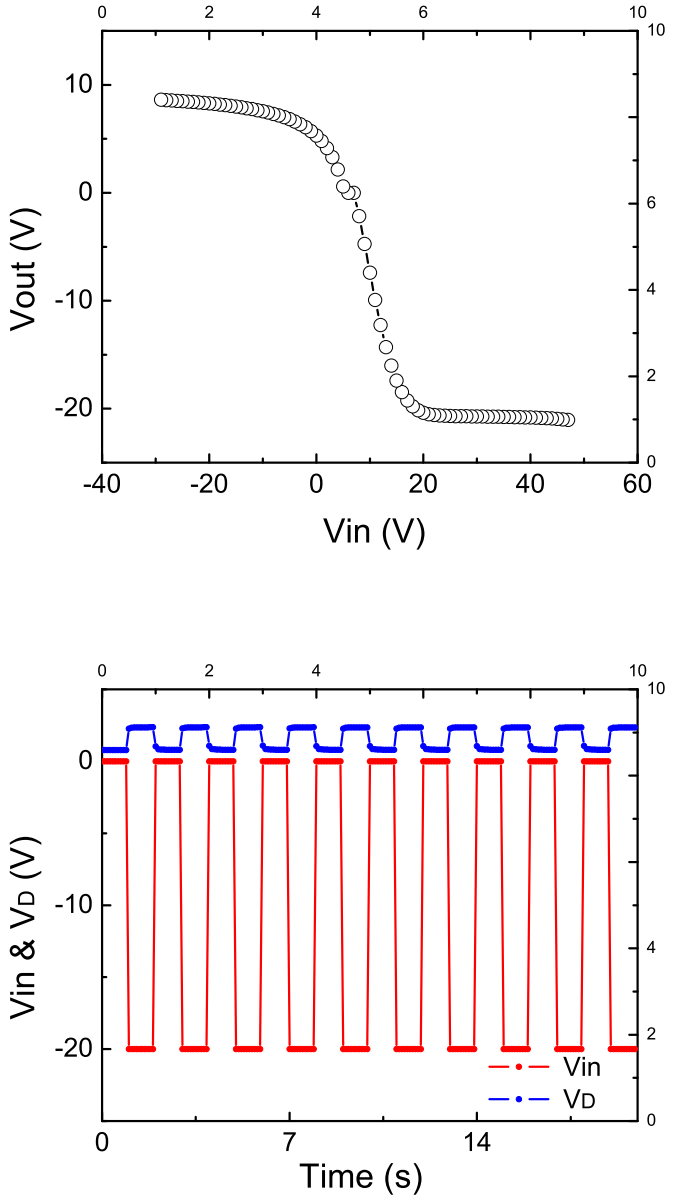

Figure 5.8: The measured input-output characteristic of the plastic inverter presented in Fig. 5.6. In the bottom graph we present the input voltage and the output voltage transferred across a 40 kΩ resistor as a function of time. The inverter switching speed is 200 ms.

5.4 Conclusions

We explored the possible application of Pn TFTs as humidity sensor. An important issue that was addressed is the bias-stress effect. The shape of the temporal decrease in the source-drain current associated with this effect is consistent with carrier trapping by shallow and deep level defects. We described a novel technique to overcome this effect which is crucial for practical applications of these devices as sensors.

We investigated quantitatively the effects of water-vapor exposure on the electrical characteristics of Pn TFTs. We observed a 10 percent decrease in source-drain current upon exposure of the transistor to approximately 1 μmole of water. Our Raman spectroscopy results suggested that this change is not due to chemical interaction between Pn and water vapor. A more likely scenario is the permeability of Pn to water leading to modification of tunneling barriers at grain boundaries.

In the last section, we demonstrated a simple inverter circuit using Pn TFTs fabricated on PET substrates. The drive transistor was modified to minimize the output impedance typical of Pn TFT. The fabrication process needs to be optimized to improve and control the gain of the inverter. However, we find that even a device with marginal transistor characteristics is still able to drive a commercial LCD device.

Chapter 6

Conclusions

We have presented a novel investigation of Pn TFTs using photocurrent modulation spectroscopy. This technique allowed us to address important issues concerning charge transport in organic transistors. For example, we demonstrated that the field effect mobility and the density of free charge carriers of these devices can be extracted without relying on assumed models of transport. This was carried out by empirically analyzing the direct- and photocurrent-voltage characteristics. We were able to find that the field effect mobility increases with the applied gate voltage as $\mu_0 \sim V_g^{1/3}$. We were also able to separate the total charge in the conduction channel into free and trapped charge carriers. More specifically, our results showed that approximately half the total charge density is trapped when the gate voltage is zero.

Further, we used photocurrent modulation spectroscopy as a probe of the defect states in thin films of pentacene. This was done by measuring the magnitude and phase of the photocurrent while tuning the incident radiation to the singlet exciton transition. The data were modeled by assuming that the photocarriers are generated in a multi-step process that includes exciton dissociation and interaction with trapped holes. We find that the data are well described by a gaussian distri-

bution located about 0.3 eV above the HOMO. This result is in good agreement with photoluminescence results reported by He *et al.* [67], which is complementary to our technique. In addition, there are two other independent methods that also agree with our results [65, 66]. We also investigated the effect of the gate dielectric material with our probe and found that the position of the extracted gaussian slightly shifts, consistent with the expected image charge effect for Pn through the dielectric substrate. Also shifts in the gaussian position for samples fabricated with variable deposition conditions are correlated with changes in Pn morphology. The morphological differences between Pn films were also detected in current-voltage characteristics and photocurrent spectra. However, the origin of the ubiquitous 0.3 eV defect in Pn seems to be unrelated to structural differences in Pn films.

Finally, we explored the viability of Pn TFTs in practical circuits. To do this, first we found a simple method to overcome the bias-stress effect, a major obstacle for the implementation of organic electronic devices. By alternating the polarity of the gate voltage, the drain current can be stabilized. This allowed us to quantitatively study the effect of water vapor on the electrical characteristics of Pn TFTs. We found a 10 percent decrease in the drain current upon exposure to approximately 1 μmole of water, with nearly 100 percent recovery after drying the device with flowing nitrogen. These results suggest that Pn TFTs might be useful as gas phase sensor. We also demonstrated the Pn TFTs can be used to construct a simple voltage inverter on a clear flexible substrate. To make Pn TFTs practical, however, we have found that the output impedance of these devices needs to be reduced so that commercially available components can be integrated with them.

BIBLIOGRAPHY

[1] A. Tsumura, H. Koezuka, and T. Ando, Appl. Phy. Lett. **49**, 1210 (1986).

[2] G. Horowitz, D. Fichou, X. Peng, Z. Xu, and F. Garnier, Solid State Commun. **72**, 381 (1989).

[3] G. Horowitz, X. Peng, D. Fichou, and F. Garnier, Synth. Met. **51**, 419, (1992).

[4] C. D. Dimitrakopoulos, A. R. Brown, and A. Pomp, J. Appl. Phys. **80**, 2501 (1996).

[5] Y.-Y. Lin, D. J. Gundlach, and T. N. Jackson, 54th Annual Device Research Conference Digest, 80 (1996).

[6] Y.-Y. Lin, D. J. Gundlach, S. Nelson, and T. N. Jackson, IEEE Electron Dev. Lett. **44**, 1325 (1997).

[7] Y.-Y. Lin, D. J. Gundlach, S. F. Nelson, and T. N. Jackson, IEEE Electron Dev. Lett. **18**, 606 (1997).

[8] N. C. Greenham, C. D. Dimitrakopoulos, and C. D. Frisbie, Mater. Res. Soc. Symp. Proc. **771**, 169, (2003).

[9] E. A. Silinsh and V. Cepek, *Organic Molecular Crystals* (AIP, New York, 1994).

[10] R. B. Campbell, J. Trotter, and J. M. Robertson, Acta Cryst. **14**, 705 (1961).

[11] J. M. Robertson, D. G. Watson, G. A. Sim, and H. M. M. Shearer, Acta Cryst. **15**, 697 (1961).

[12] V. M. Abrahams, J. M. Robertson, and J. G. White, Acta Cryst. **2**, 233 (1949).

[13] A. Mathieson, J. M. Robertson, and V. C. Sinclair, Acta Cryst. **3**, 245 (1950).

[14] J. Trotter, Acta Cryst. **15**, 289 (1962).

[15] C. D. Dimitrakopoulos and P. R. L. Malenfant, Adv. Mat. **14**, 99 (2002).

[16] C. C. Mattheus, A. B. Dros, J. Baas, G. T. Ostergetel, A. Meetsma, J. L. de Boer, and T. T. M. Palstra, Synth. Met. **138**, 475 (2003).

[17] T. Minakata, I. Nagoya, and M. Ozaki, J. Appl. Phys. **69**, 7354 (1991).

[18] J. G. Laquindanum, H. E. Katz, A. J. Lovinger, and A. Dodabalapur, Chem. Mater. **8**, 2542 (1996).

[19] M. Pope and C. E. Swenberg, *Electronic Processes in Organic Crystals and Polymers* (Oxford University Press, New York, 1999).

[20] A. S. Davydov, *Theory of Molecular Excitons* (Mc-Graw Hill, New York, 1962).

[21] D. V. Lang, X. Chi, T. Siegrist, A. M. Sergent, and A. P. Ramirez, Phys. Rev. Lett. **93**, 086802 (2004).

[22] C. Jundt, G. Klein, B. Sipp, J. Le Moigne, M. Joucla, and A. A. Villaeys, Chem. Phys. Lett. **241**, 84 (1995).

[23] L. Sebastian, G. Weiser, H. Bassler, Chem. Phys. **61**, 125 (1981).

[24] R. M. Glaeser and R. S. Berry, J. Chem. Phys. **44**, 3797 (1966).

[25] E. A. Silinsh *Organic Molecular Crystals. Their Electronic States* (Springer-Verlag, Berlin, Heidelberg, 1981).

[26] E. A. Silinsh, G. A. Shlihta, and A. J. Jurgis, Chem. Phys. **138**, 347 (1989).

[27] T. Holstein, Ann. Phys., **8**, 343 (1959).

[28] V. Y. Butko, X. Chi, D. V. Lang, and A. P. Ramirez, Appl. Phy. Lett. **83**, 4773 (2003).

[29] O. D. Jurchescu, J. Baas, and T. T. M. Palstra, Appl. Phy. Lett. **84**, 3061 (2004).

[30] N. Karl, J. Marktanner, R. Stehle, and W. Warta, Synth. Met. **42**, 2473 (1991).

[31] N. Karl, J. Cryst. Growth **99**, 1009 (1990).

[32] N. Karl, *11^{th} Molecular Crystal Symposium*, Switzerland, Sept. 30-Oct. 8, 351, (1985).

[33] L. B. Schein, Phys. Rev. B **15**, 1024 (1979).

[34] L. B. Schein and A. R. McGhie, Phys. Rev. B **20**, 1631 (1979).

[35] J. Takeya, C. Goldmann, S. Haas, K. P. Pernstich, and B. Batlogg, J. Appl. Phys. **94**, 5800 (2003).

[36] N. J. Watkins, L. Yan, and Y. Gao, Appl. Phy. Lett. **80**, 4384 (2002).

[37] J. Zaumseil, K. W. Baldwin, and J. A. Rogers , J. Appl. Phys. **93**, 6117 (2003).

[38] H. A. Szymanski, *Raman Spectroscopy. Theory and Practice* (Plenum Press, New York, 1967).

[39] J. R. Ferraro and K. Nakamoto, *Introductory Raman Spectroscopy* (Academic Press, San Diego, 1994).

[40] G. Horowitz and P. Delannoy, J. Appl. Phys. **70**, 469 (1991).

[41] L. Torsi, A. Dodabalapur, and H. E. Katz, J. Appl. Phys. **78**, 1088 (1995).

[42] N. F. Mott, *Conduction in Non-crystalline Materials* 2nd Edition (Clarendon Press, Oxford 1993).

[43] M. C. J. M. Vissenberg and M. Matters, Phys. Rev. B **57**, 12964 (1998).

[44] S. M. Sze, *Physics of Semiconductor Devices* (Wiley, New York, 1981).

[45] G. Horowitz, Adv. Mat. **10**, 365 (1998).

[46] C. D. Dimitrakopoulos, S. Purushothaman, J. Kymissis, and A. Callegari, J. M. Shaw, Science **283**, 822 (1999).

[47] P. G. Le Comber and W. E. Spear, Phys. Rev. Lett. **25**, 509 (1970).

[48] K. Ryu, I. Kymissis, V. Bulovic, and C. G. Sodini, IEEE Electron Dev. Lett. **26**, 716 (2005).

[49] E. A. Silinsh, A. I. Belkind, D. R. Balode, A. J. Biseniece, V. V. Grechov, L. F. Taure, M. V. Kurik, J. I. Vertzmacha and I. Bok, Phys. Status Solidi (a) **25**, 339 (1974).

[50] A. R. Brown, C. P. Jarrett, D. M. de Leeuw, and M. Matters, Synth. Met. **88**, 37 (1997).

[51] G. Horowitz, R. Jahlaoui, and P. Delannoy, J. Phys. III **5**, 355 (1995).

[52] W. A. Schoonveld, J. Wildeman, D. Fichou, P. A. Bobbert, B. J. van Wees, T. M. Klapwijk, Nature **404**, 977 (2000).

[53] D. E. Aspnes and J. E. Rowe, PRB **5**, 4022 (1972).

[54] O. Ostroverkhova, D. G. Cooke, S. Shcherbyna, R. F. Egerton, F. A. Hegmann, R. R. Tykwinski, and J. E. Anthony, Phys. Rev. B **71**, 035204 (2005).

[55] C. D. Dimitrakopoulos and D. J. Mascaro, IBM J. Res. Dev. **45**, 11 (2001).

[56] B.I. Shklovskii and A.L. Efros, *Electronic properties of doped semiconductors* (Springer-Verlag, Berlin 1984).

[57] J M Marshall, Rep. Prog. Phys. **46**, 1235 (1983).

[58] A. R. Volkel, R. A. Street, and D. Knipp, Pys. Rev. B **66**, 195336 (2002).

[59] H. Oheda, J. Appl. Phys. **52**, 6693 (1981).

[60] P. Kounavis, Phys. Rev. B **64** 0452041 (2001).

[61] G. Schumm and G. H. Bauer, Phys. Rev. B **39** 5311 (1989).

[62] K. C. Kao and W. Hwang, *Electrical Transport in Solids with Particular Reference to Organic Semiconductors* (AIP, New York, 1994).

[63] J. Levinson, S. Z. Weisz, A. Cobas, and A. Rolon, J. Chem. Phys. **52**, 2794 (1970).

[64] E. L. Frankevich and E. I. Balabanov, Soviet Phys. Solid State **8**, 1567 (1966).

[65] I. Muzicante and E. A. Silinsh, Acta Phys. Polonica A **88**, 389 (1995).

[66] Y. S. Yang, S. H. Kim, J.-I. Lee, H. Y. Chu, L.-M. Do, H. Lee, J. Oh, T. Zyung, M. K. Ryu, and M. S. Jang, Appl.Phys. Lett. **80**, 1595 (2002).

[67] R. He, X. Chi, A. Pinczuk, D. V. Lang and P. Ramirez, Appl. Phy. Lett. **87**, 211117 (2005).

[68] A. Kazanskii and K. Y. Khabarova, Semiconductors **38**, 1261 (2004).

[69] A. Issac and C. von Borczyskowski, Phy. Rev. B **71**, 161302 (2005).

[70] V. M. Agranovivh and G. C. La Rocca, *Organic Nanostrctures: Science and Applications* (IOS, Ohmsha 2002).

[71] J. D. Jackson, *Classical Electrodynamics* 3rd Edition (Wiley, New York 1999).

[72] M. Matters, D. M. de Leeuw, M. J. C. M. Vissenberg, C. M. Hart, P. T. Herwig, T. Geuns, C. M. J. Mutsaers, and C. J. Drury, Opt. Mat. **12**,189 (1999).

[73] E. V. Tsiper and Z. G Soos, Phys. Rev. B **68**, 085310 (2003).

[74] D. Knipp, R. A. Street, A. Volkel, and J. Ho, J. Appl. Phys. **93**, 347 (2003).

[75] R. A. Street, A. Salleo and M. L Chabinyc, Phys. Rev. B **68**, 085316 (2003).

[76] G. Horowitz, R. Hajlaoui, D. Fichou, and A. E. Kassmi, J. Appl. Phys. **85**, 3202 (1999).

[77] A. Salleo and R. A. Street, J. Appl. Phys. **94**, 471 (2003).

[78] D. B. A. Rep, A. F. Morpurgo, W. G. Sloof, and T. M. Klapwijk, J. Appl. Phys. **93**, 2082 (2003).

[79] R. H. Bube, *Photoconductivity of Solids* (John Wiley and Sons, New York,1960).

[80] A. Salleo, M. L. Chabinyc, M. S. Yang, and R. A. Street, Appl. Phys. Lett. **81**, 4383 (2002).

[81] H. E. A. Hiutema, G. H. Gelinck, J. B .P . H. van der Putten, K. E. Kuijk, C. M. Hurt, E. Cantatore, P. T. Herwig, A. J .J. M. van Breeman and D. M. de Leeuw, Nature **414**, 599 (2001).

[82] H. E. A. Hiutema, G. H. Gelinck, J. B .P . H. van der Putten, K. E. Kuijk, C. M. Hurt, E. Cantatore, and D. M. de Leeuw, Adv. Mater. **14**, 1201 (2002).

[83] M. Matters, D. M. de Leeuw, M. J. C. M Vissenberg, C. M. Hart, P. T. Herwig, T. Geuns, C. M. J. Mutsaers and C. J. Drury, Opt. Mater. **12**, 189 (1999).

[84] L. Colangeli, V. Mennella, G. A. Baratta, E. Bussoletti and G. Strazzulla, Astrophys. J., **389**, 369 (1992).

[85] J. E. Northrup and M. L. Chabinyc, Phys. Rev. **68**, 041202 (2003).

[86] Y. G. Tropsha and N. G. Harvey, J. Phys. Chem. B **101**, 2259 (1997).

[87] A. S. da Silva Sobrinho, M. Latreche, G. Czeremuszkin, J. E. Klemberg-Sapieha and M. R. Wertheimer, J. Vac. Sci. Technol. A **16**, 3190 (1998).

[88] B. M. Henry, A. G. Erlat, A. McGuigan, C. R. M. Grovenor, G. A. D. Briggs, Y. Tsukahara, T. Mizamoto, N. Noguchi, and T. Nijima, Thin Solid Films **382**, 194 (2001).

[89] K. P. Pernstich, S. Haas, D. Oberhoff, C. Goldmann, D. J. Gundlach, B. Batlogg, A. N. Rashid, and G. Schitter, J. Appl. Phys. **96**, 6431 (2004).

[90] H. E. Katz, X. M. Hong, A. Dodabalapur, and R. Sarpeshkar, J. Appl. Phys. **91**, 1572 (2002).

[91] E. Cantatore and E. J. Meijer, IEEE **7803**, 8108 (2003).

[92] S. H. Jung, W. J. Nam, J. H. Lee, J. H. Jeon, and M. K. Han, IEEE Electron Dev. Lett. **26**, 23 (2005).

[93] D. R. Hines, S. Mezhenny, M. Breban, E. D. Williams, V. W. Ballarotto, G. Esen, A. Southard, and M. S. Fuhrer, Appl. Phys. Lett. **86**, 163101 (2005).